UCLouvain
Institute of Mechanics,
Materials and Civil Engineering

Flow Electrification of Dielectric Liquids: Modeling and Numerical Study

---

Doctoral dissertation presented by

Mathieu CALERO

in partial fulfillment of the requirements for
the degree of Doctor in Engineering Sciences

August 30, 2023

Thesis committee

Pr. Sandra SOARES FRAZAO (*president*)	UCLouvain
Pr. Miltiadis V. PAPALEXANDRIS (*co-supervisor*)	UCLouvain
Dr. Holger GROSSHANS (*co-supervisor*)	PTB, Germany
Pr. Philippe CHATELAIN	UCLouvain
Pr. Ionel Sorin CIUPERCA	UCB, France
Dr. Christos VARSAKELIS	Janssen Pharmaceutical

À mes très chers parents.

Abstract

When a liquid is in contact with a solid surface, physico-chemical phenomena occur at the interface, leading to the formation of the electrical double layer. Inside the liquid, the electrical double layer comprises the Stern layer corresponding to a thin region adjacent to the solid/liquid interface, and the diffuse layer, whose the concentration of free ions decreases away from the Stern layer. Accordingly, flow electrification takes place when a flowing liquid, in contact with a solid, transports electric-charge carriers (ions) from the diffuse layer towards the bulk of the flow domain. This motion, in turn, generates a streaming current that is deemed responsible of major electrostatic accidents in the petrochemical industrial sector. Although studied extensively during the last 50 years, this phenomenon is currently not well understood, notably because of the inherent complexity of flow turbulence. Indeed, conclusive studies about the role of turbulence and the underpinning mechanisms of turbulent flow electrification are still lacking. Therefore, this thesis studies in detail the phenomenon of electrification of flowing dielectrics liquids, notably in turbulent channel flows.

To this end, we present in Chapter 2 the governing equations for the flow of interest, which consists of the incompressible Navier-Stokes equations (supplemented with a volumetric electric force) and the conservation equation for the electric charge density. Additionally, we detail the numerical algorithm employed to solve these equations.

In Chapter 3, we elaborate on the structure of the diffuse layer and its properties. First, we derive a closed-form solution for the electric charge density in a fully developed diffuse layer, when the liquid is at rest. On the basis of this solution, we then

develop a suitable expression for the thickness of the diffuse layer, which is related to the Debye length (which in turn is a material property of the dielectric liquid). Then, we show that the charge-density distribution is not affected by a laminar flow. Accordingly, we derive a closed-form expression for the streaming current in laminar channel flow which is inevitably generated by the motion of the liquid along the solid surface. Subsequently, we perform simulations in the turbulent regime.

In Chapter 4, we report on Direct Numerical Simulations (DNS) of electrification in turbulent channel flow of liquid dielectrics. As expected from earlier observations, electric-charge carriers are transported by the turbulent structures of the flow, from the diffuse layer towards the bulk of the channel. Due to this transport, the streaming current in the liquid increases considerably with the turbulence intensity of the flow. Also, we describe the various stages of turbulent flow electrification. In particular, the electrification rate increases with the turbulence intensity. For the last (stationary) stage, in which the process of electrification has been completed, we analyze the statistical properties of the electric charge density. According to our analysis, the charge-density distribution consists of three zones. In the first one, adjacent to the wall, the dominant mechanism is via ionic diffusion. Whereas in the second one the dominant mechanisms are convective and conductive currents. In the third zone, which corresponds to the bulk of the channel, the electric charge density remains almost constant. Further, we analyze the budget of the charge-density variance. Based on this analysis, molecular transport counter-balances molecular dissipation at the walls, and production counter-balances turbulent transport away from them. On another note, our simulations predict that the ohmic resistance counter-acts the convective currents, while the diffusive term plays a role only in the first zone of the charge-density distribution. Furthermore, we provide a closed-form expression for the mean charge-density profile based on the gradient assumption which agrees well with our DNS results.

In Chapter 5, we derive the filtered governing equations for the problem of interest. Then, we present four possible subgrid-scale eddy-diffusivity models. Subsequently, upon validation, we carry out Large Eddy Simulations (LES) at higher turbulence intensities with the most accurate model, which is based on the gradient assumption and on the introduction of the subgrid-scale electric Schmidt number. Accordingly, our LES predict the same properties and structure of the charge-density distribution as the ones predicted by our DNS at lower Reynolds numbers.

Remerciements

Petit, je voulais être banquier, jusqu'à ce que je réalise que les banquiers ne gardaient pas tout l'argent qu'on leur donnaient. C'était dès lors acté, je voulais devenir vétérinaire parce que cela concilie mon amour pour les animaux, mon intérêt pour la chirurgie et le fait que l'on puisse m'appeler Docteur Calero. Tout était réfléchi. Lors des portes ouvertes, j'ai visité ma future école vétérinaire qui n'attendait que l'obtention de mon baccalauréat. C'était sans compter sur ma mère qui m'a dit : "l'Université ouvre aussi ses portes, tu veux aller voir avant qu'on ne rentre ?".

Allons-y ! Là, j'ai fait la rencontre de Jesse Groenen qui, avec son immense charisme, a réussi à me vendre les qualités de la formation "parcours spéciaux" et à me transmettre sa passion pour la recherche. J'étais alors conquis. Changement de cap et direction l'Université ! Pour avoir changé la trajectoire de ma vie et m'avoir ouvert les yeux sur le monde merveilleux de la recherche, je vous remercie Jesse Groenen.

Mes années universitaires ont été globalement joyeuses, bien que stressantes, notamment grâce aux soirées foot avec Clément et Mathieu, merci les amis !

Je tiens également à remercier les encadrants de mon mémoire à Lyon. Laurent, Leon et Sorin, vous êtes humainement incroyables et j'ai hâte de pouvoir collaborer de nouveau avec vous. Cela fait cinq ans que je ne pense qu'à cela !

Lorsque l'on est habitué au Sud de la France, passer quatre ans à faire une thèse dans un pays où la pluie est aussi omniprésente que la bière n'est pas chose aisée. Heureusement que les Buddy Buddy et la boulangerie Legrand m'ont aidé à surmonter cela.

Je n'oublie pas non plus mes deux anciens colocataires Denis et Gilles, et ceux avec qui j'ai partagé mon bureau, notamment Constantin et Laeticia. Merci à vous !

Pour avoir accepté de prendre de votre temps pour lire cette thèse de doctorat, pour avoir accepté de me donner vos opinions, je tiens à vous remercier, chers membres de mon jury. Notamment, je tiens à remercier mes deux superviseurs. Holger, merci pour votre patience concernant mes nombreuses questions, et surtout d'avoir réussi à répondre clairement à chacune d'entre elle. Miltos, vous êtes d'une disponibilité sans égale et on se voit tellement que je ne sais plus trop quoi dire ! Plus sérieusement, vous êtes celui qui a cru en moi, qui a misé sur moi pour ce projet, sans hésiter, alors que les autres ne voulaient pas de moi. J'étais très proche de faire une croix sur le monde de la recherche alors que je savais que j'étais fait pour cela. Vous m'avez permis d'avoir une seconde chance. Pour cette raison, je vous serai reconnaissant à jamais.

Je tiens également à remercier ma famille de m'avoir soutenu continuellement. J'ai forcément une pensée pour mes grands-parents qui sont décédés durant mes années étudiantes. Merci à vous de vous être si bien occupé de moi lorsque j'étais petit.

Je dédie cette thèse à mes parents pour leur amour inconditionnel. Papa, dès le départ, la vie ne t'a pas forcément fait que de cadeaux. Pourtant, tu as réussi à construire une belle famille et à transmettre à tes enfants ce que tu n'as pas pu avoir toi, merci pour cela. Maman, ton sens de la famille et ton amour pour les autres n'a pas d'égal. Malgré la distance, tu as toujours été là pour me conseiller, me comprendre lorsque moi-même je n'y arrivais pas et m'aider à réaliser mes objectifs. Je ne serais pas l'homme que je suis sans toi, tu es et restera toujours mon plus grand modèle, merci.

Enfin, je tiens à remercier ma compagne, fiancée et future épouse pour son soutien, ses conseils, et son amour, notamment lors de cette période critique de rédaction de thèse. Merci également pour la correction de ces remerciements. Au vu de toutes les fois, tous ces jours où je te parlais de flow electrification, je suis persuadé que tu connais mieux le sujet que moi, Miltos, et Holger réunis ! Merci pour tout Anastasiya.

Bonne lecture.

Contents

List of Figures

List of Tables

Nomenclature

Acronyms

ASM	Algebraic Stress Models
CFD	Computational Fluid Dynamics
CFL	Courant-Friedrich-Levy
DES	Detached Eddy Simulations
DL	Diffuse Layer
DNS	Direct Numerical Simulations
DSM	Differential Second-Moment
EDL	Electrical Double Layer
FCV	Fluctuating Charge-density Variance
IEA	International Energy Agency
ILES	Implicit Large Eddy Simulations
LES	Large Eddy Simulation
max	Maximum

MILES Monotonically Integrated Large Eddy Simulations

min Minimum

pafiX Particle Flow Simulation in Explosion Protection

PISO Pressure-Implicit with Splitting of Operators

r.m.s Root-mean-square

RANS Reynolds-Averaged Navier-Stokes

SGS Subgrid scale

SIMPLE Semi-Implicit Method for Pressure-Linked Equations

SIMPLEC Semi-Implicit Method for Pressure-Linked Equations-Consistent

SIMPLER Semi-Implicit Method for Pressure-Linked Equations Revised

TKE Turbulent Kinetic Energy

URANS Unsteady Reynolds-Averaged Navier-Stokes

Dimensionless numbers

$Lo = \frac{\rho U^2}{h\ \rho_{\mathrm{el}}\ E}$ Lorentz number

$Pe = \frac{\tau_{\mathrm{d}}}{\tau_{\mathrm{c}}}$ Peclet number

$Re_{\lambda} = \frac{h}{\lambda_{\mathrm{D}}}$ Debye number

$Re_{\tau} = \frac{u_{\tau} h}{\nu}$ Friction Reynolds number

$Re_{\mathrm{E}} = \frac{\tau_{\mathrm{e}}}{\tau_{\mathrm{c}}}$ Electric Reynolds number

$Re_{\mathrm{m}} = \frac{u_{\mathrm{m}} h}{\nu}$ Mean Reynolds number

$Sc_{\mathrm{s}} = \frac{\nu_{\mathrm{s}}}{D_{\mathrm{s}}}$ Subgrid Schmidt number

Notations

$\langle \psi \rangle$	Time and area average of a generic quantity
$\langle \rangle_t$	Time average of a generic quantity
$\langle \rangle_{xz}$	Area average (at the xz-plane) of a generic quantity
ψ'	Fluctuation of a generic quantity
ψ^*	Predicted value of a generic quantity (between the n-th and $n+1$-th level)
ψ^n	n-th time level of a generic quantity
ψ_{rms}	Root-mean-square of the fluctuating component of a generic quantity
$\widetilde{\psi}$	Filtered field of a generic quantity
y^+	Wall unit

Variables

$\boldsymbol{\tau}$	Residual stress tensor
$\boldsymbol{\zeta}$	Unclosed terms of the filtered charge-density equation
$\boldsymbol{E}$	Electric field
$\boldsymbol{F}_{\text{el}}$	Volumetric electric force
$\boldsymbol{J}$	Total current density
$\boldsymbol{J}_{\text{N}}$	Electric current densitiy for anions
$\boldsymbol{J}_{\text{P}}$	Electric current densitiy for cations
$\boldsymbol{S}$	Strain rate tensor
$\boldsymbol{u}$	Velocity field
Δt	Time step
Δx	Streamwise grid spacing

Δy	Cross-stream grid spacing
Δz	Spanwise grid spacing
Δ	Nominal filter width
δ_{ij}	Kronecker delta
ϵ	Electrical permittivity
η	Kolmogorov microscale
Γ	Flux limiter
γ	Thickness of the diffuse layer
λ_{ψ}	Taylor microscale
λ_{D}	Debye length
$\mathscr{A}_{\mathrm{e}}$	Advection term of the fluctuating charge-density variance budget
$\mathscr{C}$	Pressure diffusion term of the turbulent kinetic energy budget
$\mathscr{D}$	Molecular transport term of the turbulent kinetic energy budget
$\mathscr{D}_{\mathrm{e}}$	Molecular transport term of the fluctuating charge-density variance budget
$\mathscr{E}$	Dissipation term of the turbulent kinetic energy budget
$\mathscr{E}_{\mathrm{e}}$	Dissipation term of the fluctuating charge-density variance budget
$\mathscr{F}_{\mathrm{e}}$	Sink term of the fluctuating charge-density variance budget
$\mathscr{P}$	Production term of the turbulent kinetic energy budget
$\mathscr{P}_{\mathrm{e}}$	Production term of the fluctuating charge-density variance budget
$\mathscr{T}$	Turbulent transport term of the turbulent kinetic energy budget
$\mathscr{T}_{\mathrm{e}}$	Turbulent transport term of the fluctuating charge-density variance budget
μ	Dynamic viscosity

ν	Kinematic viscosity
ν_{s}	Subgrid-scale eddy viscosity
ω	Ion mobility
$\overline{T}$	Time-averaged period
ϕ	Electric potential
ρ	Mass density
ρ_{el}	Electric charge density
ρ_{w}	Charge density at the wall
σ	Electrical conductivity
τ_{c}	Charge-convection time scale
τ_{d}	Charge-diffusion time scale
τ_{e}	Charge-relaxation time scale
τ_{w}	Wall shear stress
C_{S}	Smagorinsky coefficient
D	Diffusion coefficient
D_{N}	Diffusion coefficient of anions
D_{P}	Diffusion coefficient of cations
D_{s}	Subgrid-scale eddy diffusivity
D_{t}	Turbulent eddy diffusivity
e_0	Elementary charge
h	Half-width of the channel
I	Total streaming current

I_0	Zeroth-order modified Bessel functions of the first kind
I_{DL}	Streaming current in the diffuse layer
K	Reaction rate of physico-chemical phenomena
k	Turbulent kinetic energy
K_0	Zeroth-order modified Bessel functions of the second kind
K_{B}	Boltzmann constant
L_{x}	Length of the channel
L_{z}	Depth of the channel
n_0	Total ionic concentration
n_{N}	Concentration of anions
n_{P}	Concentration of cations
N_{x}	Number of grid points in the streamwise direction
N_{y}	Number of grid points in the cross-stream direction
N_{z}	Number of grid points in the spanwise direction
p	Hydrodynamic pressure
Q	Total charge
Q_{DL^0}	Initial amount of charge in the diffuse layer
Q_{DL}	Amount of charge in the diffuse layer
r	Ionic radius
r_+	Ratio of successive gradients
T	Temperature
t	Time

U	Hydrodynamic velocity scale
u	Streamwise velocity
u_τ	Friction velocity
u_m	Mean velocity
v	Cross-stream velocity
w	Spanwise velocity
x	Streamwise direction
y	Cross-stream direction
z	Spanwise direction
z_N	Ionic valence
z_N	Valence of anions
z_P	Valence of cations

CHAPTER 1

Introduction

Context

We live in a world surrounded by petrochemicals. Vehicles, clothing, electronics, consumer products, food, and healthcare products contain petrochemicals. Therefore, it would be difficult, or impossible, to design a world without them. Although paradoxically, many people are unfamiliar with certain aspects of the petrochemical industry. In the aftermath of World War II, the consumption of petrochemicals increased dramatically. Unfortunately, as this sector expanded, accidents occurred more frequently. Various factors can explain these accidents, including gas leaks, but not only. In particular, handling petrochemicals in refineries and tankers caused many fires and explosions over the past 80 years.

Certain of these accidents were due to an electrokinetic effect, unknown at the time, called flow electrification. In order to avoid further disastrous consequences, this phenomenon has been extensively observed and studied by several authors since its discovery, namely in the 1940s. Nevertheless, despite the efforts of the scientific community, fundamental questions concerning the underlying mechanisms of flow electrification remain unanswered. This is mainly due to the complexity of turbulence, whether mathematical or numerical.

Nowadays, the design of advanced flow solvers and the ever-increasing power of modern computers have made it possible to study turbulent flows via numerical simulations. Accordingly, this thesis consists of an in-depth study of flow electrification in the case of low-conductivity (or, equivalently, dielectric) liquids, such as liquid hy-

drocarbons. More specifically, we use theoretical and numerical results to gain physical insight into the phenomenon of flow electrification in laminar and turbulent flow regimes.

In this first chapter, we provide the framework and the appropriate background knowledge of flow electrification. To this end, we first present an overview of the petrochemical industrial sector, *i.e.*, the sector in which this phenomenon is most likely to occur. Then, we describe the phenomenon of flow electrification through a detailed review of the relevant literature. Finally, we state the objectives of this thesis and outline its contents.

1.1 The petrochemical industrial sector

The occurrence of accidents in the petrochemical industrial sector combined with preconceived ideas, primarily due to a lack of information, may harm its image. As pointed out by Jarvis [1], transparency in the petrochemical and nuclear sectors is fundamental in ensuring the effective use of natural resources, thus restoring the reputation of these industries. In this context, we succinctly present the operating mode and history of the petrochemical industrial sector.

1.1.1 Types of petrochemicals

Petrochemicals are typically divided into three generations: feedstocks, intermediates, and finished products.

1. Earth naturally provides the feedstocks. Most of them emanate from natural gas and crude oils. However, there should be no underestimation of the significance of coal and biomass as feedstocks [2]. Natural gas is a combustible mixture of hydrocarbon (made entirely of carbon and hydrogen) and non-hydrocarbon compounds [3]. It consists primarily of methane (CH_4), while the non-hydrocarbon constituents include helium, nitrogen, and carbon dioxide (CO_2) [4]. Figure 1.1 illustrates the composition of natural gas from [4]. This circular diagram helps to appreciate the importance of each constituent. Nevertheless, it is worth pointing out that the composition of natural gas depends on its origin [5]. Similarly,

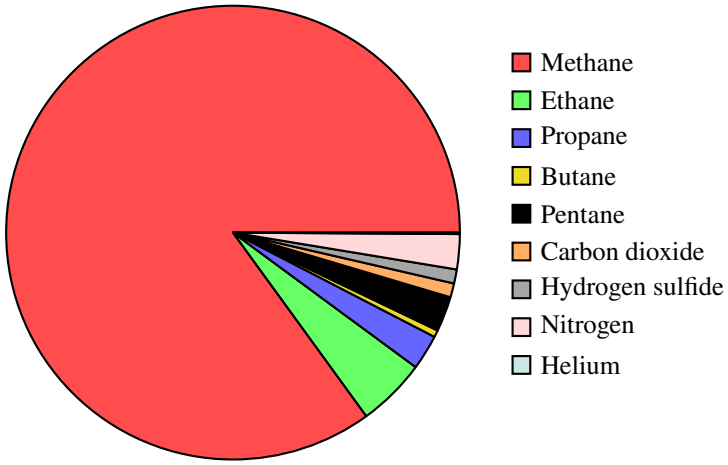

Figure 1.1: Composition of natural gas, obtained from [4].

hydrocarbons comprise most of the constituents of crude oils, followed by non-hydrocarbons and metallic compounds such as sodium, magnesium, and nickel.

2. Different chemical processes, such as steam and fluid catalytic crackings, produce second-generation petrochemicals; see, for example, [6, 7]. Herein, we only describe hydrocarbons since they constitute most of the intermediates. However, natural gas and crude oils can also produce non-hydrocarbon compounds, such as hydrogen, sulfur, carbon black, and synthesis gas [6]. Hydrocarbons are divided into aromatic and aliphatic compounds, described below.

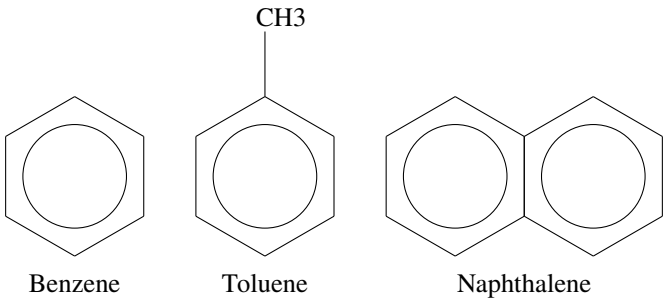

Figure 1.2: Molecular structures of benzene, toluene, and naphthalene.

Aromatic compounds are defined as hydrocarbons that contain the so-called aromatic ring, which corresponds to a circular chain of six carbon atoms with alternating double and single carbon-carbon bonds. Benzene (C_6H_6) is known to be both the simplest and most widely employed aromatic hydrocarbon [8]. Aside from certain molecules (*e.g.*, pyrrole, pyridine, ferrocene, chlorophyll a and b), nearly all aromatic hydrocarbons are derived from benzene [9]. For example, Figure 1.2 shows the molecular structures of benzene and two derivatives, namely toluene and naphthalene. According to it, we identify one and two benzene rings for toluene and naphthalene, respectively.

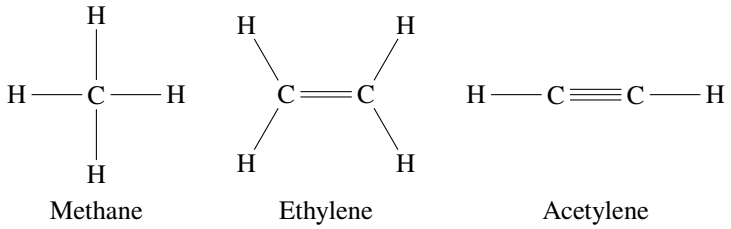

Figure 1.3: Molecular structures of methane, ethylene, and acetylene.

Aliphatic compounds are all the non-aromatic compounds. In particular, its molecular structure is either linear (acyclic) or cyclic but without a benzene ring. Additionally, aliphatic hydrocarbons are divided into several categories depending on their molecular structure. Alkanes have single carbon-carbon bonds, and their structure is serial, not cyclic; see the molecular structure of methane (CH_4) in Figure 1.3. Alkenes (respectively, alkynes), on the other hand, are aliphatic hydrocarbons in which at least one double (respectively, triple) bond links two carbon atoms. For visualization purposes, we provide in Figure 1.3 the molecular structures of ethylene (C_2H_4) and acetylene (C_2H_2), which are, respectively, the simplest alkane and alkyne.

3. Third-generation petrochemicals are derived from hydrocarbon intermediates. The different processes to produce them are numerous [6]. One can cite alkylation, chlorination, hydrogenation, nitration, and oxidation for benzene; *cf.* [6] and references therein. These finished (commercial) products include plastics, adhesives, soaps, explosives, foams, synthetic rubber, dyes, and others.

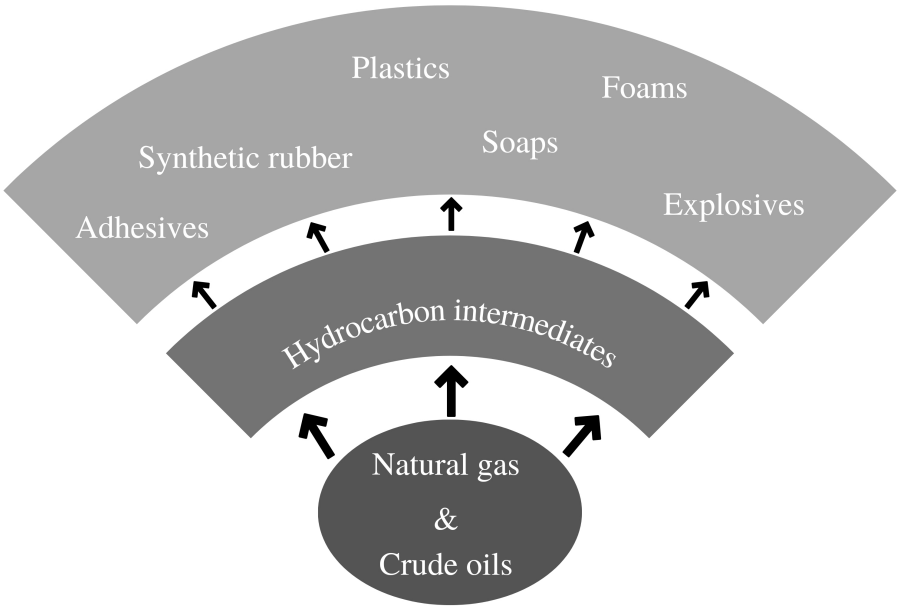

Figure 1.4: Simplified flowchart of petrochemicals, divided into three generations: feedstocks, intermediates, and finished products.

To summarize, Figure 1.4 illustrates a simplified petrochemical flowchart with the three generations described above. Please note that, in reality, the overall process is much more complex; see, for example, [6, 10, 11]. However, Figure 1.4 has the advantage of being simple while including the necessary details for understanding the operating mode of the petrochemical industrial sector.

1.1.2 Historical perspective

In the past, petrochemicals had not played such an essential role in the economy and society as they do today. The first chemistry-related event most likely occurred when Paleolithic people from France exploited coal as fuel [13]. Other archaeological evidence suggests the use of coal in olden times, notably in China [14] and Greece [15, 16]. However, it was only after the industrial revolution that coal became widely employed around the world, especially with the invention of steam engines by James Watt in 1776. At that time, coal, along with whale oil, overshadowed petroleum. Neverthe-

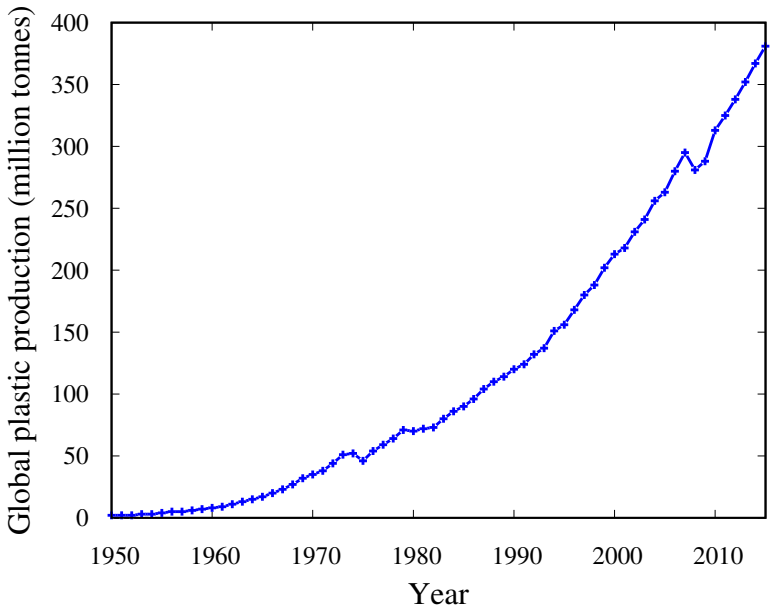

Figure 1.5: Evolution of the global plastic production from 1950 to 2015. The data are obtained from Geyer's work [12].

less, the latter gained popularity in the 19th century after the discovery of lamp oil, extracted from crude oils (petroleum) and used as a heating and lighting fuel. Soon afterwards, people built a variety of products other than fuels from petroleum, thus resulting in the emergence of the petrochemical industrial sector [17–20]. With time, petroleum and natural gas became more readily available. However, coal were extensively employed during World War II, especially by the nazi regime. According to Gillingham [21], in 1939, more than nine-tenths of the energy consumption in Germany came from coal. By contrast, at that time, in the United States, less than half of the energy consumption came from coal. Since the second half of the 20th century, petroleum has taken over coal as the principal source of chemicals. In particular, the steel crisis of 1973 exacerbated this trend [22]. Further, mass consumerism has characterized the second half of the 20th century, notably through the explosive growth of

plastics; see Figure 1.5. Subsequently, the petrochemical industry became the largest of the industrial chemical sectors [23].

In all likelihood, this trend will continue in the next few years. It is, therefore, necessary for the sector of the petrochemical industry to embrace a more sustainable environment. According to the International Energy Agency (IEA) [24], the industry has made several improvements, including mitigating air/water pollution and the water demand associated with primary chemical production. However, the most critical area of improvement in the petrochemical industrial sector concerns safety hazards. When the risks are not well assessed, handling petrochemicals can cause numerous accidents, such as fires and explosions. These accidents, in turn, release large quantities of pollutants into the environment. As Chen et al. [25] suggested, this can have disastrous effects on the local environment and health of the local human population. For example, during the *Deepwater Horizon oil spill* of 2010, over 200 million gallons of crude oil were released in the Gulf of Mexico [26].

In this context, prior research investigated in detail different methods concerning the identification, classification, and assessment of environmental risk sources; see [25, 27, 28] and references therein. Overall, these efforts helped different industries such as the petrochemical sector to correctly define the safety requirements and straightforwardly identify reference accident scenarios, as explained by Debray and Salvi [29]. These methods require reliable data, such as accident frequency rate, and a physical understanding of the phenomenon of interest. In this manner, one can determine critical factors influencing environmental risk.

1.1.3 Hazards and accidents due to flow electrification

The transport and storage of dielectric liquids can cause numerous accidents in the petrochemical industrial sector. In the 1950s, the origin of certain of these accidents was unknown. Consequently, identical accidents occurred in a short period. For example, in 1954, fires started in a Shell refinery at Pernis (Holland) 40 minutes after a liquid hydrocarbon (naphtha) blending operation. The following day, under the same conditions, fires started again [30]. These accidents were due to a phenomenon called flow electrification. A simple explanation is the following. During handling operations of dielectric liquids, electric-charge carriers accumulate and cause sparks in the

Figure 1.6: Static spark explosion of a chemical facility at Valley Center (Kansas, USA) in 2007 during a tank filling operation [34].

flowing liquid. These sparks may, in turn, generate fires and explosions, as illustrated, for example, in Figure 1.6. Since then, numerous accidents in the petrochemical industrial sector involving accumulation of charges in dielectric liquids were reported; see, for example, [31–33].

Hazards due to flow electrification do not necessarily involve fires and explosions. For example, flow electrification is deemed responsible for power transformer failures in the petrochemical industrial and nuclear sectors; see, for example, [35]. Although less dangerous for the local population than fires, the economic impact that power transformer failures have on the industrial sector is considerable.

Nowadays, although well-known by the principal actors in the petrochemical industrial sector, accidents due to flow electrification remain relatively unpredictable. This is primarily due to the lack of conclusive studies concerning the underlying mechanisms of this phenomenon. Hence, this thesis aims at filling this gap. To this end, in what follows, we provide some basic notions regarding flow electrification. Then, we detail earlier works and findings concerning this phenomenon.

1.2 Basic notions and earlier works

In this section, we list the principal types of electrokinetic phenomena and introduce some fundamental notions with regards to flow electrification, namely, the streaming current, the electrical double layer, and the Debye length. Then, we summarize the main results achieved by different authors in the past 80 years, corresponding to the discovery of the phenomenon of flow electrification.

1.2.1 Electrokinetic phenomena

Electrokinetic phenomena refer to the relative motion of two phases along their interface [36]. These two phases are, in general, solids and liquids containing impurities. Electrokinetic phenomena fall into four main groups, listed below.

1. Electro-osmosis. This phenomenon refers to the motion of a liquid along the charged solid surface induced by an externally applied electric field [37]. The main application for electro-osmosis consists of dewatering soils, sediments, and sludge. In this manner, it allows the remediation of hazardous waste contaminated soils [38, 39].

2. Electrophoresis. This concerns the movement of solid particles containing ions in the fluid caused by an electric field [37]. In a similar manner to chromatography, this phenomenon allows the identification of a mixture via the separation of particles. For example, electrophoresis is employed in genetics to separate and analyze nucleic acids [40].

3. The sedimentation potential. This phenomenon, also known as the *Dorn effect*, occurs when gravity or centrifugation results in the motion of sedimenting solid particles in the solution, thus generating an electric field [41]. Similar to electrophoresis, a well-known application of this phenomenon concerns particle size analysis via a separation technique called Sedimentation Field Flow Fractionation (SFFF) [42].

4. Streaming potential/current. The streaming potential/current is an electric current that is generated when a liquid moves along a flat surface [43]. Areas of application are typically the control of the coagulation process in wastewater

treatment plants [44, 45]. More specifically, the streaming potential measure the degree of coagulation of raw water.

Additionally, secondary groups complete the family of electrokinetic phenomena, namely, capillary osmosis, colloid vibration, diffusiophoresis, and electric sonic amplitude; see [46] and references therein.

1.2.2 Electrical double layer

Although they are different in nature, all electrokinetic effects stem from a common source: the *electrical double layer* (EDL). It consists of a region located at the interface of two phases (liquid/solid). The development and structure of the EDL has been the topic of several studies in the past. These studies resulted in the development of a number of theories of the EDL of different levels of complexity and precision.

Initially, Helmholtz [47] assumed the existence of two layers of opposite polarity at the interface. However, Helmholtz's model did not consider certain critical factors, such as the diffusion and mixing of ions in the solution. Subsequently, Gouy [48] and Chapman [49] introduced a diffuse model for the EDL. In particular, from Maxwell-Boltzmann statistics, it is possible to measure the electric potential in the diffuse layer. Afterwards, Stern [50] proposed a theory that combined elements of the previous two models.

In Stern's theory, the EDL consists of two parallel charge layers. The first layer, located on the side of the solid, is called the *surface charge*. Inside, ions share the same sign (positive or negative); see bottom of Figure 1.7. The second layer is on the liquid side and consists of two sublayers: the *Stern* and *diffuse layers*; see the colored part in Figure 1.7. In the Stern layer, ions have the opposite sign to those located in the surface charge. The thickness of this sublayer is so thin that inside, ions are not affected by the flow. More specifically, the electrical properties of the Stern layer are constant with time, such as the concentration of ions and their signs. On the other hand, the concentration of ions decreases away from the solid surface, as illustrated in Figure 1.7.

Since then, several theories have emerged to extend Stern's model [51–55]. One of the most significant advancements concerning the EDL is that of Marcus [56] for its explanation of the rates of electron transfer reactions. Marcus [56] was awarded the

1992 Nobel Prize in Chemistry for the development of his EDL theory. For a general description of the Marcus model, the interested reader is referred to his Nobel-Prize lecture [56]. More recently, Wang and Wang [57] introduced the notion of the hybrid EDL. Wangs' theory, in contrast to previous models, proposes the transfer of electrons at the interface, which has been verified experimentally by Lin et al. [58] and Nie et al. [59]. For visualization purposes, we have plotted in Figure 1.7 the representation of the EDL from Wangs' model. We observe the presence of electrons in the surface charge while the configuration of ions in both Stern and diffuse layers follow Stern's model, described above. As explained by Wang and Wang [57], the formation of the EDL consists of two steps. First, the transfer of electrons at the interface leads to the development of ions on the solid surface. These ions cause the migration of opposite ions in the solution towards the interface. Then, the electrostatic interactions result in the formation of the EDL.

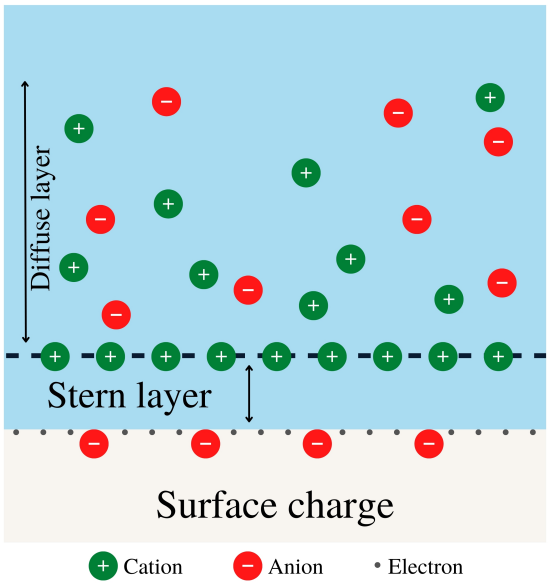

Figure 1.7: Representation of the EDL through Wang's model [57].

1.2.3 Flow electrification

Flow electrification occurs when a flowing liquid, in contact with a solid, transports electric-charge carriers (ions) from the diffuse layer towards the bulk of the flow domain. Generally, in the petrochemical industrial sector and most laboratories, the ions originate almost exclusively from impurities. There can be many different sources of impurities: during the production of the liquid, during its initial storage, and so on. In particular, according to Touchard [60], additives can be put intentionally to reduce the liquid conductivity. Consequently, an accurate characterization of these impurities is not readily available, as suggested by Abedian and Sonin [61]. Further, flow electrification falls into the last category of electrokinetic phenomena described in section 1.2.1. More specifically, the motion of the liquid, in contact with the solid, generates a streaming current in the liquid. The latter measures the concentration of electric-charge carriers convected by the flow. On another note, this convection of charge in the liquid is deemed responsible for several major electrostatic accidents. For example, Klinkenberg's report [30] includes graphic descriptions of explosions of tanks filled with petroleum products. More recently, Ohsawa [62] presented a statistical analysis of fires and explosions in Japanese refineries from 1960 to 2010.

Several parameters influence the streaming current, including the thickness of the electrical double layer and the initial concentration of impurities in the liquid. On the one hand, the thickness of the Stern layer corresponds to a few Angstroms, *i.e.*, an ionic radius. Concerning the diffuse layer, its thickness relies on a quantity called *Debye length*, based on the electrical properties of the medium [63]. Notably, the Debye length is proportional to the square root of the electrical resistivity of the liquid. In general, the order of magnitude of the Debye length corresponds to a few microns for aqueous solutions. However, certain fluids of particular importance to the petrochemical industrial sector have high electrical resistivity. Typical examples include liquid hydrocarbons such as benzene, heptane, or toluene. In other words, the diffuse layer's thickness may be significant for these liquids. Therefore, it is expected that flow electrification primarily occurs in handling operations of low-conductivity liquids (*i.e.*, dielectric liquids) such as tanks filled with hydrocarbons. Please note that, for chemically pure dielectric liquids, such impurities should not exist. Nonetheless, for liquid hydrocarbons in the petrochemical industrial sector, the concentration of these impurities is

sufficiently large to result in the development of the diffuse layer (at the liquid/solid interface) and the generation of a streaming current (once the liquid becomes to flow); see, for example, [64].

1.2.4 Earlier research

Probably the earliest study of flow electrification was that of Dolezalek [65] on benzene and ether flows in metal pipes. This phenomenon, yet unknown, has gained increasing attention over time. More specifically, the rise of electrostatic accidents in the petrochemical industrial sector has spurred several authors to describe flow electrification [30, 66–73].

Cooper [64] explained flow electrification through the classical theory of streaming potential [47]. That author obtained an expression of the streaming current by using the Helmholtz-Smolucowski equation for the zeta potential. The latter corresponds to the electric potential at the interface between the diffuse layer and the bulk of the flow domain. This formulation helped quantity laminar flow electrification of aqueous solutions in tubes. However, the classical theory of streaming potential neglects the influence of the liquid conductivity on the thickness of the diffuse layer of the EDL, as pointed out by Rutgers et al. [73]. Notably, the Helmholtz-Smolucowski equation is not valid in the case of diffuse layers involving hydrocarbons because these substances have large Debye lengths. Additionally, classical EDL theories predict a discontinuous charge-density profile, contradicting earlier observations [74]. Consequently, the theories based on the classical Helmholtz-Gouy model (*i.e.*, by using the Helmholtz-Smolucowski equation) fail to explain flow electrification of liquid dielectrics. To remedy this, two theories have been proposed and described below.

Theory 1: from Gavis and Koszman [74] to Abedian and Sonin [61]

Gavis and Koszman [74, 75] studied turbulent flow electrification of low-conductivity liquids in metallic tubes. They based their theory on conservation equations for anions and cations. These equations consider the transport of ions by conduction, diffusion, and convection. Further, their theoretical development was based on several hypotheses. These are the following.

H1. The *valence* of each ion, defined by Parkin [76] as " the number of electrons that an atom uses in bonding", is set equal to unity.

H2. The electrical conductivity of the liquid is constant and non-zero.

H3. The diffusion coefficients of cations and anions are equal.

H4. The concentration of ions at the wall is constant.

H5. The time-averaged equation for the electric charge density is approximated through a "gradient assumption". This assumption accounts for the loss of turbulent effects (due to the averaging) by introducing a quantity called *eddy diffusivity*. The eddy diffusivity is related to the intensity of the flow and operates as an additional diffusion process. In other words, the resulting diffusion coefficient in the time-averaged charge-density equation corresponds to the sum between the initial diffusion coefficient and the eddy diffusivity.

H6. The *effective diffusion sublayer* corresponds to a region adjacent to the wall, where the turbulence intensity of the flow does not affect the electric charge-density distribution. Therefore, the eddy diffusivity is negligible inside this zone.

H7. The effective diffusion sublayer is thinner than the diffuse layer.

H8. The charge density of liquids with very low electrical conductivity is constant in the radial direction [75].

Hypotheses H1-H3 allow the derivation of a unique conservation equation for the electric charge density. Then, by virtue of H4-H8, Gavis and Koszman [74, 75] solved the time-averaged transport equation for the electric charge density. By multiplying the radially uniform charge density (H8) with the averaged velocity, Gavis and Koszman [75] derived an expression for the streaming current. Furthermore, these findings were consistent with most experimental and observational data for turbulent liquid hydrocarbon flows [65–70, 72, 73, 77–85]. Nonetheless, the applicability of this formulation is limited to low-conductivity liquids in circular tubes, mainly because of H8.

Twenty years later, Abedian and Sonin [61] extended the theory of Gavis and Koszman. Those authors derived a closed-form expression for the streaming current and the

electric charge density in turbulent (circular) pipe flow. In their formulation, they did not impose any assumptions regarding the electrical conductivity of the liquid. In fact, Abedian and Sonin [61] presented a case study depending on three parameters: the Debye length, the pipe radius, and the thickness of the effective diffusion sublayer. For example, the expressions obtained by Cooper [64] for aqueous solutions and Koszman and Gavis [75] for very low-conductivity liquids appear as limiting cases. In a subsequent paper, Abedian and Sonin [86] demonstrated that their expression for the streaming current compares favorably with available experimental data, including those of Hampel and Luther [71] for materials with long Debye lengths.

In their analysis, Abedian and Sonin [61] assumed hypotheses H1-H6 to be valid. Additionally, they cast the eddy diffusivity in terms of the distance from the wall. This continuous profile depends on three regions. First, the eddy diffusivity is negligible in the effective diffusion sublayer, as suggested by Koszman and Gavis [75] through hypothesis H6. Then, in the second region, it increases linearly with the distance from the wall. Finally, the eddy diffusivity becomes constant in the third zone. Nonetheless, it is worth adding that the value of this constant increases proportionally with the turbulence intensity of the flow.

Further, Abedian and Sonin [61] pointed out that the derivation of the expression of the streaming current in [75] does not require hypothesis H8. Instead, it is sufficient to add in H7 a condition on the ratio between the Debye length, the pipe radius, and the thickness of the diffuse sublayer. Those authors also assumed the following.

H9. The electric charge density is small inside the liquid. In particular, the difference between anion and cation concentrations is much smaller than their sum.

H10. Outside the effective diffusion sublayer, the mean axial velocity profile is constant; inside, it is linear.

The inequality in H9 constrains the conductivity of the liquid to be constant. As a result, it allows the explanation of hypothesis H2. Also, Abedian and Sonin [61] assumed an overly simplified profile for the mean axial velocity via hypothesis H10. Indeed, the closed-form expression for the electric charge density can only be obtained by virtue of the above simplifying hypothesis. Due to this, those authors fell short of providing physical insight of the underlying mechanisms of turbulent flow electrification.

Theory 2: from Boumans [87] to Touchard [88]

Boumans [87, 89, 90, 91] described the phenomenon of flow electrification in circular tubes through the Debye-Hückel equation for the electric potential. More specifically, that author estimated an expression for the electric charge density and the streaming current in the diffuse layer. Hence, the two theories initiated by Gavis and Koszman [74, 75] and Boumans [87, 89–91] do not rely on the same equations to describe flow electrification. Moreover, Boumans mainly focused on the diffuse layer and its perturbation. Essentially, this is where the two theories diverge.

- Part I: charge-density distribution in a fully developed diffuse layer

Later on, Touchard [92] undertook Boumans' work and expanded it. Unlike Abedian and Sonin [61], the conservation equation for the electric charge density does not consider transport of ions by convection. That author justified this by invoking the following *ad hoc* hypothesis.

H11. The diffuse layer is fully developed. As a result, the total charge density in the diffuse layer remains constant, regardless of the flow regime.

Accordingly, Touchard [92] determined a closed-form solution of the electric charge density for a fluid at rest in the diffuse layer. Based on hypotheses H1-H4 and the "weak space-charge density assumption", equivalent to H9, the electric charge density is given in terms of modified Bessel functions. In the same paper, Touchard also studied the charge distribution in the diffuse layer and the influence of the flow on it. On the one hand, a laminar flow does not modify the electric charge density, resulting in a profile similar to that in a liquid at rest. Turbulent mixing, on the other hand, homogenizes the electric charge density, except in the near-wall regions, analogous to the effective diffusion sublayer. Touchard [92] estimated numerically the value of the constant charge density so that the total charge in the diffuse layer remains constant, *i.e.*, so that H11 holds. However, this hypothesis resulted in a discontinuous charge distribution at the point where the first zone ends and the second one begins.

Cabaleiro et al. [93] remedied the discontinuous profile by assuming that the total charge in the diffuse layer and the streaming current increase with the turbulence intensity of the flow, contradicting H11. Nevertheless, similarly to Touchard [92], those

authors failed to consider transport of ions by convection. Instead, Cabaleiro et al. [93] included an eddy diffusivity in the time-averaged charge-density equation. Please note that their expression for the eddy diffusivity differs from that of Abedian and Sonin [61]. In particular, Abedian and Sonin [61] derived a closed-form expression for the electric charge density, in contrast to Cabaleiro et al. [93]. Further, via the numerically computed profile of the electric charge density, Cabaleiro et al. [93] suggested that four parameters influence the streaming current: the pipe radius, the electric charge density at the wall, the flow velocity, and the perturbed region by turbulence.

Very recently, Touchard [88] proposed to combine the two models described above (*i.e.*, [92, 93]). Subsequently, that author separated the diffuse layer into two regions. First, turbulence does not affect the charge-density distribution in the effective diffusion sublayer, as in [92]. In the second region, Touchard [88] introduced the eddy diffusivity in the time-averaged charge-density equation, as in [93]. Once again, the (numerical) estimation of the electric charge density resulted in a discontinuity at the junction of the two zones because that author assumed H11 to be valid.

In a subsequent paper, Touchard [94] compared the predictions of the three models discussed above [88, 92, 93] with experimental data obtained by that author on cryogenic liquids flow electrification. In spite of the discontinuity in the charge-density profile, the predictions of Touchard [88, 92] agree better with the experimental data than the one Cabaleiro et al. [93] does. However, according to Touchard [94], these data should be considered with caution due to the complex experimental facility and protocol. Among these difficulties were preserving a constant concentration of impurities (to ensure reproducible experiments) and minimizing reactions between the liquid and materials in contact with it. Consequently, the experimental data yielded significantly dispersed results. This, in turn, prevented the development of a more realistic model (*i.e.*, without discontinuity).

- Part II: development of the diffuse layer via physico-chemical phenomena

Further, Touchard and his team also studied physico-chemical phenomena at the liquid/solid interface [95–98]. More specifically, they developed a theoretical model of the EDL development and described the influence of this evolution on flow electrification via the streaming current. In this context, hypothesis H11 is no longer required. Accordingly, Touchard et al. [95] presented the first physico-chemical model for hydro-

carbon liquids flowing through circular pipes. These reactions occur at the interface via the dissociation and recombination of additives, also known as the *corroding model*. In addition to hypotheses H1-H4 and H9, the authors assumed the following.

H12. Inside the liquid, only one type of impurity (or additive) is dissociated. Moreover, the impurity exhibits a weak dissociation rate.

By virtue of H1-H4, H9, and H12, Touchard et al. [95] derived an expression for the *wall-current density*. Mathematically, the wall-current density corresponds to the time-derivative of the total charge in the diffuse layer. For example, the wall-current density equals zero when the diffuse layer is fully developed (*cf.* H11). This quantity was first introduced by Boumans [87] to correct classical EDL theories, including that of Cooper [64], described above.

Accordingly, Touchard et al. [95] suggested that the wall-current density is proportional to a coefficient, denoted by K, related to the intensity of the physico-chemical phenomena. By virtue of H4, this coefficient is considered constant. In the same paper, via the wall-current density, Touchard et al. [95] estimated the evolution of the electric charge density during the development of the diffuse layer. However, Cabaleiro et al. [96] used experimental results to highlight the limits of Touchard's model in channel flows. In particular, those authors indicated that the coefficient K varies linearly with the mean flow velocity. One possible explanation for this concerns the validity of hypothesis H4. More specifically, Cabaleiro et al. [96] supposed that the concentration of cations at the interface is not constant but depends on the flow velocity. Through a new expression for the coefficient K based on experiments with metallic capillaries, Paillat et al. [97] rectified Touchard's corroding model. Further, Leblanc et al. [99] investigated the validity of the coefficient K for mineral oil flowing through stainless steel capillaries. Similarly, El-Adawy et al. [100, 101] and Ela et al. [102] studied physico-chemical phenomena at the interface between dielectric liquids in contact with dielectric solids.

The corroding model is one of many ways to represent physico-chemical phenomena at liquid-solid interfaces. One can also mention, for instance, the *adsorption model* introduced by Walmsley and Woddford [103] and taken up recently by Leblanc et al. [98]. In this case, anions are adsorbed at the solid surface, in contrast to the corroding model. Washabaugh and Zhan [104], on the other hand, presented a *hybrid model* of

adsorption and corrosion. Later on, the validity of models for the EDL development was tested via experimental data and measurements of the streaming current in simple cross-sectional geometries (channel, square duct, circular pipe); see [33, 60, 85, 105–113].

- Part III: flow electrification in other flow domains

In addition, several authors discussed the generation of electric charge in flow of low-conductivity liquids (liquid hydrocarbons) through wire mesh screens [114, 115], filters [116, 117], and (micro)porous media [118–120]. However, as explained by Miaoulis et al. [114], due to the complexity of flow structures in such media, these studies were mostly experimental. In addition, many authors studied flow electrification in power transformers [35, 121–129], mainly because this phenomenon is deemed responsible for power transformer failures. Consequently, a team in the laboratory of Poitiers University developed a "capacitive sensor". As indicated by Paillat et al. [120], the aim of this machine is to prevent future electrostatic accidents through a measure of flow electrification.

To summarize, flow electrification has been the subject of numerous research efforts. Except for Abedian and Sonin [61], the models described above did not consider the appropriate equation for the electric charge density based on the conduction, diffusion, and convection of ions. In this manner, the numerical treatment of the electric charge-density equation is eased since there is no coupling with the Navier-Stokes equations. Nevertheless, not including the convective term resulted in unphysical outcomes, such as a discontinuous profile for the electric charge density in [88, 92]. With regards to the work of Abedian and Sonin [61], the simplified profiles of the mean axial velocity and the eddy diffusivity significantly restricted the influence of small-scale turbulent structures on flow electrification, located in the near-wall regions.

Additionally, earlier studies mostly focused on measuring flow electrification by determining the streaming current. However, the phenomenon of flow electrification should not be limited to this. In particular, no study has examined the transport of charge induced by turbulence from the diffuse layer towards the bulk of the flow domain, nor the build-up of electric-charge carriers. Instead, all studies assumed that flow electrification has occurred. Consequently, prior studies have failed to adequately identify the role of turbulence in flow electrification. Notably, no investigation has

analyzed statistical properties of the electric charge density, such as potential fluctuations induced by turbulence. Accordingly, this thesis aims to fill this gap by presenting Direct Numerical Simulations (DNS) and Large Eddy Simulations (LES) of electric charge transport in turbulent channel flows of dielectric liquids.

1.3 Objectives and outline of the thesis

In this work, we develop a theoretical and numerical framework for flow electrification of liquid dielectrics in channel flows that can be further extended at other geometries (square duct, circular pipes) in a straightforward manner. Concerning the numerical treatment, in the recent past, advancements in algorithm development have enabled the numerical study of various problems arising in electrohydrodynamics. These algorithms have two coupled components: one solver for the fluid-flow equations (typically the Navier-Stokes equations) and another one for the governing equations of electrostatics; see, for example, [130, 131]. Our algorirthm and the related code development has become part of pafiX [132], which is a computational tool for the simulations of powder and fluid-flow operations in process industries with an emphasis on phenomena that represent a hazard to operational safety. Accordingly, we set the following objectives:

1. Develop an accurate and robust algorithm for the governing equations of hydrodynamics and electrostatics.

2. Study the charge-density distribution in the diffuse layer in terms of the flow regime.

3. Investigate the characteristics of turbulent flow electrification and the influence of convection, conduction, and diffusion of electric-charge carriers on it.

4. Develop a cost-effective subgrid-scale model for the charge-density equation, allowing a further study of flow electrification at higher turbulence intensities.

This thesis is structured as follows. Chapter 2 describes the governing equations for the flow under study, namely the incompressible Navier-Stokes equations and the electrostatic equations. We also elaborate on the spatial and temporal discretization of these equations. Furthermore, we identify and discuss the principal nondimensional groups

of the governing equations. Then, we describe in detail our implementation of their numerical treatment. Finally, we present the computational setup, including the material properties of the liquid of interest, the geometry of the flow domain, and the boundary conditions.

In Chapter 3, we examine the charge-density distribution in the diffuse layer in terms of the flow regime. In the case of a liquid at rest and in laminar flow, we predict the analytical expression of the electric charge density. We also present an analysis for the thickness of the diffuse layer. Additionally, we provide the formulation of the streaming current in the case of a laminar regime. Then, we study the influence of turbulence on the charge-density distribution via DNS at low to moderate turbulence intensities.

Chapter 4 presents an in-depth analysis of turbulent flow electrification via DNS. We separate these simulations into two groups. With the first group, we investigate the influence of the turbulence intensity in flow electrification. Through the second group, we study the effects of the Debye length, the electrical conductivity, and the diffusion coefficient in turbulent flow electrification. To this end, we compare fundamental statistical quantities, such as the mean and the standard deviation of the electric charge density. It is worth pointing out that, to our knowledge, there is no reliable experimental data in the literature. Therefore, our findings serve as a reference point for future work.

In Chapter 5, we employ the LES approach to study turbulent flow electrification at higher turbulence intensities. Accordingly, we present different subgrid-scale eddy-diffusivity models for the filtered charge-density equation. Then, we compare these models with the database obtained in Chapter 4. Upon validation, we conduct LES. Accordingly, these simulations contribute to a better understanding of the underlying mechanisms of turbulent flow electrification.

Finally, Chapter 6 concludes and elaborates on future perspectives.

CHAPTER 2

Governing equations and numerical modeling

2.1 Introduction

This chapter presents in a detailed manner the theoretical and numerical framework for the problem in hand, namely flow electrification of liquid dielectrics in wall-bounded flows. The system of governing equations consists of two different parts. The first one concerns the motion of the fluid, regarded as a continuous medium. It includes the mass (or continuity) and momentum equations, commonly called the *Navier-Stokes equations*. The second part of the system of governing equations involves the electric charge density in the liquid via a charge conservation equation. In addition, the equations are coupled via an extra force in the momentum equations and a convective term in the charge conservation equation.

Since the diffuse layer is adjacent to the wall, it is expected that small-scale turbulent structures near the viscous sublayer play a significant role in flow electrification. For this reason, the predictive capacity of approaches based solely on the mean velocity profile, as employed by Abedian and Sonin [61] and Touchard [88, 92], has certain limitations. On another note, as described in section 1.3, modern computers and advanced flow solvers have enabled numerical simulations of turbulent flows. Accordingly, these simulations consider the small-scale structures of the flow, either by resolving them or modeling their effects.

Therefore, one can provide significant new physical insight into the underlying mechanisms of the phenomenon of interest. This approach, however, requires the design of efficient numerical algorithms for the system of governing equations. López-Herrera et al. [130] and Roghair et al. [131] developed numerical algorithms for electrohydrodynamics. Nevertheless, these algorithms do not consider mechanisms for charge generation at solid boundaries and charge diffusion away from them.

In this chapter, we present an algorithm for computational electrohydrodynamics that is well suited for the study of flow electrification and, more generally, for wall-bounded flows of dielectric liquids. We implemented this algorithm in pafiX, which is a recent computational tool developed by Grosshans [132] in the federal metrology institute (PTB) with additional contributions from UCLouvain, including the author of the present thesis. Notably, pafiX is available as freeware and has been developed specifically for studying powder and fluid flows under conditions involving operational safety hazards.

2.2 Governing equations

This section describes the governing equations of electrohydrodynamics for incompressible flows. As mentioned above, this system consists of two coupled parts, namely, the Navier-Stokes equations (supplemented with a volumetric electric force), and the charge conservation equation.

2.2.1 Hydrodynamic equations

Throughout this thesis, we consider a fluid with constant mass density and temperature. Accordingly, the conservation equations for mass and momentum read in dimensional form,

$$\nabla \cdot \boldsymbol{u} \;=\; 0\,, \tag{2.1}$$

$$\frac{\partial \boldsymbol{u}}{\partial t} + (\boldsymbol{u}\cdot\boldsymbol{\nabla})\boldsymbol{u} \;=\; -\frac{1}{\rho}\boldsymbol{\nabla} p + \nu\nabla^2\boldsymbol{u} + \frac{1}{\rho}\boldsymbol{F}_{\mathrm{el}}\,, \tag{2.2}$$

where $\boldsymbol{u} = (u, v, w)$, ρ, p, and ν represent the velocity field, the (mass) density, the dynamic pressure, and the kinematic viscosity of the fluid, respectively. The derivation

of the Navier-Stokes equations is elaborated in standard textbooks [133–136] and is not provided herein.

Further, $\boldsymbol{F}_{\text{el}}$ stands for the volumetric electric force. Castellanos [137] added this quantity to the momentum equations to improve the dielectric electrohydrodynamic model suggested by Melcher and Taylor [138]. This force is due to the sum between a non-homogeneous dielectric permeability and free charge, namely,

$$\boldsymbol{F}_{\text{el}} \;=\; -\frac{1}{2}\,(\boldsymbol{E}\cdot\boldsymbol{E})\,\boldsymbol{\nabla}\epsilon + \rho_{\text{el}}\,\boldsymbol{E}\,, \tag{2.3}$$

where $\boldsymbol{E}$, ϵ, and ρ_{el} denote, respectively, the electric field, the electrical permittivity, and the electric charge density. In this study, we also assume constant electric properties, which results in a simplified formulation for the volumetric electric force,

$$\boldsymbol{F}_{\text{el}} \;=\; \rho_{\text{el}}\,\boldsymbol{E}\,. \tag{2.4}$$

As it stands, the contribution of this force has been proven to be negligible everywhere in the flow domain, except at the interface between two liquids [130]. Since this study focuses uniquely on single-phase fluid flows, it is reasonable to consider that the volumetric electric force has imperceptible effects on fluid motions. As a matter of fact, all the simulations considered herein confirmed this trend. Nonetheless, we retain this term in the governing equations for completeness purposes.

2.2.2 Electrostatic equations

In this section, we derive the governing electrostatic equations. It consists of one equation for the electric potential ϕ and another one for the electric charge density ρ_{el}. In the applications of interest, dynamic currents due to charge transport are insignificant, resulting in negligible effects of electromagnetic induction [139]. Subsequently, we simplify the laws of electrodynamics to those of electrostatics. In particular, the electric field $\boldsymbol{E}$ satisfies Gauss' law,

$$\nabla\cdot\boldsymbol{E} \;=\; \frac{\rho_{\text{el}}}{\epsilon}\,. \tag{2.5}$$

In the electrostatic approximation, the electric field is irrotational. Thus, we can express $\boldsymbol{E}$ in terms of the gradient of the electric potential ϕ,

$$\boldsymbol{E} \;=\; -\nabla\phi\,. \tag{2.6}$$

Accordingly, Gauss' law reduces to the following Poisson equation,

$$\nabla^2 \phi \;=\; -\frac{\rho_{\mathrm{el}}}{\epsilon}\,. \tag{2.7}$$

As explained in Chapter 1, our study focuses on liquid dielectrics. Theoretically and for a perfect liquid dielectric, it is impossible to detect any electrohydrodynamic effects, hence no flow electrification. However, in practice, we observe the presence of impurities that can dissolve in such materials. In this manner, ions participate in the electrochemical reactions at the liquid/solid wall interface, leading to the formation of the EDL; *cf.* section 1.2.2. At typical impurity concentrations, neutral electronacceptor molecules trap free electrons inside the liquid [137], constraining them to be only present at the surface charge, as illustrated in Figure 1.7. Consequently, we may consider only ions (cations and anions) as impurities inside the liquid. The electric charge density ρ_{el} for the flows of interest is then given by [140],

$$\rho_{\mathrm{el}} \;=\; \sum_{\mathrm{P}} e_0 z_{\mathrm{P}} n_{\mathrm{P}} - \sum_{\mathrm{N}} e_0 z_{\mathrm{N}} n_{\mathrm{N}}\,, \tag{2.8}$$

where n_{P} and n_{N} represent, respectively, the concentrations of cations and anions in the liquid, while e_0 corresponds to the elementary charge. In addition, z_{P} and z_{N} denote, respectively, the absolute values of the valences of cations and anions. Then, we define the electrical conductivity as [140],

$$\sigma \;=\; \frac{e_0^2}{K_{\mathrm{B}} T}\left(D_{\mathrm{P}} z_{\mathrm{P}}^2 n_{\mathrm{P}} + D_{\mathrm{N}} z_{\mathrm{N}}^2 n_{\mathrm{N}}\right)\,, \tag{2.9}$$

where D_{P} and D_{N} stand for, respectively, the diffusion coefficient of a cation and an anion in the liquid. Further, K_{B} represents the Boltzmann constant, while T is the temperature of the liquid, which is assumed to be constant. The specific electric current densities for cations and anions read [140],

$$\boldsymbol{J}_{\mathrm{P}} \;=\; -e_0 z_{\mathrm{P}} D_{\mathrm{P}} \boldsymbol{\nabla} n_{\mathrm{P}} + \frac{e_0^2 z_{\mathrm{P}}^2 D_{\mathrm{P}} n_{\mathrm{P}}}{K_{\mathrm{B}} T} \boldsymbol{E} + e_0 z_{\mathrm{P}} n_{\mathrm{P}} \boldsymbol{u}\,, \tag{2.10}$$

$$\boldsymbol{J}_{\mathrm{N}} \;=\; e_0 z_{\mathrm{N}} D_{\mathrm{N}} \boldsymbol{\nabla} n_{\mathrm{N}} + \frac{e_0^2 z_{\mathrm{N}}^2 D_{\mathrm{N}} n_{\mathrm{N}}}{K_{\mathrm{B}} T} \boldsymbol{E} - e_0 z_{\mathrm{N}} n_{\mathrm{N}} \boldsymbol{u}\,. \tag{2.11}$$

In each of equations (2.10) and (2.11), the first term on the right-hand side represents ionic diffusion, the second term expresses ionic migration, and the third one describes

ionic convection. Additionally, we define the total (electric) current density, $\boldsymbol{J}$, as the sum of the specific electric current densities for cations and anions, namely,

$$\boldsymbol{J} \;=\; \sum_{\mathrm{P}} \boldsymbol{J}_{\mathrm{P}} + \sum_{\mathrm{N}} \boldsymbol{J}_{\mathrm{N}} \,. \tag{2.12}$$

Then, the conservation equation for the electric charge density reads,

$$\frac{\partial \rho_{\mathrm{el}}}{\partial t} + \nabla \cdot \boldsymbol{J} \;=\; 0 \,. \tag{2.13}$$

In order to simplify the expression for $\boldsymbol{J}$, hence for (2.13), we introduce herein the following assumptions:

i. The ionic valences are all equal to a specific value, often unity, denoted by z,

$$z_{\mathrm{P}} \;=\; z_{\mathrm{N}} \;=\; z \,. \tag{2.14}$$

ii. The diffusion coefficients of all ionic species are equal, denoted by D,

$$D_{\mathrm{P}} \;=\; D_{\mathrm{N}} \;=\; D \,. \tag{2.15}$$

iii. The sum of the concentration of cations and anions is much higher than their difference,

$$\sum_{\mathrm{P}} n_{\mathrm{P}} + \sum_{\mathrm{N}} n_{\mathrm{N}} \;>>\; \sum_{\mathrm{P}} n_{\mathrm{P}} - \sum_{\mathrm{N}} n_{\mathrm{N}} \,. \tag{2.16}$$

These assumptions are commonly employed in studying flows in the presence of electrostatic fields. They are deemed valid for the fluid of interest, corresponding to dielectric liquids. Please note that in the flow of interest, the fluid is only very weakly charged and, therefore, is not a plasma . Also, as a matter of fact, equations (2.14)-(2.16) correspond respectively to hypotheses H1, H3, and H9, which are formulated in section 1.2.4.

By virtue of these three assumptions, the electrical conductivity σ becomes independent of the electric charge density. In particular, the definition (2.9) of σ reduces to,

$$\sigma \;=\; \frac{e_0^2 z^2 D n_0}{K_{\mathrm{B}} T} \,, \tag{2.17}$$

where n_0 represents the total ionic concentration in the liquid, $n_0 = n_N + n_P$. Further, by introducing (2.10) and (2.11) into (2.12), we readily obtain the following expression for the total current density,

$$\boldsymbol{J} \;=\; -D\nabla\rho_{el} + \sigma\boldsymbol{E} + \rho_{el}\boldsymbol{u}\,. \tag{2.18}$$

It is worth noting that Saville [139] provided a similar formulation for the total current density by using the notion of ion mobility ω instead of the diffusion coefficient $\boldsymbol{D}$. More specifically, we have,

$$\omega K_B T \;=\; \boldsymbol{D}\,. \tag{2.19}$$

The expression (2.18) for the total current density can be directly substituted in (2.13). In other words, the assumptions (2.14)-(2.16) allow for the introduction of a single conservation equation for the electric charge density (global analysis) instead of the use of a conservation equation for each ionic species (local analysis) [139].

One crucial benefit stemming from this simplification is that it is no longer required to determine the rates of chemical reactions such as recombination and production of cations or anions. This feature is particularly essential in the case of liquid hydrocarbons because such reaction rates are not readily available for them. Also, as mentioned in section 1.2.3, in the electrification of these substances, the dominant ionized species are typically unknown impurities [61].

By employing the continuity equation (2.1), Gauss' law (2.5), and the expression (2.18) for $\boldsymbol{J}$, the conservation equation (or, equivalently, balance law) for the electric charge density reads,

$$\frac{\partial\rho_{el}}{\partial t} + \boldsymbol{u}\cdot\boldsymbol{\nabla}\rho_{el} \;=\; -\frac{\sigma}{\epsilon}\rho_{el} + \boldsymbol{E}\cdot\boldsymbol{\nabla}\sigma + \boldsymbol{\nabla}\cdot\left(D\boldsymbol{\nabla}\rho_{el}\right)\,. \tag{2.20}$$

The diffusion coefficient $\boldsymbol{D}$ relies on the temperature and the ion mobility, which in turn depends on the fluid density. Since both the temperature and the fluid density are constant, then $\boldsymbol{D}$ is taken to be constant too.

Furthermore, the electrical conductivity of a liquid dielectric is due to impurities only which carry ions. The concentration of the impurities is very small and cannot be known precisely. Nonetheless, it is reasonable to assume that it remains nearly constant in the flow domain and does not affect the physical properties of the liquid (temperature, density, viscosisty). This has been a common assumption in previous

studies on liquid dielectrics; see, for example, [61, 88] and references therein. Therefore, the total ionic concentration n_0 can also be approximated as constant. According to Touchard et al. [95], this is also inferred from the hypothesis (2.15) that the difference between anion and cation concentrations is much smaller than their sum n_0. Consequently, in view of (2.17), the electrical conductivity σ can be approximated to be constant as well. This approximation is also made by necessity due to the scarcity of data for σ at different concentrations of impurities in liquid dielectrics. Then, with these approximations, the final form of the charge balance law reads,

$$\frac{\partial \rho_{\mathrm{el}}}{\partial t} + \boldsymbol{u} \cdot \boldsymbol{\nabla} \rho_{\mathrm{el}} \;=\; -\frac{\sigma}{\epsilon} \rho_{\mathrm{el}} + D \nabla^2 \rho_{\mathrm{el}} \,. \tag{2.21}$$

The above expression consists in an advection-diffusion-reaction equation. The second term on the left-hand side of this equation describes convection of charge, *i.e.*, the convective currents. The first term on the right-hand side of (2.21) represents the conductive currents, hereinafter referred as to *ohmic resistance*, and acts as a counterweight to charge accumulation. Finally, the second term on the right-hand side expresses diffusion of charge.

2.2.3 Non-dimensionalization of the governing equations

Herein, we introduce the dimensionless groups associated to the governing equations, especially with regards to the conservation equation for the electric charge density.

Dimensionless momentum equations

The Reynolds number is defined as the ratio of inertial to viscous forces. More specifically, it is given by,

$$Re \;=\; \frac{U h}{\nu} \,, \tag{2.22}$$

where h and U denote the hydrodynamic length scale and velocity scale, respectively. Due to the presence of the volumetric electric force in (2.2), another dimensionless group appears. In this work, it is denoted by Lo and reads,

$$Lo \;=\; \frac{\rho U^2}{h \, \rho_{\mathrm{el},0} \, E_0} \;=\; \frac{\rho \epsilon U^2}{h^2 \, \rho_{\mathrm{el},0}^2} \,, \tag{2.23}$$

where $\rho_{\mathrm{el},0}$ and E_0 represent the reference values of the electric charge density and electric field, respectively. According to Gauss' law (2.5), these reference values are

related via $E_0 = \rho_{\mathrm{el},0} h/\epsilon$. Then, the dimensionless form of the momentum equations reads,

$$\frac{\partial \boldsymbol{u}}{\partial t} + (\boldsymbol{u}\cdot\nabla)\boldsymbol{u} \;=\; -\nabla p + \frac{1}{Re}\nabla^2\boldsymbol{u} + \frac{1}{Lo}\boldsymbol{F}_{\mathrm{el}}\,. \tag{2.24}$$

Please note that, for simplicity purposes, we use the same symbols for dimensional and dimensionless quantities. Further, based on the remarks from section 2.2.1 concerning the volumetric electric force, the dimensionless number Lo is most often exceedingly large. This feature is mainly due to the hypothesis formulated in (2.16), also known as the *weak charge-density assumption*. In particular, by introducing (2.8) and (2.17) into (2.16), we readily obtain the following inequality,

$$\rho_{\mathrm{el}} \;<<\; \frac{\sigma K_{\mathrm{B}} T}{e_0 D} \;\Rightarrow\; Lo \;>>\; \rho\epsilon\left(\frac{e_0\, D\, U}{\sigma K_{\mathrm{B}} T\, h}\right)^2 . \tag{2.25}$$

In the present work, the volumetric electric force has been evaluated to be several orders of magnitude smaller than the other terms in the momentum equation (2.21). In particular, the ratio Lo/Re can increase up to 10^5. Therefore, for the problem of interest, we infer that the electric charge density and its redistributions across the flow domain do not affect the fluid motion.

Dimensionless charge conservation equation

Due to the ohmic resistance (or, equivalently, the conductive currents) in (2.21), the behavior of the electric charge density ρ_{el} is quite different from that of a passively advected scalar (*e.g.*, the temperature). Notably, three different electric time scales emerge naturally from (2.21). They read,

$$\tau_{\mathrm{c}} \;=\; \frac{h}{U}\,,\quad \tau_{\mathrm{e}} \;=\; \frac{\epsilon}{\sigma}\,,\quad \tau_{\mathrm{D}} \;=\; \frac{h^2}{D}\,. \tag{2.26}$$

The first time scale τ_{c} is related to the convection of charge by the flow. The second time scale τ_{e} concerns the charge relaxation. Please note that τ_{e} does not exist in passively advected scalar and is specific to this equation. The third time scale τ_{D}, on the other hand, is related to the diffusion of charge. Further, we introduce two dimensionless quantities from (2.26), namely,

$$Re_{\mathrm{E}} \;=\; \frac{\tau_{\mathrm{e}}}{\tau_{\mathrm{c}}}\,,\quad Pe \;=\; \frac{\tau_{\mathrm{d}}}{\tau_{\mathrm{c}}}\,, \tag{2.27}$$

where Re_{E} and Pe denote, respectively, the electric Reynolds and Péclet numbers [141–143]. Consequently, the conservation equation for the electric charge density reads, in dimensionless form,

$$\frac{\partial \rho_{\mathrm{el}}}{\partial t} + \boldsymbol{u} \cdot \boldsymbol{\nabla} \rho_{\mathrm{el}} \;=\; -\frac{1}{Re_{\mathrm{E}}}\, \rho_{\mathrm{el}} + \frac{1}{Pe} \nabla^2 \rho_{\mathrm{el}}\,. \tag{2.28}$$

The presence of the ohmic resistance in (2.21) also leads to a different characteristic length scale than h: the Debye length. It is denoted by λ_{D}, and is defined by,

$$\lambda_{\mathrm{D}} \;=\; \sqrt{\frac{\epsilon D}{\sigma}}\,. \tag{2.29}$$

As mentioned in section 1.2.3, the Debye length is proportional to the square root of the electrical resistivity of the liquid. Then, this quantity becomes significant for dielectric liquids such as liquid hydrocarbons. Due to (2.29), it is possible to rewrite the equation (2.28) through the Debye length λ_{D} instead of the hydrodynamic length scale h. To this end, we introduce another dimensionless group: the Debye number Re_{λ}, given by,

$$Re_{\lambda} \;=\; \frac{h}{\lambda_{\mathrm{D}}}\,. \tag{2.30}$$

By definition, this quantity measures the importance of the Debye length over the hydrodynamic length scale. Subsequently, the charge conservation equation can also read, in dimensionless form,

$$\frac{\partial \rho_{\mathrm{el}}}{\partial t} + \boldsymbol{u} \cdot \boldsymbol{\nabla} \rho_{\mathrm{el}} \;=\; -\frac{Re_{\lambda}^2}{Pe}\, \rho_{\mathrm{el}} + \frac{Re_{\lambda}^2 Re_{\mathrm{E}}}{Pe^2}\, \nabla^2 \rho_{\mathrm{el}}\,. \tag{2.31}$$

In particular, we have the following relation between the Debye, Péclet and electric Reynolds numbers,

$$Re_{\lambda}^2 \;=\; \frac{Pe}{Re_{\mathrm{E}}}\,. \tag{2.32}$$

From (2.24) and (2.32), we readily infer that four dimensionless quantities control the phenomenon of flow electrification: the electric (Re_{E}) and hydrodynamic (Re) Reynolds numbers, the Péclet number (Pe), and the Debye number (Re_{λ}). Therefore, we investigate the influence of each in the following chapters. Nonetheless, before doing so, we present below the numerical modeling.

2.3 Numerical modeling

Throughout this thesis, we have used the computational framework of pafiX and contributed to its further development. As explained above, pafiX was designed by Grosshans [132] and implemented in the language F95. Further, it is parallelized via the Message Passing Interface protocol, also known as MPI. PafiX stands for *Particle Flow Simulation in Explosion Protection* and has been available as freeware since 2019. Initially, it was designed to study powder and fluid under conditions involving operational safety hazards. At the same time, it aims to be as simple and understandable as possible while being efficient. To this end, pafiX simplifies redundant features of classical academic code. For instance, the first version of pafiX had ten times fewer lines of code than the previous solver employed for the study of powder and fluid; see [144, 145]. PafiX includes, *inter alia*, a Navier-Stokes solver. For validation purposes, we performed [1] DNS of duct flows and compared them with previous DNS available in the literature [147, 148]. In what follows, we elaborate on the numerical procedure that we use to integrate the governing system of equations, starting with an outline of the Navier-Stokes solver and finishing with the framework of the electrostatics solver.

Obtaining numerical solutions requires the definition of a computational mesh to discretize the geometric domain. Herein, we employ the finite difference method. Accordingly, a set of indices, denoted by (i, j, k), uniquely identifies each grid node. It corresponds to the indices of the grid lines that intersect at it. Also, we define the neighbor nodes by increasing or reducing one of the indices by unity. Therefore, each node provides one algebraic (partial differential) equation. Then, we replace each term of the partial differential equation with a finite-difference approximation at each node. For clarity, Figure 2.1 illustrates an example of a computational grid point P and its neighborhood. Additionally, Table 2.1 defines the compass notation employed herein.

All unknown variables, however, are not necessarily stored at the same grid points. Herein, pafiX has been implemented in a staggered grid, introduced by Harlow and Welch [149]. The motivations behind that are multiple; see [150]. In particular, staggered grids are not prone to the well-known odd-even decoupling between the pressure and velocity fields [151, 152]. For example, Figure 2.2 provides a staggered grid ar-

[1] Grosshans H., Bissinger, C., Calero, M. and Papalexandris M., The effect of electrostatic charges on particle-laden duct flows, *J. Fluid Mech.* 909 (2021) A21. [146]

rangement in the xy-plane. As exhibited in this figure, we compute the variables p, $\boldsymbol{E}$, and ρ_{el} at the cell centers. By contrast, we evaluate the velocity field $\boldsymbol{u}$ and the volumetric electric force $\boldsymbol{F}_{\mathrm{el}} = (F_{\mathrm{x}}, F_{\mathrm{y}}, F_{\mathrm{z}})$ at the center of the cell faces.

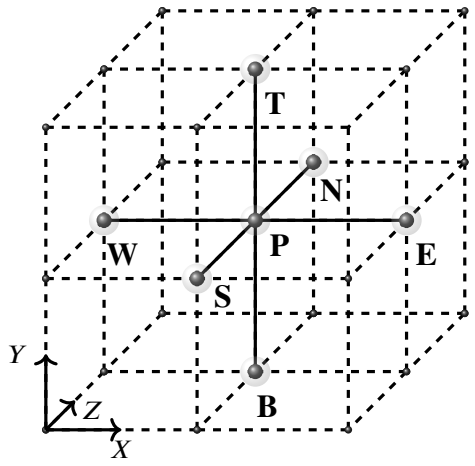

Figure 2.1: Representation of a computational grid point (P) and its neighborhood.

Furthermore, pafiX employs a non-uniform Cartesian grid, with refined grid meshing in the wall region, as is typically the case for simulating wall-bounded flows [150]. As a result, the discretization error is more evenly distributed over the computational domain, leading to a better numerical solution [150]. Also, the staggered grid requires interpolated values of the velocity field $\boldsymbol{u}$ to solve the charge conservation equation

Grid location	Compass notation
i, j, k	P
$i-1, j, k$	W
$i+1, j, k$	E
$i, j-1, k$	B
$i, j+1, k$	T
$i, j, k-1$	S
$i, j, k+1$	N

Table 2.1: Grid location and its compass notation

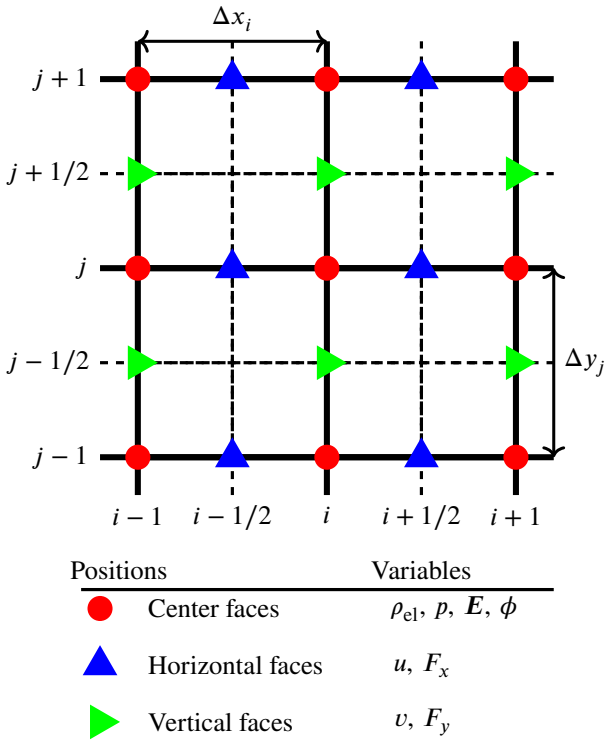

Figure 2.2: Staggered grid arrangement in the xy-plane.

(2.21). Herein, we employ the bilinear interpolation, regarded as the simplest two-dimensional interpolation [153]. For example, in (2.21), for a given computational grid point P, we have,

$$\tilde{u}_{\mathrm{P}} := \frac{1}{2}\left(u_{\mathrm{P}} + u_{\mathrm{W}}\right), \tag{2.33}$$

$$\tilde{v}_{\mathrm{P}} := \frac{1}{2}\left(v_{\mathrm{P}} + v_{\mathrm{B}}\right), \tag{2.34}$$

$$\tilde{w}_{\mathrm{P}} := \frac{1}{2}\left(w_{\mathrm{P}} + w_{\mathrm{S}}\right), \tag{2.35}$$

where $\tilde{u}_{\mathrm{P}}$, $\tilde{v}_{\mathrm{P}}$ and $\tilde{w}_{\mathrm{P}}$ denote the interpolated velocity components, with the compass notation from Table 2.1.

2.3.1 Hydrodynamics solver

In this section, we describe the hydrodynamics solver of pafiX, for which several improvements have been made in recent years; see the comparison between [146] and the procedure below. We note the following concerning the discretization of the spatial derivatives of the flow variables. The convective term, the pressure gradient, and the viscous terms of the momentum equations (2.2) are discretized through second-order central differences. In the case of a staggered grid, this second-order approximation is the most natural because we do not need to interpolate.

Since the dynamic pressure enters the momentum equations (2.2) via its gradient, its role is to constrain the fluid motion so that the continuity equation (2.1) is satisfied. Herein, we couple the continuity and momentum equations through a (sequential) Semi-Implicit Method for Pressure-Linked Equations, commonly known as SIMPLE [154]. This algorithm is widely employed in the field of Computational Fluid Dynamics (CFD) to solve the governing equations of fluid mechanics. Please note that other versions have been developed since then, such as SIMPLER [151], SIMPLEC [155] or the PISO algorithm [156]. Furthermore, we integrate in time the Navier-Stokes equations via second-order implicit scheme using a variable time step,

$$\frac{\partial \boldsymbol{u}}{\partial t} \approx \frac{\left(1+\tau^{n+\frac{1}{2}}\right)\boldsymbol{u}^{n+1} - \left(1+\tau^{n+\frac{1}{2}}+\tau^{n-\frac{1}{2}}\right)\boldsymbol{u}^{n} + \tau^{n-\frac{1}{2}}\boldsymbol{u}^{n-1}}{2\tau^{n+\frac{1}{2}}\,\Delta t^{n+1}}, \tag{2.36}$$

with

$$\tau^{n+\frac{1}{2}} = \frac{\Delta t^{n+1}}{\Delta t^{n+1}+\Delta t^{n}} \quad \text{and} \quad \tau^{n-\frac{1}{2}} = \frac{\Delta t^{n}}{\Delta t^{n}+\Delta t^{n-1}}\ , \tag{2.37}$$

where the superscript n represents a label for the current time instance, t^n, *i.e.*, the most advanced time at which the solution has been computed. Also, Δt^{n+1} corresponds to the time step used to advance the solution from the n-th time level to the next one.

2.3.2 Electrostatics solver

As discussed in section 2.1, we developed in pafiX an electrostatics solver aimed at solving the conservation equation for the electric charge density, which is strongly coupled with the Navier-Stokes equations via the convective term of (2.21). Accordingly, we describe below the main characteristics of the electrostatics solver.

We discretize the left-hand side of the Poisson equation (2.7) for the electric potential ϕ via second-order central differences. This discretization results in a linear system that standard linear solvers can solve. Herein, we apply the Jacobi method, which facilitates the straightforward parallelization of the computer code. The diffusive term of the charge conservation equation (2.21) is also discretized via second-order central differences.

Further, we apply an upwind scheme for the convective term of (2.21), coupled with a flux limiter. The motivations for adding a flux limiter are the following:

1. For smooth solutions, the flux limiter does not operate. The upwind scheme is second-order accurate, thus minimizing the numerical diffusion from a first-order upwind scheme.

2. In the case of discontinuities or sharp gradients, the flux limiter prevents the upwind scheme from introducing spurious oscillations due to the dispersive nature of second-order discretizations.

3. The upwind scheme and the flux limiter preserve the positivity of the numerical scheme. In other words, the sign of the electric charge density ρ_{el} remains the same everywhere in the liquid.

Several functions have been employed in the literature to estimate the flux limiter, denoted by Γ; see [157–163] and references therein. For this work, we use the (symmetric) minmod limiter function, introduced by Roe [160]. It reads,

$$\Gamma(r_+) = \max\left(0, \min\left(1, r_+\right)\right) , \tag{2.38}$$

where r_+ represents the ratio of successive gradients. By virtue of (2.38), the solution is smooth when $r_+ \geq 1$, thereby resulting in a second-order upwind scheme. Conversely, for sharp gradients, $\Gamma(r_+) = r_+ < 1$. Finally, in the case of discontinuities, the ratio of successive gradients is negative, thus $\Gamma(r_+) = 0$, resulting in a first-order upwind scheme. In order to better understand the role of the flux limiter, we provide below the approximation of $\dfrac{\partial \rho_{\text{el}}}{\partial y}$ at a given computational grid point $P(i, j, l)$.

We denote by $\mathfrak{U}_{\mathrm{P}}$ and $\mathfrak{U}_{\mathrm{B}}$ the first-order upwind scheme approximation (positive velocity) of $\dfrac{\partial \rho_{\mathrm{el}}}{\partial y}$ at the grid points $P(i,j,l)$ and $B(i,j-1,l)$, respectively. They read,

$$\mathfrak{U}_{\mathrm{P}} = \frac{\rho_{\mathrm{el}}(i,j,l) - \rho_{\mathrm{el}}(i,j-1,l)}{\Delta y_j}, \tag{2.39}$$

$$\mathfrak{U}_{\mathrm{B}} = \frac{\rho_{\mathrm{el}}(i,j-1,l) - \rho_{\mathrm{el}}(i,j-2,l)}{\Delta y_{j-1}}. \tag{2.40}$$

For a positive interpolated velocity $\tilde{v}_{\mathrm{P}}$, the approximation of $\dfrac{\partial \rho_{\mathrm{el}}}{\partial y}$ is given by,

$$\frac{\partial \rho_{\mathrm{el}}}{\partial y}(i,j,l) \approx \mathfrak{U}_{\mathrm{P}} - \Gamma(r_+)\frac{\Delta y_j}{\Delta y_j + \Delta y_{j-1}}\left(\mathfrak{U}_{\mathrm{B}} - \mathfrak{U}_{\mathrm{P}}\right). \tag{2.41}$$

On the basis of (2.41), we list below three different cases.

- Case 1: $\mathfrak{U}_{\mathrm{P}}$ and $\mathfrak{U}_{\mathrm{B}}$ have opposite signs.

  It corresponds to the case in which we have discontinuities. Thus, the ratio of successive gradients is negative and we have,

  $$\frac{\partial \rho_{\mathrm{el}}}{\partial y}(i,j,l) \approx \mathfrak{U}_{\mathrm{P}}. \tag{2.42}$$

- Case 2: $\mathfrak{U}_{\mathrm{P}}$ is negative and $\mathfrak{U}_{\mathrm{B}}$ is strictly negative.

  For this case, we set the ratio of successive gradients to be equal to,

  $$r_+ = \frac{\mathfrak{U}_{\mathrm{P}}}{\mathfrak{U}_{\mathrm{B}}}. \tag{2.43}$$

  In particular, the solution is smooth for $\mathfrak{U}_{\mathrm{P}} \geq \mathfrak{U}_{\mathrm{B}}$.

- Case 3: $\mathfrak{U}_{\mathrm{P}}$ is positive and $\mathfrak{U}_{\mathrm{B}}$ is strictly positive.

  This case bears similarities with the previous one, except that we inverse the ratio of successive gradients, namely,

  $$r_+ = \frac{\mathfrak{U}_{\mathrm{B}}}{\mathfrak{U}_{\mathrm{P}}}. \tag{2.44}$$

  Consequently, the solution is smooth when $\mathfrak{U}_{\mathrm{B}} \geq \mathfrak{U}_{\mathrm{P}}$.

To summarize, the final value of r_+ reads,

$$r_+ = \max\left(0, \frac{\min\left(0, \mathfrak{U}_\mathrm{P}\right)}{\mathfrak{U}_\mathrm{B}} + \frac{\max\left(0, \mathfrak{U}_\mathrm{B}\right)}{\mathfrak{U}_\mathrm{P}}\right). \tag{2.45}$$

Finally, the charge conservation equation (2.21) is integrated in time by an explicit second-order Runge-Kutta method. In what follows, we present the steps required to advance the solution from a time t^n to the next time step $t^{\mathrm{n}+1}$. As explained in section 2.3.2, the superscript n denotes a label for the current time instance.

1. The intermediate electric charge density ρ_el^* is calculated by using the interpolated value of $\boldsymbol{u}^\mathrm{n}$ and ρ_el^n,

$$\left(\delta\rho_\mathrm{el}\right)^\mathrm{n} = -\boldsymbol{u}^\mathrm{n}\cdot\boldsymbol{\nabla}\rho_\mathrm{el}^\mathrm{n} - \frac{\sigma}{\epsilon}\rho_\mathrm{el}^\mathrm{n} + D\nabla^2\rho_\mathrm{el}^\mathrm{n}, \tag{2.46}$$

$$\rho_\mathrm{el}^* = \rho_\mathrm{el}^\mathrm{n} + \frac{1}{2}\left(\delta\rho_\mathrm{el}\right)^\mathrm{n}\Delta t^\mathrm{n}. \tag{2.47}$$

2. The electric potential ϕ^* is computed by solving the Poisson equation (2.7), the right-hand side of which involves the value of ρ_el^* that was determined in Step 1.

3. The electric field $\boldsymbol{E}^*$ is evaluated from (2.6).

4. The value of the volumetric electric force F_el^* is updated from (2.4).

5. The new values of the velocity field $\boldsymbol{u}^{\mathrm{n}+1}$ and the pressure $p^{\mathrm{n}+1}$ are computed through the SIMPLE algorithm.

6. The new electric charge density $\rho_\mathrm{el}^{\mathrm{n}+1}$ is calculated via the interpolated value of $\boldsymbol{u}^{\mathrm{n}+1}$ and ρ_el^*,

$$\left(\delta\rho_\mathrm{el}\right)^* = -\boldsymbol{u}^{\mathrm{n}+1}\cdot\boldsymbol{\nabla}\rho_\mathrm{el}^* - \frac{\sigma}{\epsilon}\rho_\mathrm{el}^* + D\nabla^2\rho_\mathrm{el}^*, \tag{2.48}$$

$$\rho_\mathrm{el}^{\mathrm{n}+1} = \rho_\mathrm{el}^* + \frac{1}{2}\left(\delta\rho_\mathrm{el}\right)^*\Delta t^{\mathrm{n}+1}. \tag{2.49}$$

2.4 Computational setup

In this section, we provide the main information concerning the computational setup of all the numerical simulations conducted throughout this thesis. It includes the liquid employed alongside its material properties, the geometry of the flow domain, and the boundary conditions.

2.4.1 Properties of benzene

In the present study, we select benzene as the working medium. As mentioned in section 1.1.1, benzene is one of the most important hydrocarbons in the petrochemical industrial sector. Due to its low conductivity, benzene is ideal for studying flow electrification. Moreover, the value of the liquid conductivity, or equivalently the concentration of impurities inside the liquid, is large enough to have only ionic carriers, hence no free electrons. Indeed, according to Castellanos [143], there are no free electrons inside a given dielectric liquid if $\sigma > 10^{-14}$ S/m, corresponding to a high level of saturation on impurities. From Table 2.2, we readily infer that our value of σ meets the requirement. Therefore, the hypothesis of the absence of free electrons formulated in section 2.2.2 applies herein.

Please note that, although we study flow electrification of benzene, the findings of our simulations also apply to dielectric liquids in general. In particular, we investigate in Chapter 4 the influence of the electrical conductivity, the diffusion coefficient, and the Debye length on turbulent flow electrification. Accordingly, we list in Table 2.2 the material properties of benzene at 25°C, corresponding to a standard ambient temperature. Specific values have been measured experimentally, such as the mass density [164], the electrical permittivity [165], and the electrical conductivity of benzene [166]. The remaining quantities, on the other hand, have been determined empirically.

Reid et al. [7] provided a four-parameter exponential correlation for the dynamic viscosity $\mu = \nu\rho$, which reads,

$$\mu \;=\; A_1 \exp\left(\frac{A_2}{T} + A_3 T + A_4 T^2\right), \tag{2.50}$$

where A_1, A_2, A_3, and A_4 vary in terms of the liquid and the temperature; see, for example, [7]. Herein, we obtain approximately $\mu = 6.07 \times 10^{-4}$ Kg/ms, leading to a value of $\nu = 6.95 \times 10^{-7}$ m^2/s. Further, we employ the Einstein-Stokes law to compute the diffusion coefficient D. It reads,

$$D \;=\; \frac{K_\mathrm{B} T}{6\pi\mu r}, \tag{2.51}$$

where r denotes the ionic radius, set equal to $r = 2$ nm [167]. Thus, we obtain a value of $D = 1.80 \times 10^{-10}$ m^2/s. Finally, we estimate the Debye length from definition (2.29), which corresponds approximately to $\lambda_\mathrm{D} = 5.73 \times 10^{-5}$ m.

Symbol	Quantity	Value
ρ	Mass density [164]	8.74×10^2 Kg/m^3
ν	Kinematic viscosity [7]	6.95×10^{-7} m^2/s
ϵ	Electrical permittivity [165]	2.01×10^{-11} F/m
σ	Electrical conductivity [166]	1.10×10^{-12} S/m
D	Diffusion coefficient [167]	1.80×10^{-10} m^2/s
λ_D	Debye length	5.73×10^{-5} m

Table 2.2: Material properties of benzene at standard ambient temperature.

Please note that the measurement of the electrical conductivity (and, by extension, the Debye length) in dielectric liquids depends on the concentration of impurities, as mentioned in section 2.2.2. Therefore, the estimation obtained in Table 2.2 may be subject to discussion. However, these values are in good agreement with the data collected in the literature when measuring the Debye length of dielectric liquids. For example, Cabaleiro et al. [125] obtained a value of $\lambda_D = 3.95 \times 10^{-5}$ m for a 25° C mineral oil. Similarly, Touchard et al. [95] determined the Debye length of a liquid heptane at room temperature, corresponding to $\lambda_D = 7.95 \times 10^{-5}$ m.

2.4.2 Channel flow

In this thesis, we are concerned with flow electrification in channels. This choice of flow domain was motivated by the following factors. First, most results involving flow electrification are based on circular pipes. As suggested by Cabaleiro et al. [112], there is an increasing number of applications concerning flow electrification in channels. Hence, through this study, we aim to fill this gap. Second, channel flow is one of the simplest wall-bounded flows and plays a significant role in turbulent flow studies. Accordingly, many results concerning turbulence are readily available; see, for example, [168, 169] and references therein.

The computational domain consists of a periodic channel in the streamwise and spanwise directions, x and z, respectively. The half-width of the channel is denoted by h and set at $h = 0.5$ cm. As is typically the case in channel flow, we employ h as the hydrodynamic length scale. Also, the midplane of the channel is assumed to be

located at $y = 0$. The length of the channel is $4\pi h$ (streamwise direction x), its width is $2h$ (cross-stream direction y), and its depth is $2\pi h$ (spanwise direction z); see Figure 2.3. Further, the grid spacing is uniform in the x and z directions. In the y direction, the mesh is refined in the near-wall regions in a fashion similar to that of Kim et al. [170]. More specifically, the y coordinates of the edges of the computational cells are given by the general formula,

$$y_j \;=\; h\,\cos\left(\frac{j-1}{N_\mathrm{y}-1}\pi\right)\,, \qquad j = 1,\dots N_\mathrm{y}\,, \tag{2.52}$$

where N_y represents the total number of grid cells in the cross-stream direction.

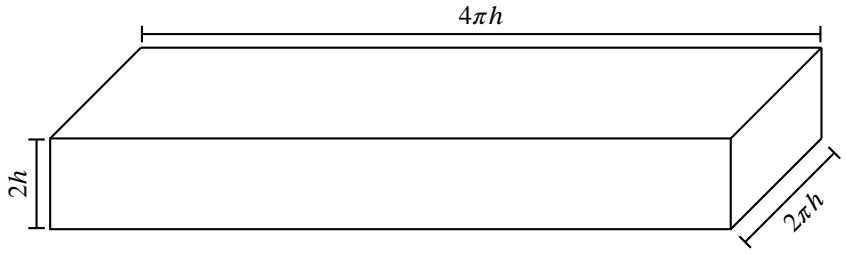

Figure 2.3: Schematic representation and dimensions of the flow domain.

2.4.3 Boundary conditions

In the streamwise x and spanwise z directions, periodic boundary conditions are applied for all the variables considered herein, namely, $\boldsymbol{u}$, p, ρ_el, ϕ, $\boldsymbol{E}$, and $\boldsymbol{F}_\mathrm{el}$. For this study, we prescribe at the solid-wall boundaries the no-slip condition for the velocity field, *i.e.*, all velocity components are zero. In addition, the solid-wall boundaries are located at the Stern layer. Hence, we note the following:

1. The Stern layer is not resolved numerically because its thickness is at the order of the ion size (nanometer).

2. Since the Stern layer represents the wall, we do not consider in this study the behavior of electrons and ions at the surface of the solid wall; see Figure 1.7 for visualization purposes.

3. The Stern layer is assumed to be unaffected by the flow and the liquid/solid interface. This is because significant electrostatic forces (*e.g.*, the adsorption force) between ions in the Stern layer and electrons in the surface charge prevent any transfer. The ions in the Stern layer are, in particular, incapable of diffusing in the surface charge nor inside the liquid, regardless of the turbulence intensity of the flow; see, for example, [46, 171, 172].

By virtue of the third point, equivalent to H4 in section 1.2.4, we prescribe a non-zero Dirichlet condition for the electric charge density ρ_{el} at the solid-wall boundaries. In other words, the electric charge density remains constant in the Stern layer. Further, the selection of this constant is determined such as it respects the weak charge-density assumption (2.16); *i.e.*,

$$\rho_{\mathrm{w}} \; < \; \frac{K_{\mathrm{B}} T \sigma}{e_0 D} \,, \tag{2.53}$$

where ρ_{w} represents the constant charge density at the wall. According to the parameters given in Table 2.2, the right-hand side of (2.53) equals 1.57×10^{-4} C/m^3. Therefore, for this study, the electric charge density at the wall (Stern layer) corresponds to $\rho_{\mathrm{w}} = 10^{-4}$ C/m^3. In particular, the Stern layer solely consists of cations, as illustrated in Figure 1.7. It is worth adding that this value is in good agreement with data from previous literature. For example, Paillat et al. [97] used a charge density at the wall ranging between 2.60 and 3.46 (10^{-4} C/m^3). More interestingly, Cabaleiro et al. [125] employed a value of 8.24×10^{-4} C/m^3 when the right-hand side of (2.53) was set to 3.15×10^{-4} C/m^3. Therefore, those authors did not consider the weak charge-density assumption.

Furthermore, the sign of the constant charge density at the wall does not restrict our study. This pattern is due to the configuration of the conservation equation for the electric charge density (2.21). More specifically, the governing equations for ρ_{el} and its opposite $-\rho_{\mathrm{el}}$ are identical. Similarly, the value of ρ_{w} does not influence the overall behavior ot the electric charge density. Indeed, by virtue of (2.21), the ratio $\rho_{\mathrm{el}}/\rho_{\mathrm{w}}$ is independent of the charge density at the wall. Please note that this property is valid as long as the volumetric electric force does not influence the fluid motion, which is the case in this work; see section 2.2.1.

Finally, we apply a zero-Neumann condition for the electric potential at the solid-wall boundaries. The use of $\boldsymbol{\nabla}\phi = \mathbf{0}$ implies that the overall charge (including the

liquid and the solid boundaries) remains zero. Alternatively, one could specify the value of the electric potential at the walls, *i.e.*, assign a Dirichlet boundary condition for ϕ. However, this value can seldom be estimated in a reliable manner. Further, numerical experiments conducted in the context of this study showed that the use of the Dirichlet boundary condition for the potential has negligible effects on the evolution of the charge-density distribution. Accordingly, by virtue of equations (2.6) and (2.4), both the electric field $\boldsymbol{E}$ and the volumetric electric force $\boldsymbol{F}_{\text{el}}$ equal zero at the solid-wall boundaries.

2.5 Concluding remarks

In this chapter, we introduced the governing equations for the motion of flow under study: the incompressible Navier-Stokes equations and the conservation equation for the electric charge density. Then, we presented the discretization methods used to solve the governing equations. In particular, we paid special attention to developing an accurate and robust algorithm for the resolution of the electric charge density. Finally, we elaborated on the computational setup employed for all simulations conducted throughout this thesis.

CHAPTER 3

Diffuse layer: properties and structure

3.1 Introduction

Flow electrification occurs in the presence of the EDL, composed of both the Stern and diffuse layers (*cf.* section 1.2.2). As mentioned in section 2.4.3, the Stern layer represents in our study the wall of the channel and is, therefore, not resolved numerically due to its negligible thickness (which is equal to a few ion-diameters). On the other hand, the thickness of the diffuse layer is not negligible. Hence, its properties and structure can be studied theoretically and/or numerically. Therefore, this chapter presents an in-depth study of the properties and structure of the diffuse layer. This study considers three flow regimes: liquid at rest, laminar, and turbulent flows. In this context, we introduce below several quantities related to the investigation of the charge-density profile in the diffuse layer.

First, we denote the thickness of the diffuse layer by γ. For this work, we demonstrate below (see section 3.2.3) that the thickness γ is thinner than the half-width h of the channel. In other words, in the cross-stream direction of the channel, the charge-density distribution is divided into two distinct regions: the diffuse layer and the rest of the channel, hereinafter referred to as the *bulk of the channel*. This feature has

A part of the results reported herein have been published in: Calero, M., Grosshans H., and Papalexandris M., A computational framework for electrification of liquid flows, *J. Loss Prevent. Proc.* 74 (2022) 104637. [173]

the advantage of allowing us to study the phenomenon of flow electrification in the diffuse layer, which corresponds to the aim of this chapter. At the same time, we can also investigate the transport of electric-charge carriers outside the diffuse layer, which corresponds to the aim of Chapter 4.

Further, Q and I denote, respectively, the total charge and the streaming current in the liquid. For a channel flow of dimensions $4\pi h \times 2h \times 2\pi h$, they read,

$$Q := 2\int_0^{4\pi h}\int_{-h}^{0}\int_0^{2\pi h} \rho_{\mathrm{el}}(x,y,z)\, dz\, dy\, dx\,, \tag{3.1}$$

$$I := \int_0^{4\pi h}\int_{-h}^{0}\int_0^{2\pi h} \frac{\rho_{\mathrm{el}}(x,y,z)\, u\,(x,y,z)}{h}\, dz\, dy\, dx\,, \tag{3.2}$$

where u corresponds to the streamwise velocity component. Q quantifies the total accumulation of electric-charge carriers, namely ions, in the liquid. On the other hand, the total streaming current I quantifies the convection (or, equivalently, advection) of ions by the flow parallel to the wall, which has been studied extensively in the literature, as reported in section 1.2.3. Similarly, we define the amount of charge and the streaming current in the diffuse layer by Q_{DL} and I_{DL}, respectively. They read,

$$Q_{\mathrm{DL}} := 2\int_0^{4\pi h}\int_{-h}^{-h+\gamma}\int_0^{2\pi h} \rho_{\mathrm{el}}(x,y,z)\, dz\, dy\, dx\,, \tag{3.3}$$

$$I_{\mathrm{DL}} := \int_0^{4\pi h}\int_{-h}^{-h+\gamma}\int_0^{2\pi h} \frac{\rho_{\mathrm{el}}(x,y,z)\, u\,(x,y,z)}{\gamma}\, dz\, dy\, dx\,. \tag{3.4}$$

From (3.1)-(3.2) and (3.3)-(3.4), two dimensionless numbers emerge naturally: Q/Q_{DL} and I/I_{DL}. These two ratios have a twofold purpose: first, Q/Q_{DL} helps determining an approximation for the thickness of the diffuse layer γ (*cf.* section 3.2.3). Additionally, these quantities provide insight into the significance of the diffuse layer with regards to flow electrification; see Chapter 4.

3.2 Diffuse layer in a liquid at rest

This section examines the properties of the diffuse layer when the liquid is at rest, *i.e.*, $\boldsymbol{u} = \boldsymbol{0}$. Then, the conservation equation for the electric charge density (2.21) reads in dimensional form,

$$\frac{\partial \rho_{\mathrm{el}}}{\partial t} = -\frac{\sigma}{\epsilon}\rho_{\mathrm{el}} + D\nabla^2\rho_{\mathrm{el}}\,. \tag{3.5}$$

3.2.1 Development of the diffuse layer via ionic diffusion

In the literature, certain authors (*e.g.*, López-Herrera et al. [130], Castellanos [137]) neglected the diffusive term due to relatively small values compared to the convective and conductive terms of (2.21). Accordingly, we highlight below the influence of this term on the diffuse-layer development. To this end, let us assume no diffusion of ions. In other words, the diffusion coefficient D is set equal to 0. Then, the electric charge density for a fluid at rest is given by,

$$\rho_{\mathrm{el}}(t) \;=\; \rho_{\mathrm{el}}^{0} \exp\left(-\frac{\sigma}{\epsilon} t\right) , \tag{3.6}$$

where ρ_{el}^{0} corresponds to the initial charge density in the liquid. According to this solution, the impurities in the liquid are not allowed to move. Instead, the initial charge density decays exponentially with time. In particular, the charge-relaxation time $\tau_{\mathrm{e}} = \epsilon/\sigma$, defined in (2.26), characterizes this decay. For aqueous solutions, the charge-relaxation time is very low. For example, $\tau_{\mathrm{e}} \approx 10^{-5}$ s for deionized water [130]. By contrast, for liquid hydrocarbons, the charge-relaxation time is significant. For instance, τ_{e} corresponds to $\tau_{\mathrm{e}} \approx 18$ s for benzene; see Table 2.2. Additionally, as can be seen from Figure 3.1, the phenomenon of charge relaxation is uniquely observable (in a human frametime) for dielectric liquids, such as benzene.

Further, from (3.6), we infer that the diffusive term controls the phenomenon of charge diffusion off the wall for a fluid at rest. More specifically, this term plays a major role in the development of the diffuse layer. By neglecting it, the electrical double layer would consist uniquely of the surface charge (solid) and the Stern layer (liquid), as suggested by Helmholtz [47]. This simple model has been proven to be inaccurate (*cf.* section 1.2.2). Moreover, through Helmholtz's model, the phenomenon of flow electrification cannot be explained since, in the liquid, there are no charges to transport. Therefore, it is fundamental to consider in this thesis the process of charge diffusion, although the diffusive term is several orders of magnitude smaller than both the convective and conductive terms of (2.21).

3.2.2 Charge-density distribution in a liquid at rest

By virtue of equation (3.5) and the boundary condition $\rho_{\mathrm{el}} = \rho_{\mathrm{w}}$ (see section 2.4.3), we derive a unique analytical (closed-form) solution for the electric charge density,

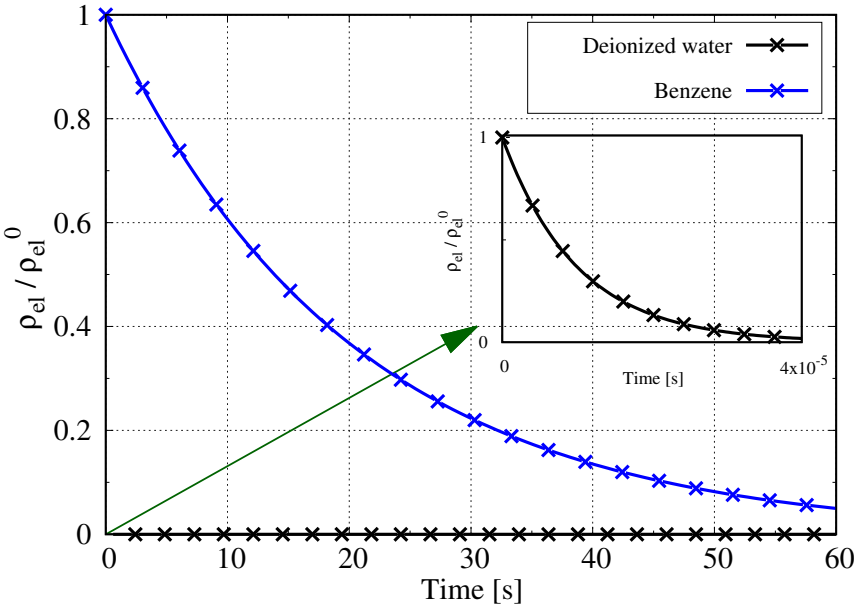

Figure 3.1: Comparison of the phenomenon of charge relaxation between a dielectric liquid (benzene) and an aqueous solution (deionized water).

denoted as $\overline{\rho}_{\mathrm{el}}$. In the case of a channel, periodic in the streamwise x and spanwise z directions (see section 2.4.2), this solution reads,

$$\overline{\rho}_{\mathrm{el}}(y) = \rho_{\mathrm{w}} \frac{\sinh\left(\frac{h-y}{\lambda_{\mathrm{D}}}\right) + \sinh\left(\frac{h+y}{\lambda_{\mathrm{D}}}\right)}{\sinh\left(\frac{2h}{\lambda_{\mathrm{D}}}\right)}, \quad \text{for} \quad y \in [-h, h]. \tag{3.7}$$

According to the above expression (3.7), the electric charge density $\overline{\rho}_{\mathrm{el}}$ has the following properties.

1. In contrast to (3.6), the electric charge density is time-independent but does vary in terms of the cross-stream direction y. Thus, based on the expression (3.7), ions are diffused away from the Stern layer. Moreover, this diffusion depends on four parameters: the Debye length λ_{D}, the electric charge density at the wall ρ_{w}, the half-width of the channel h, and the distance from the wall.

2. The electric charge density is symmetric in the cross-stream direction, *i.e.*, $\overline{\rho}_{\mathrm{el}}(y) = \overline{\rho}_{\mathrm{el}}(-y)$. We attribute this feature to the fact that we consider the same constant charge density at the top and bottom walls. This assumption has the advantage of simplifying the evaluation of integrals, such as for the total charge Q and the streaming current I, defined in equations (3.1) and (3.2), respectively.

3. The solution reaches its maximum at the walls ($y = \pm h$) and its minimum at the midplane ($y = 0$). Further, these extrema are respectively equal to,

$$\overline{\rho}_{\mathrm{el}}(\pm h) \;=\; \rho_{\mathrm{w}} \quad \text{and} \quad \overline{\rho}_{\mathrm{el}}(0) \;=\; \frac{\rho_{\mathrm{w}}}{\cosh\left(h/\lambda_{\mathrm{D}}\right)}\,. \tag{3.8}$$

   On the basis of (3.8), we deduce that the electric charge density at the wall acts as an upper limit for the electric charge density in the liquid and must satisfy the inequality (2.25) for the weak charge-density assumption to hold, as discussed in section 2.4.3. In addition, for high values of the Debye number, defined as $Re_{\lambda} = h/\lambda_{\mathrm{D}}$ (*cf.* (2.30)), the electric charge density at the midplane is negligible. In other words, the process of charge diffusion is restricted to a specific zone inside the liquid and close to the wall. By definition, this zone corresponds to the diffuse layer.

4. Due to symmetry, the solution is increasing for positive values of y and decreasing for negative values of y. More specifically, the electric charge density decreases in terms of the distance from the wall (or, equivalently, from the Stern layer). It is worth noting that this property is consistent with the formal definition of the diffuse layer; see [46] and references therein.

5. At high values of the Debye number, namely $Re_{\lambda} >> 4$, the solution (3.7) can be approximated by,

$$\overline{\rho}_{\mathrm{el}}(y) \;=\; \rho_{\mathrm{w}}\exp\left(-\frac{h-|y|}{\lambda_{\mathrm{D}}}\right), \quad \text{for} \quad y \in [-h, h]\,. \tag{3.9}$$

As mentioned above, the solution obtained in (3.7) is time-independent. In this case, the diffuse layer is said to be *fully developed*, as mentioned in section 1.2.4. In particular, it is assumed that physico-chemical phenomena no longer take place at the interface because a chemical equilibrium has been reached; see, for example, [95, 98].

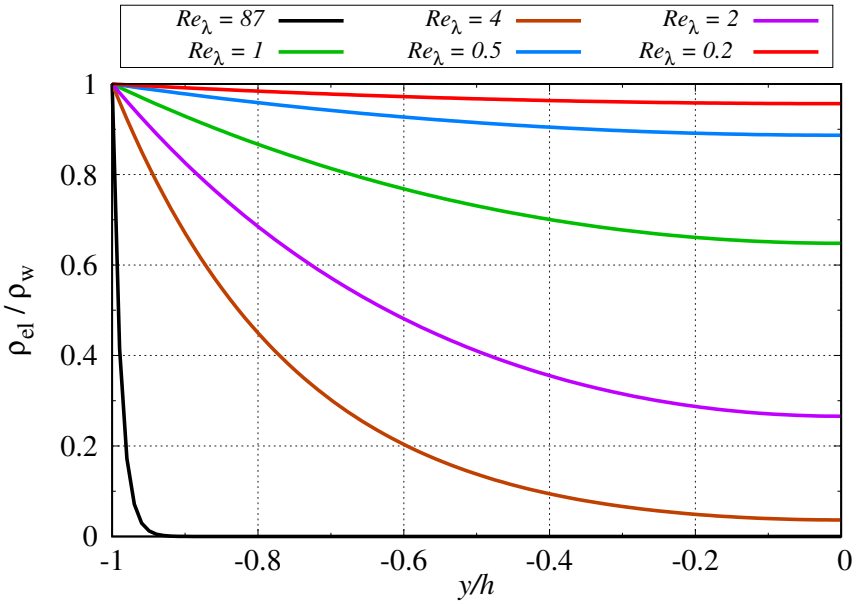

Figure 3.2: Charge-density distribution for a liquid at rest in a channel at various Re_λ, when the diffuse layer is fully developed.

This configuration is the starting point of our numerical study of flow electrification. Notably, all the numerical simulations conducted throughout this thesis employ the expression obtained in (3.7) as the initial profile for the electric charge density.

Further, we have plotted in Figure 3.2 the charge-density distribution for a liquid at rest in a channel (when the diffuse layer is fully developed), at various Re_λ. Due to symmetry, we provide only the profile for negative values of y. From these plots, we readily confirm that the electric charge density in the liquid decreases strongly with respect to Re_λ. More specifically, for very low values of Re_λ, the electric charge density tends to be uniform and equal to ρ_w. The explanation is the following. When the dimension of the channel is very small, as is the case in microfluidics, the Stern layer extends over a significant part of the channel. Hence, the value of the electric charge density in the liquid is close to that at the wall (Stern layer). Conversely, for large values of the Debye number, the diffuse layer is relatively thin compared to the half-width of the channel.

3.2.3 Thickness of the diffuse layer

In what follows, we investigate the thickness of the diffuse layer γ. The main purpose is to obtain a relation between γ and the Debye length λ_{D}, which is typically employed as the characteristic length scale of the EDL (*cf.* section 1.2.3). The analysis consists of two steps. First, we compute the total charge in the liquid Q and in the diffuse layer Q_{DL} with the solution obtained in (3.7). Then, we determine γ so that the ratio Q_{DL}/Q is sufficiently close to 1. By virtue of (3.1), (3.3), and the solution (3.7), we have,

$$\begin{aligned} Q &= 16(\pi h)^2 \lambda_{\mathrm{D}} \rho_{\mathrm{w}} \tanh(h/\lambda_{\mathrm{D}}), \\ Q_{\mathrm{DL}} &= 16(\pi h)^2 \lambda_{\mathrm{D}} \rho_{\mathrm{w}} \frac{\sinh(h/\lambda_{\mathrm{D}}) + \sinh((-h+\gamma)/\lambda_{\mathrm{D}})}{\cosh(h/\lambda_{\mathrm{D}})}. \end{aligned} \tag{3.10}$$

Then, the ratio Q_{DL}/Q equals,

$$\frac{Q_{DL}}{Q} = 1 - \frac{\sinh\left(\dfrac{h-\gamma}{\lambda_{\mathrm{D}}}\right)}{\sinh\left(\dfrac{h}{\lambda_{\mathrm{D}}}\right)}. \tag{3.11}$$

From (3.11), we deduce that the ratio Q_{DL}/Q depends on two quantities: the Debye number and the ratio between the thickness of the diffuse layer and the Debye length. Accordingly, we have plotted in Figure 3.3 four profiles of Q_{DL}/Q in terms of Re_λ. These profiles correspond to cases for which the thickness of the diffuse layer equals one, two, three, and four times the Debye length λ_{D}, respectively. According to it, for high values of the Debye number, γ can be approximated by $\gamma \approx 4\lambda_{\mathrm{D}}$ with an error of 1.8%; see Figure 3.3d. We assume it is sufficiently close to zero for the purposes of this study. As a result, we consider herein that the thickness of the diffuse layer corresponds to four times the Debye length.

Further, Paillat et al. [106] suggested that 87% (respectively, 95%) of the charge in the diffuse layer is located between the Stern layer and two times the Debye length (respectively, three times). Figures 3.3b and 3.3c indicate that these values are in excellent agreement. However, the statement made by Paillat et al. [106] holds solely for relatively high Debye numbers, *i.e.*, $Re_\lambda \geq 6$. By contrast, for $4 < Re_\lambda < 6$, the corresponding adequate thickness is determined by referring to Figure 3.3. Please note that this situation does not correspond to our problem in hand since $Re_\lambda \approx 87$; see Table 2.2. For visualization purposes, this case corresponds to the black line in Figure 3.2.

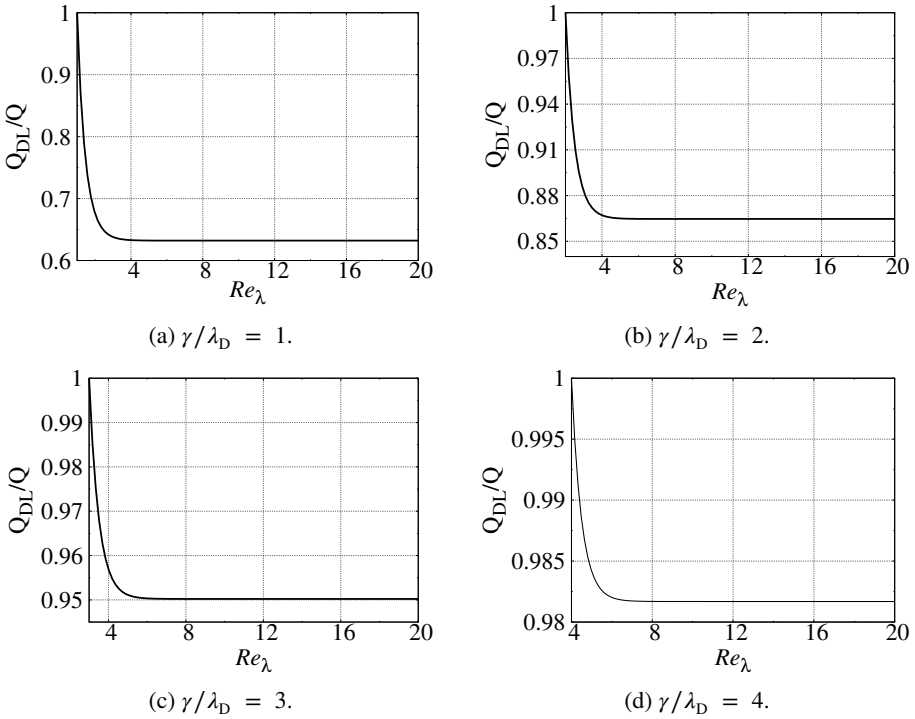

(a) $\gamma/\lambda_D = 1$. (b) $\gamma/\lambda_D = 2$.

(c) $\gamma/\lambda_D = 3$. (d) $\gamma/\lambda_D = 4$.

Figure 3.3: Variation of the ratio Q_{DL}/Q in terms of the Debye number Re_λ.

3.3 Charge-density distribution in laminar channel flow

In this section, we investigate the influence that laminar channel flow has on the charge-density distribution in the diffuse layer. Hence, we consider a liquid (benzene) in motion, in contrast to section 3.2. In this context, only the streamwise velocity u is non-zero. It reads [168],

$$u(y) = \frac{3u_m\left(h^2 - y^2\right)}{2h^2}, \quad \text{for} \quad y \in [-h, h], \tag{3.12}$$

where u_m represents the mean velocity, while ν denotes the kinematic viscosity, the value of which is provided in Table 2.2. It is worth adding that the expression (3.12) for the velocity field in Poiseuille flow is well known and is valid herein since the volumetric electric force in the momentum equations is assumed to be negligible, as mentioned in section 2.2.3 through the inequality (2.25).

According to (3.12), the velocity field is normal to the initial charge-density gradient of (3.7). This, in turn, implies that the convective term $\boldsymbol{u} \cdot \boldsymbol{\nabla} \rho_{\mathrm{el}}$ of (2.21) equals zero. Therefore, the charge-density profile is the same as for a fluid at rest, given by (3.7). More specifically, laminar flow electrification does not occur in channels in the sense that the liquid motion does not result in transport of electric-charge carriers away from the diffuse layer. Please note that is is also the case in circular pipes, as indicated by Touchard [92]. Nonetheless, the flowing liquid generates a streaming current (*cf.* section 1.2.3). It reads,

$$I \;=\; 8\pi^2 h \int_{-h}^{0} \overline{\rho}_{\mathrm{el}}(y)\, u\,(y)\, d\, y\,, \tag{3.13}$$

where $\overline{\rho}_{\mathrm{el}}$ corresponds to the time-asymptotic solution (3.7). Due to (3.7) and (3.12), the streaming current in laminar channel flow reads,

$$I \;=\; 24\pi^2 \rho_{\mathrm{w}} \lambda_{\mathrm{D}}^2 u_m \left(1 - \frac{\lambda_{\mathrm{D}}}{h} \tanh(h/\lambda_{\mathrm{D}}) \right) . \tag{3.14}$$

By virtue of the aforementioned expression, the streaming current in laminar channel flow depends on four parameters: the charge density at the wall ρ_{w}, the Debye length λ_{D}, the half-width of the channel h, and the mean velocity u_{m}. More specifically, we have the following properties.

1. The streaming current depends linearly on the mean velocity. This property is in excellent agreement with experimental measurements of the streaming current in both laminar pipe and rectangular channel flows; see [92, 96, 101, 106, 111], and references therein.

2. The streaming current is proportional to the constant charge density at the wall. This result stems from the specific relation between ρ_{el} and ρ_{w}. From (2.21), we infer that the ratio $\rho_{\mathrm{el}}/\rho_{\mathrm{w}}$ is independent of the value of the electric charge density at the wall, as discussed in section 2.4.3.

3. For high values of the Debye number, *i.e.*, $Re_\lambda >> 4$, the streaming current can be approximated by,

   $$I \;=\; 24\pi^2 \rho_{\mathrm{w}} \lambda_{\mathrm{D}}^2 u_m\,. \tag{3.15}$$

   Based on (3.15), the streaming current has a quadratic growth with regards to the Debye length. Thus, the streaming current has higher values when the liquid conductivity is low, as is the case in liquid hydrocarbons such as benzene.

As examined in section 1.2.4, the value of the electric charge density at the wall ρ_{w} depends on the initial concentration of impurities in the liquid. In particular, for lower values of σ, we expect a decrease of ρ_{w} (*cf.* (2.17)). From the two last points described above, it is not straightforward to determine with precision how different concentration of impurities influence the streaming current. Nonetheless, due to the relation between the Debye length and the diffuse layer, increasing the concentration of impurities (hence the electrical conductivity) results in a thinner diffuse layer.

Further, from (3.15), we infer that the streaming current in laminar channel flow cannot exceed a certain value, denoted by I_{max}. We estimate I_{max} via the expression (3.15), the weak-charge density assumption (2.53), and the inequality concerning the mean Reynolds number Re_{m} in a laminar regime [168],

$$Re_{\mathrm{m}} := \frac{2u_{\mathrm{m}}h}{\nu} \leq 1.35 \times 10^{3} \,. \tag{3.16}$$

Then, we have the following inequality for the streaming current in laminar channel flow,

$$I < I_{\mathrm{max}} := \frac{1.62 \times 10^{4} \pi^{2} \nu K_{\mathrm{B}} T \epsilon}{e_0 \, h} \,. \tag{3.17}$$

In our specific case of benzene flowing within a channel of dimensions $4\pi h \times 2h \times 2\pi h$, the maximum value for the streaming current corresponds to $I_{\mathrm{max}} = 1.14 \times 10^{-11} A$.

3.4 Perturbations of the charge-density distribution

In turbulent channel flows, the convective term $\boldsymbol{u} \cdot \boldsymbol{\nabla} \rho_{\mathrm{el}}$ of (2.21) has a nonzero value, in contrast to a fluid at rest (or in a laminar regime). The existence of this term implies that the solution (3.7) is no longer valid in turbulent channel flows. For this very reason, as reported in section 1.2.4, it has been proposed by several authors that flow turbulence plays a significant role in the phenomenon of flow electrification. Accordingly, we present in this section a numerical study of the perturbations of the charge-density distribution in the diffuse layer by turbulence. To this end, we describe below the grid resolution requirements.

3.4.1 Grid resolution requirements

For this study, we employ the friction Reynolds number $Re_\tau = u_\tau h/\nu$ to measure the turbulence intensity of the flow field. The friction velocity u_τ is defined by [168],

$$u_\tau = \sqrt{\frac{\tau_\mathrm{w}}{\rho}} \text{ and } \tau_\mathrm{w} = \mu \frac{\mathrm{d}\langle u \rangle_\mathrm{t}}{\mathrm{d}y}\Big|_{\tilde{y}=0}, \tag{3.18}$$

where τ_w denotes the wall shear stress. Further, $\langle u \rangle_\mathrm{t}$ stands for the time-averaged streamwise velocity, while $\tilde{y}$ represents the distance from the wall. Also, it is well-known that other relevant Reynolds numbers exist, such as the centerline and mean Reynolds numbers. Their differences stem from the selection of the hydrodynamic velocity scale. Nonetheless, for turbulent channel flows, semi-empirical correlations have been provided between the various Reynolds numbers [168]. Therefore, the particular choice of the Reynolds number is not restrictive.

In this section, we carry out six DNS for friction Reynolds numbers set equal to $Re_\tau = 80$, 100, 120, 150, 180, and 210. DNS is the most accurate approach for the numerical treatment of turbulent flows. For this reason, they are widely employed for the simulations of flows at low to moderate Reynolds numbers, as is the case herein. DNS, on the other hand, requires very fine grids. In particular, to perform DNS, we must meet two basic criteria [150]. First, the largest turbulence scales need to be included in the computational domain (a channel in our study). Additionally, the extent of the domain in the periodic directions has to be large so as to avoid spurious interactions between the largest structures. In other words, this approach requires to have a relatively large computational domain, as the one used in our study, namely $4\pi h \times 2h \times 2\pi h$ (*cf.* section 2.4.2). The second criterion concerns the grid resolution. It must be fine enough to capture the smallest turbulence structures, represented through the Kolmogorov microscale, η, defined by,

$$\eta = \left(\frac{\nu^3}{\mathscr{E}}\right)^{1/4}, \tag{3.19}$$

where $\mathscr{E}$ denotes the average rate of dissipation of the turbulent kinetic energy, the definition of which is given in section 4.3.2. In addition, based on the work of Kim et al. [170], we provide below a sufficient requirement for DNS of turbulent channel flows:

- In the periodic directions, the streamwise and spanwise grid spacing must satisfy,

$$\Delta x \;\leq\; 12\,\frac{h}{Re_\tau} \;\text{ and }\; \Delta z \;\leq\; 7\,\frac{h}{Re_\tau}\,. \tag{3.20}$$

- In the cross-stream direction, the relative distances between the wall and the third grid point (Δy_3), and between the wall and the tenth grid point (Δy_{10}) must follow,

$$\Delta y_3 \;\leq\; \frac{h}{Re_\tau} \;\text{ and }\; \Delta y_{10} \;\leq\; 10\,\frac{h}{Re_\tau}\,. \tag{3.21}$$

- In the cross-stream direction, the largest grid spacing ($\Delta y_{\max}$), located at the midplane $y = 0$ (see section 2.4.2), must satisfy,

$$\Delta y_{\max} \;\leq\; 10\,\frac{h}{Re_\tau}\,. \tag{3.22}$$

In the field of computational fluid dynamics (CFD), it is common practice to measure a distance via the wall unit y^+. This dimensionless quantity determines the relative importance of viscous and turbulent processes. In particular, the distance Δ of a generic quantity can be measured in wall units by,

$$\Delta^+ \;=\; \Delta\frac{Re_\tau}{h}\,. \tag{3.23}$$

Further, the computational mesh consists of $192\times129\times160$ grid cells for $Re_\tau \leq 180$. For $Re_\tau = 210$, we employ a finer grid consisting of $280\times181\times225$ grid cells. For the sake of completeness, Table 3.1 reports the values of the grid spacing in the x, y, and z directions for the DNS considered in this study. According to it, we readily conclude that the above requirements (3.20)-(3.22) for DNS have been satisfied. Additionally, Figure 3.4 presents an *a posteriori* comparison between the Kolmogorov length scale η^+ and the grid spacing Δy^+ in terms of the distance from the wall, measured in wall units. For $Re_\tau \leq 120$, the Kolmogorov length scale is always larger than the grid spacing; see Figure 3.4(c). Otherwise, the curve of η^+ is above the one of Δy^+ only close to the wall. As expected from Table 3.1, the biggest gap between Δy^+ and η^+ corresponds to the case $Re_\tau = 180$; see Figure 3.4(e). In particular, the grid spacing is one wall unit larger than the Kolmogorov length scale at $y = \pm0.5$. As a result, the grid employed for the case $Re_\tau = 180$ may be formally too coarse for DNS. However,

Re_τ	Δx^+	Δz^+	Δy_3^+	Δy_{10}^+	$\Delta y_{\max}^+$
80	5.23	3.13	0.46	2.37	3.86
100	6.54	3.92	0.58	2.95	4.83
120	7.85	4.70	0.69	3.56	5.79
150	9.81	5.88	0.87	4.45	7.24
180	11.77	7.05	1.04	5.33	8.69
210	9.4	5.84	0.30	3.17	3.64

Table 3.1: Summary of the grid spacing for the DNS considered herein.

as demonstrated by Kim et al. [170], the turbulent structures that are not resolved carry an insignificant amount of kinetic energy.

Initially, we perform a preliminary simulation of turbulent channel flow in absence of electric charge. Once the flow becomes fully developed, we apply the initial profile for the electric charge density (see Figure 3.5) and start solving for the coupled system of equations of electrohydrodynamics. Further, the initial profile has been computed numerically from the charge conservation equation for a liquid at rest. According to Figure 3.5, our numerical solution is in excellent agreement with the closed-form expression obtained in (3.7). Additionally, this figure allows us to identify the position of each numerical grid point in the diffuse layer. In the cross-stream direction, the coarser mesh (for $Re_\tau \leq 180$) consists of thirteen grid points within the diffuse layer, corresponding to approximately 20% of the total grid points in this direction. The last point is located at $y/h = -0.954$ so that the diffuse layer thickness γ is set equal to $4\lambda_{\mathrm{D}}$. In particular, as described in section 3.2.3, 98.2% of the total charge is concentrated in this zone. Finally, we determine for all simulations considered herein the time step via the Courant-Friedrich-Levy (CFL) condition with a constant Courant number set to 0.25.

3.4.2 The law of the wall in turbulent channel flows

Before proceeding further, we present in this section some general characteristics of turbulence in channel flow, which are deemed needed for the understanding of turbulent flow electrification. Accordingly, we employ certain well-known definitions

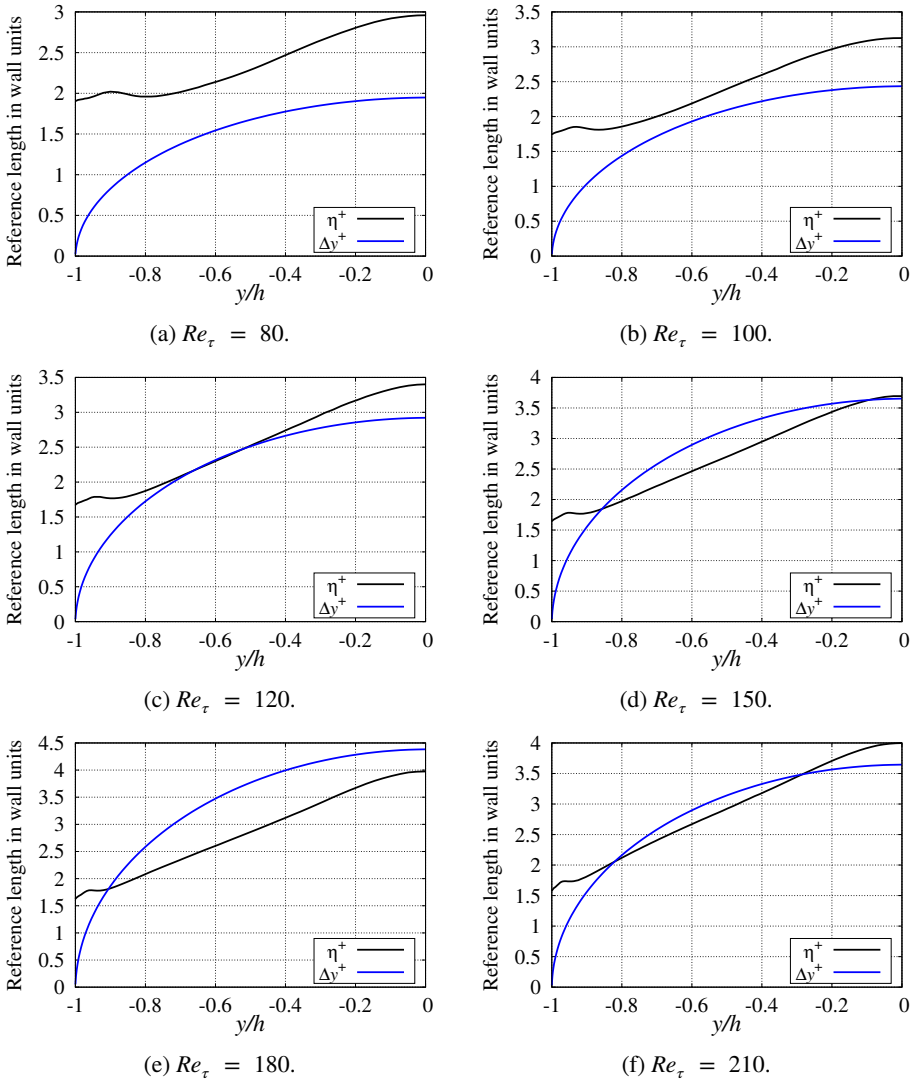

(a) $Re_\tau = 80$. (b) $Re_\tau = 100$.

(c) $Re_\tau = 120$. (d) $Re_\tau = 150$.

(e) $Re_\tau = 180$. (f) $Re_\tau = 210$.

Figure 3.4: Comparison of the Kolmogorov microscale η^+ and the grid spacing Δy^+, measured in wall units, for friction Reynolds number Re_τ ranging from 80 to 210.

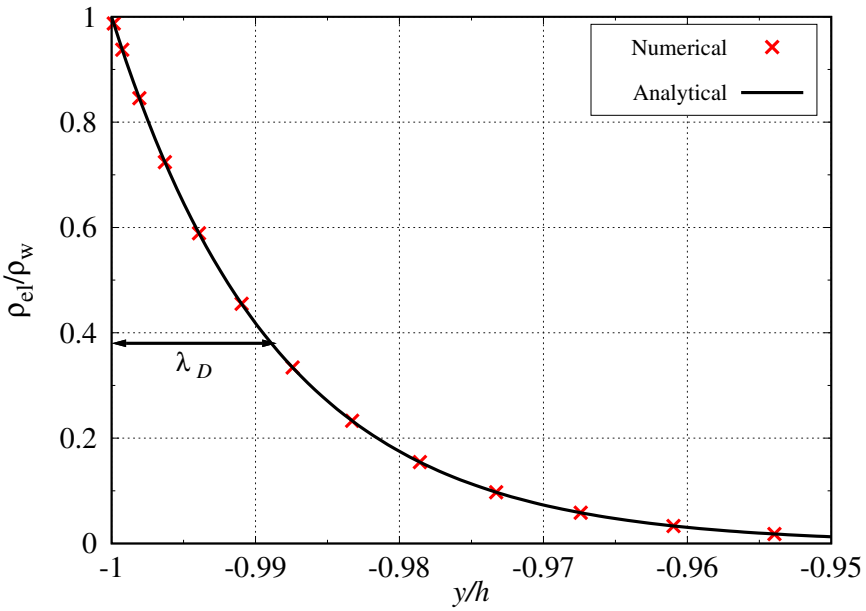

Figure 3.5: Analytical and numerical solutions of the charge-density distribution for a liquid at rest in the diffuse layer. It corresponds to the initial profile of the electric charge density for all the numerical simulations considered herein.

and notions regarding channel flows that can be found in standard textbooks; see, for example, [168, 169].

In turbulent flows, we can separate a generic quantity ψ into two parts: its mean $\langle\psi\rangle$ and its fluctuation ψ',

$$\psi = \langle\psi\rangle + \psi' . \tag{3.24}$$

A fully developed channel flow is considered statistically one-dimensional, with velocity statistics depending only on the cross-stream direction y,

$$\langle \boldsymbol{u} \rangle = (\langle u \rangle(y), 0, 0) . \tag{3.25}$$

The behavior of the velocity field strongly depends on the position regarding the distance from the wall. As described in section 3.4.1, we measure this distance via the wall unit y^+, defined by [168],

$$y^+ = \frac{(h-y)Re_\tau}{h}, \quad \text{for} \quad y \in [-h, h] . \tag{3.26}$$

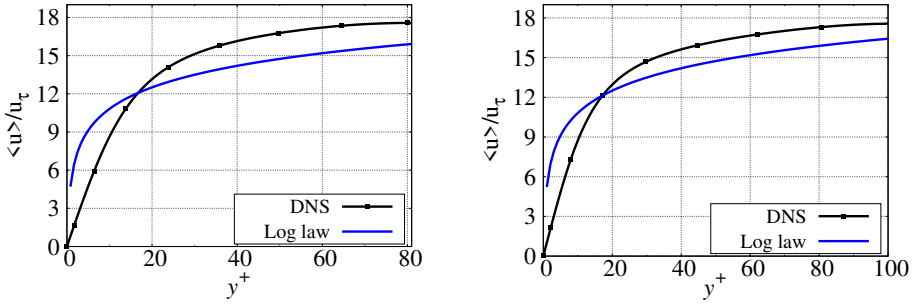

(a) $Re_\tau = 80$.

(b) $Re_\tau = 100$.

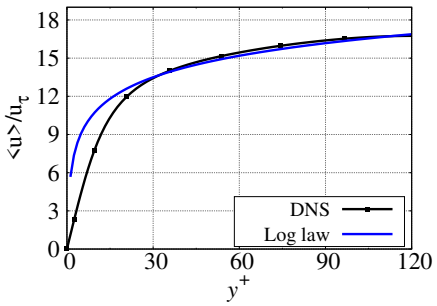

(c) $Re_\tau = 120$.

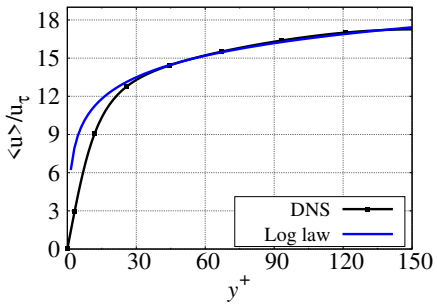

(d) $Re_\tau = 150$.

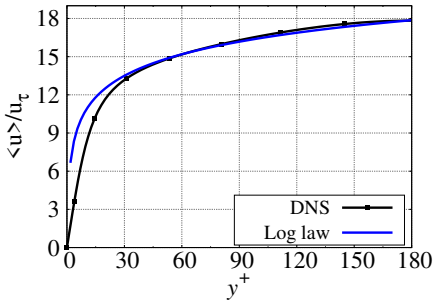

(e) $Re_\tau = 180$.

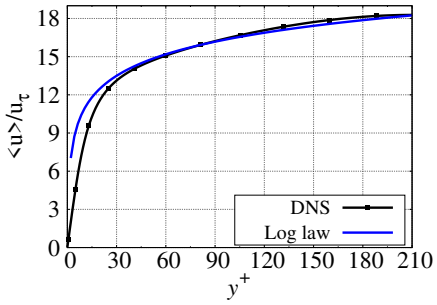

(f) $Re_\tau = 210$.

Figure 3.6: Comparison of the mean charge-density profiles with the log-law estimation for the DNS considered herein.

Typically, the channel is divided into two main zones: the *viscous wall region* corresponding to $y^+ < 50$ and the *outer layer* corresponding to $y^+ > 50$. This separation is of particular importance since we consider a flow to be laminar if $Re_\tau \leq 45$ [168]. In other words, in laminar channel flows, the fluid is restricted to the viscous wall region. Inside it, there is a zone called *viscous or laminar sublayer*, corresponding to $y^+ < 5$, in which the turbulent fluctuations are exceedingly small due to the proximity of this region with regards to the wall. In particular, the mean streamwise velocity consists of a linear profile regarding the wall unit [168],

$$\langle u^+ \rangle = y^+ \quad \text{for} \quad y^+ < 5\,. \tag{3.27}$$

Inside the outer layer, and more specifically in the *log-law region*, corresponding to $y^+ < 30$, the mean streamwise velocity is approximated via the following log law [168],

$$\langle u^+ \rangle = \frac{1}{0.41} \ln\left(y^+\right) + 5.2\,. \tag{3.28}$$

From the plots of Figure 3.6, we can confirm that our profiles of $\langle u \rangle$ agree very well with the log-law estimation (3.28). The only exceptions concern cases $Re_\tau = 80$ and $Re_\tau = 100$. Indeed, Patel and Head [174] observed transitional laminar/turbulent effects between $Re_\tau = 50$ and $Re_\tau = 100$. Therefore, conducting DNS at $Re_\tau = 80$ and $Re_\tau = 100$ allows the investigation of the phenomenon of flow electrification in transitional flows.

In this work, the viscous sublayer entirely covers the diffuse layer for $Re_\tau \leq 110$. By contrast, it covers approximately half of the diffuse layer for $Re_\tau = 210$. Accordingly, it is expected that the contribution of the velocity in the diffuse layer via the convective term $\boldsymbol{u} \cdot \boldsymbol{\nabla} \rho_{\text{el}}$ may not be as significant as in the bulk of the channel, or may even be negligible. We address this particular issue in the following section.

3.4.3 Evolution of the electric charge density

The fully developed diffuse layer is perturbed as soon as the flow becomes turbulent. Accordingly, we present in Figure 3.7 the evolution of the charge-density distribution in the diffuse layer for the Reynolds numbers considered herein. From Figure 3.7, we observe certain similarities between the different plots, regardless of Re_τ. First, the electric charge density in the diffuse layer tends progressively towards an equilibrium

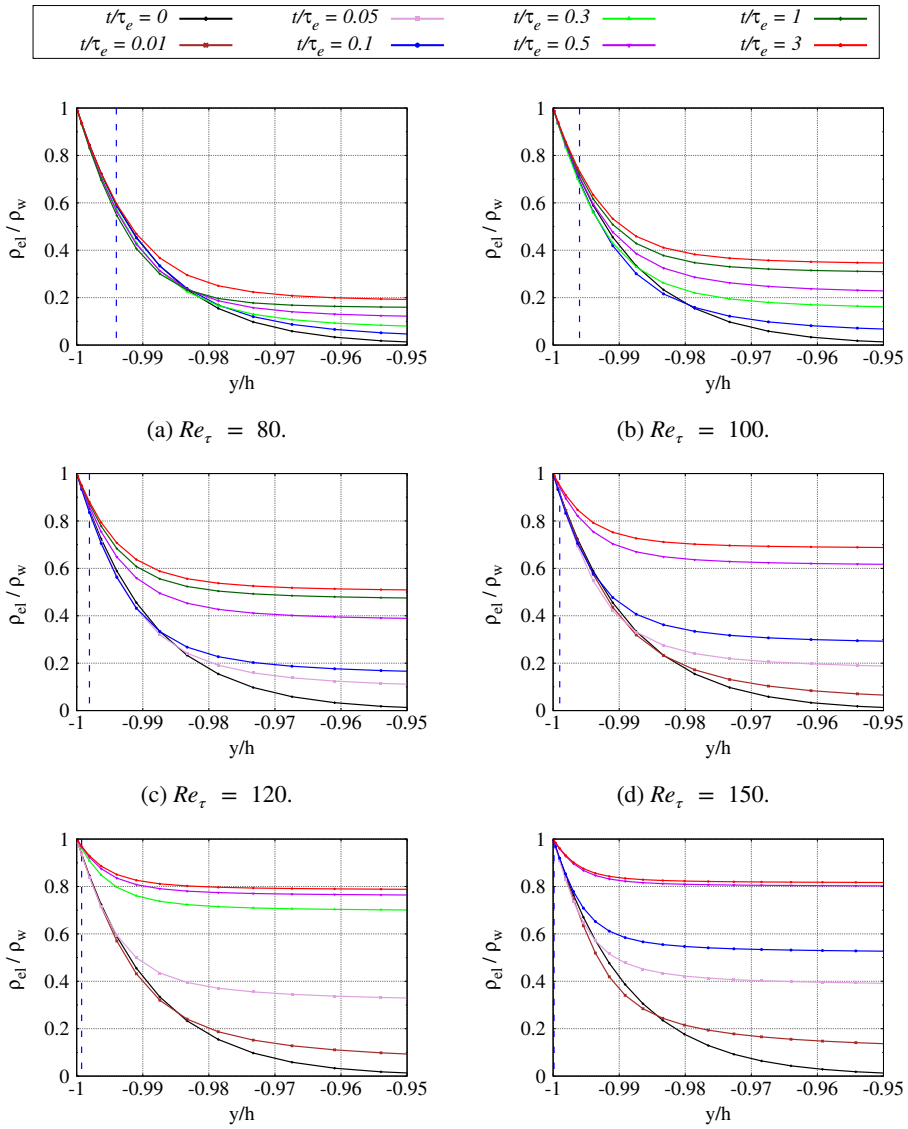

(a) $Re_\tau = 80$. (b) $Re_\tau = 100$.

(c) $Re_\tau = 120$. (d) $Re_\tau = 150$.

(e) $Re_\tau = 180$. (f) $Re_\tau = 210$.

Figure 3.7: Evolution of the charge-density distribution in the diffuse layer for the friction Reynolds numbers considered herein.

value. During this (last) stage of electrification, hereinafter referred to as the *stationary stage*, the profile of the electric charge density varies very little with time. In this manner, during the stationary stage, the total charge in the diffuse layer can be considered as constant.

As soon as the liquid is in contact with the solid, a small percentage of impurities in the liquid dissociate in anions and cations. On the one hand, the anions react with cations from the solid. Whereas, the cations (in the liquid) form a double layer with the electrons of the solid. Please note that these electrons are inevitably generated to compensate the formation of cations from the solid since initially, the surface charge is electrically neutral. Then, these physico-chemical phenomena stop when the concentrations of anions (in the liquid) and cations (from the solid) reach a specific value, *i.e.*, so that the reaction between anions and cations is at equilibrium; see, for example, [95, 96, 98] and references therein. Accordingly, at equilibrium (*i.e.*, for a fully developed diffuse layer), the EDL is electrically neutral. More specifically, the surface charge is charged negatively (due to the presence of electrons at the interface), while the liquid is charged positively (only cations in the Stern layer and mostly cations in the diffuse layer).

However, when turbulence takes ions (mostly cations) away from the diffuse layer, our simulations suggest that the charge imbalance triggers further dissociation of the impurities located in the liquid, thus resulting in a significant increase of the concentration of cations in the liquid, and not only in the diffuse layer (due to the turbulent convection). As is commonly assumed, the solid can provide an "endless supply" of cations. In other words, the anions (in the liquid) are the limiting reagents, see [95, 98]. In this manner, the overall system (consisting of the solid surface and the liquid) remains electrically neutral but there is a flux of cations from the diffuse layer until a new equilibrium state is reached, which corresponds to the stationary stage.

Then, our simulations, on the basis of Figure 3.7, predict two chemical equilibria for the EDL. The first one is when the liquid is at rest or in laminar flow, which corresponds to the fully developed diffuse layer. The second equilibrium is during the stationary stage when the flow is turbulent. In such case and for the purpose of this study, the diffuse layer is said to be *fully perturbed*. We employ this notation mainly to distinguish it from the notion of fully developed diffuse layer whose the latter is no longer appropriate for turbulent flows.

Additionally, the value of the (constant) total charge in the diffuse layer during the stationary stage, which depends on the turbulence intensity of the flow (*cf.* section 3.4.4), is higher than that for a fluid at rest (or, equivalently, in laminar flow). This, in turn, implies that it would not be accurate to assume that the total charge in the diffuse layer is independent of the flow regime, as suggested by Touchard [88, 92] when investigating the charge-density profile in the diffuse layer of a circular pipe. According to that author and as mentioned in section 1.2.4, this hypothesis (referred as H11) is due to the fact that, when the diffuse layer is fully developed, further physico-chemical reactions can no longer take place, which is in contradiction with our predictions.

Further, as suggested by Touchard [88, 92], there is a region adjacent to the wall in which turbulence does not affect the profile of the electric charge density: the *effective diffusion sublayer*. We delimit approximately this zone by the vertical dashed line in Figure 3.7. Please note that a further investigation regarding the effective diffusion sublayer is provided in Chapter 4. Accordingly, the evolution of the diffuse-layer profiles varies dramatically with regards to the turbulence intensity of the flow. In particular, we observe the emergence of three different patterns.

1. Higher turbulence intensities result in a reduction of the duration required to reach the stationary stage. In other words, they result in faster electrification. For instance, the process of flow electrification for $Re_\tau = 180$ (see Figure 3.7e) lasts approximately half as long as for the case $Re_\tau = 120$ (see Figure 3.7c).

2. During the stationary stage, the electric charge density in the (fully perturbed) diffuse layer significantly increases with the turbulence intensity. This phenomenon is even more pronounced in transitional laminar/turbulent flows, corresponding to friction Reynolds numbers ranging approximately between $Re_\tau = 50$ and $Re_\tau = 100$ [168, 174]. For example, the overall value of the electric charge density is almost two times higher for $Re_\tau = 100$ than for $Re_\tau = 80$, while it is also two times higher for $Re_\tau = 180$ than for $Re_\tau = 100$. In addition, at higher turbulence intensities, our simulations suggest that the electric charge density increases with a lower rate than for small values of the friction Reynolds number.

3. The thickness of the unaffected region, *i.e.*, the effective diffusion sublayer, becomes thinner with regards to the turbulence intensity of the flow. For instance,

we denote a ratio of approximately 17 between cases $Re_\tau = 80$ and $Re_\tau = 180$; see Figures 3.7a and 3.7e.

According to the above observations, it is therefore expected that turbulence also strongly affects the streaming current I_{DL} and the amount of charge Q_{DL} in the diffuse layer.

3.4.4 Convection and accumulation of electric-charge carriers

As reported in section 3.3, for laminar channel flows (*i.e.*, $Re_\tau \leq 45$), the streaming current in the diffuse layer I_{DL} scales with the square of the friction Reynolds number. With regards to the amount of charge in the diffuse layer, it is constant, the value of which is given in (3.10) and is denoted as Q^0_{DL}. In turbulent channel flows, our simulations predicted that the behaviors of the streaming current I_{DL} and the amount of charge Q_{DL} are radically different.

We have plotted in Figure 3.8 the variation of the streaming current in the diffuse layer in terms of the Reynolds number. For $Re_\tau \leq 50$, the values of I_{DL} have been obtained via the laminar estimation of (3.14). Whereas, for $80 \leq Re_\tau \leq 210$, the values of the streaming current have been computed via DNS. In the same figure, we also have juxtaposed a fit of this quantity, by using the nonlinear least-squares Marquardt-Levenberg algorithm. It reads, for $Re_\tau \geq 50$,

$$I(Re_\tau) \;=\; C_1 Re_\tau^2 + C_2 Re_\tau + C_3 \;, \tag{3.29}$$

where $C_1 = 8.11 \times 10^{-13}$, $C_2 = -7.86 \times 10^{-11}$, and $C_3 = 1.86 \times 10^{-9}$ are constants and have dimensions of current (Ampere). Based on the aforementioned expression, it is expected that the growth of I_{DL} with respect to Re_τ is accentuated as the turbulence intensity of the flow increases. This can also be deduced from the fact that the streaming current is related directly to the streamwise velocity u (hence the turbulence intensity of the flow) through its definition (3.4). Therefore, turbulence increases dramatically the streaming current in the diffuse layer. By comparison, the values of the streaming current in laminar flow become exceedingly small; see Figure 3.8.

Further, we have plotted in Figure 3.9 the variation of the ratio $Q_{\mathrm{DL}}/Q^0_{\mathrm{DL}}$ in terms of the Reynolds number. According to it, $Q_{\mathrm{DL}}/Q^0_{\mathrm{DL}}$ increases with Re_τ but at a lower rate to that for the streaming current. This is because, contrary to I_{DL}, the streamwise

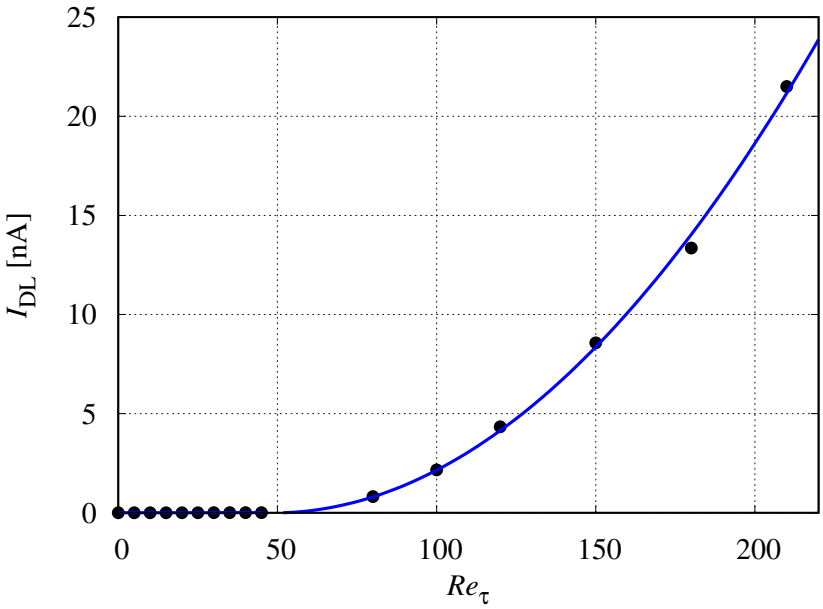

Figure 3.8: Variation of the streaming current in the diffuse layer I_{DL} with Re_τ. The blue curve corresponds to a fit for the streaming current, defined in (3.29). The black circles "•" represent the values of I_{DL}, obtained via DNS when $Re_\tau \geq 50$.

velocity does not appear in the definition of Q_{DL}; *cf.* definition (3.3). Also, due to this particularity, it is expected that the amount of charge in the diffuse layer cannot exceed a specific threshold value. More specifically, this limit can be predicted by assuming that, at infinitely large turbulence intensities (*i.e.*, when the viscous sublayer is exceedingly thin, thus resulting in many eddies in the diffuse layer), the electric charge density becomes exceedingly close to its value at the wall ρ_w. Then, by replacing ρ_{el} by ρ_w in equations (3.1) and (3.3), the limit reads,

$$\frac{Q_{DL}}{Q^0_{DL}} = 4\frac{\cosh(h/\lambda_D)}{\sinh(h/\lambda_D)+\sinh((-h+4\lambda_D)/\lambda_D)} \approx 3.92\,. \tag{3.30}$$

The aforementioned expression corresponds to the theoretical limit of an infinite Reynolds number with zero charge relaxation (*i.e.*, $\sigma = 0$). However, please note that due to the presence of the ohmic resistance in the conservation equation (2.21),

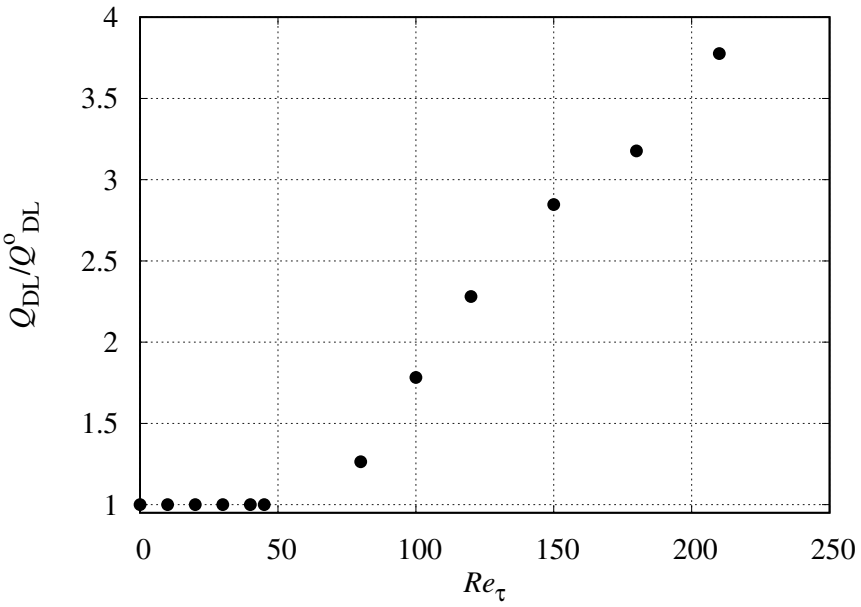

Figure 3.9: Variation of the ratio Q_{DL}/Q^0_{DL} with Re_τ. The black circles "•" represent the values of Q_{DL}/Q^0_{DL}, computed via DNS when $Re_\tau \geq 50$.

the electric charge density ρ_{el} cannot be everywhere equal to ρ_w, regardless of the turbulence intensity of the flow.

As shown in Figure 3.7, inside the unaffected region, the charge-density profile is similar to that in a fluid at rest. In particular, in this zone, ρ_{el} differs from ρ_w. Nonetheless, our numerical results concerning the streaming current and the amount of charge predict that flow electrification increases significantly with the turbulence intensity of the flow, thereby increasing the risk of electrostatic hazards. As reported by Klinkenberg and van der Minne [30], these risks include ignitions, fires, and explosions of liquid hydrocarbons such as benzene.

3.5 Concluding remarks

In this chapter we presented the charge-density distribution in the diffuse layer and the influence of the flow on it. First, we observed that the process of charge diffusion is

fundamental for the development of the diffuse layer. Otherwise, it simply results in charge relaxation, hence no electrification. For a fluid at rest, we derived an analytical expression for the electric charge density. Further, we estimated the thickness of the diffuse layer through the Debye length. This confirmed the importance of the Debye length in flow electrification. In particular, this phenomenon is more likely to occur when handling dielectric liquids such as benzene.

For laminar channel flow, we highlighted that the transport of charge from the diffuse layer towards the bulk of the channel does not occur. As a result, the electric charge density has the same profile as if the fluid was at rest. However, the flowing liquid generates a streaming current in the diffuse layer, which consists of ions advected by the flow parallel to the wall. We established that this quantity increases linearly in terms of the mean velocity, as in laminar pipes and rectangular duct flows.

Further, our simulations predicted that the induction of a turbulent channel flow dramatically modifies the charge-density distribution in the diffuse layer. In particular, further physico-chemical phenomena take place in the EDL until the charge imbalance caused by the turbulent structures of the flow is stopped. Therefore, two chemical equilibria exists in the EDL. The first equilibrium occurs when the liquid is at rest (or in laminar flow), corresponding to the notion of fully developed diffuse layer. Whereas, the second equilibrium solely occurs in turbulent flows during the last stage of electrification, called stationary stage.

Additionally, our simulations predicted that in a region adjacent to the wall, called effective diffusion sublayer, the charge-density profile remains the same with time. However, the thickness of this region decreases with the turbulence intensity of the flow. Accordingly, at high turbulence intensity, the streaming current becomes exceedingly large. Notably, this increase is much more important than in the case of a laminar channel flow.

All the results presented through this chapter lead us to believe that the phenomenon of turbulent flow electrification goes beyond the diffuse layer, namely in the whole channel. In particular, it is expected that, in turbulent channel flows, the charge-density distribution is also affected in the bulk of the flow domain. Therefore, the understanding of this phenomenon requires deeper investigations, which are the subject of the next chapter.

CHAPTER 4

Direct numerical simulations of turbulent flow electrification

4.1 Introduction

In Chapter 3, we have investigated the charge-density distribution in the diffuse layer in terms of the flow regime. In a similar manner, we examine in this chapter the transport of electric-charge carriers in the bulk of the channel. For most applications in the process industries, except in microfluidics, this region is considerably thicker than the diffuse layer. In particular, the analysis of the phenomenon of flow electrification should not be restricted uniquely to the diffuse layer, as is common practice. When the flow is laminar, investigating the charge-density distribution in the bulk of the channel is irrelevant since there are no electric-charge carriers, as demonstrated in section 3.3. On the other hand, according to the numerical results obtained in section 3.4, it is expected that a turbulent flow induces a transport of electric-charge carriers from the diffuse layer towards the bulk of the channel.

The phenomenon of charge convection may, in turn, considerably modify the total charge and streaming current in the liquid. Subsequently, we address this issue in Section 2. In addition, we conduct in Section 3 a thorough analysis of turbulent flow electrification via first- and second-order statistics concerning the electric charge den-

A part of the results reported herein have been published in: M. Calero, H. Grosshans, M. Papalexandris, Electrification in turbulent channel flows of liquid dielectrics, *Phys. Fluids* 35 (4) (2023) 045119. doi: 10.1063/5.013842510 [175]

Case	Re_τ	Re_E	Pe	Re_λ
A1	80	4.06×10^1	3.09×10^5	8.72×10^1
A2	100	5.08×10^1	3.86×10^5	8.72×10^1
A3	120	6.10×10^1	4.63×10^5	8.72×10^1
A4	150	7.60×10^1	5.79×10^5	8.72×10^1
A5	180	9.14×10^1	6.95×10^5	8.72×10^1
A6	210	1.06×10^2	8.10×10^5	8.72×10^1
B1	180	9.14×10^1	9.01×10^4	2.61×10^2
B2	180	9.60×10^2	6.95×10^5	2.61×10^2
B3	180	9.14×10^1	7.29×10^6	2.90×10^1
B4	180	1.18×10^1	6.95×10^5	2.90×10^1

Table 4.1: Summary of the dimensionless parameters for the DNS considered in our study.

sity. In particular, we introduce the notion of *fluctuating charge-density variance*. By analyzing its budget, we can explain the relative contributions of physical processes that govern the motion of the electric charge density. Finally, we derive in Section 4 an expression for the mean charge-density profile via different assumptions. More specifically, this closed-form profile extends the procedure of Abedian and Sonin [61] for our specific case of turbulent channel flows.

To our knowledge, this is the first numerical study of the process of flow electrification in turbulent flows. Additionally, this study accesses for the first time in detail the role of flow turbulence. In what follows, we provide the values of the physical parameters for the various cases considered herein and define several quantities for the statistical analysis of the phenomenon of turbulent flow electrification.

4.1.1 Description of the flow cases

Tables 4.1 and 4.2 summarize the dimensionless and dimensional parameters for the DNS considered in this study. In particular, Table 4.1 includes four dimensionless parameters: the friction (Re_τ) and electric (Re_E) Reynolds numbers, the Péclet number (Pe), and the Debye number (Re_λ). Whereas, Table 4.2 presents four (dimensional) quantities: the friction velocity (u_τ), the electrical conductivity (σ), the diffusion coef-

Case	u_τ [m/s]	σ [S/m]	D [m^2/s]	λ_D [m]
A1	1.11×10^{-2}	1.10×10^{-12}	1.80×10^{-10}	5.73×10^{-5}
A2	1.39×10^{-2}	1.10×10^{-12}	1.80×10^{-10}	5.73×10^{-5}
A3	1.67×10^{-2}	1.10×10^{-12}	1.80×10^{-10}	5.73×10^{-5}
A4	2.08×10^{-2}	1.10×10^{-12}	1.80×10^{-10}	5.73×10^{-5}
A5	2.50×10^{-2}	1.10×10^{-12}	1.80×10^{-10}	5.73×10^{-5}
A6	2.92×10^{-2}	1.10×10^{-12}	1.80×10^{-10}	5.73×10^{-5}
B1	2.50×10^{-2}	1.10×10^{-12}	1.62×10^{-9}	1.72×10^{-4}
B2	2.50×10^{-2}	1.22×10^{-13}	1.80×10^{-10}	1.72×10^{-4}
B3	2.50×10^{-2}	1.10×10^{-12}	2.00×10^{-11}	1.91×10^{-5}
B4	2.50×10^{-2}	9.90×10^{-12}	1.80×10^{-10}	1.91×10^{-5}

Table 4.2: Summary of the dimensional parameters for the DNS considered in our study.

ficient (D), and the Debye length (λ_D). Please note that these two tables are related via the expressions derived in section 2.2.3. For this work, we separate our simulations into two groups: one for the variations of the turbulence intensity of the flow; and one for the variations of the Debye length.

Group A: variation of the turbulence intensity of the flow (Cases A1-A6)

The first group consists of six DNS corresponding to those presented in section 3.4.1. Hence, we employ the same grids and we use the values of the material properties of benzene listed in Table 2.2. In this group, the friction Reynolds number ranges from $Re_\tau = 80$ (A1) to $Re_\tau = 210$ (A6); see Table 4.1. Accordingly, comparisons between simulations of cases in Group A assess the role of the turbulence intensity on flow electrification.

Group B: variation of the Debye length (Cases B1-B4)

The second group consists of DNS of four cases at $Re_\tau = 180$ but with different Debye lengths. For this reason, the computational mesh consists of $192 \times 129 \times 160$ grid cells, corresponding to the mesh used when conducting DNS with Case A5 (*cf.* section 3.4.1). In these simulations, we employ an artificially modified Debye length.

More specifically, we increase λ_D by a factor of three in Case B1 via D and in Case B2 via σ. On the other hand, we decrease λ_D by the same factor in Cases B3 (decreased diffusion) and B4 (increased conductivity).

For comparison purposes, the DNS results obtained with Case A5, corresponding to $Re_\tau = 180$ with an unmodified Debye length, are also provided when comparing the different cases of Group B. The objective of the simulations of the cases of this group is to determine the effects of the electrical conductivity, the diffusion coefficient, and the Debye length in turbulent flow electrification. In an equivalent manner, these simulations help to assess the role of the three dimensionless parameters mentioned in section 2.2.3. These are the electric Reynolds number Re_E (the effect of which is assessed via comparisons between Cases A5, B2, and B4), the Péclet number Pe (comparisons between Cases A5, B1, and B3), and the Debye number Re_λ (comparisons between Cases A5 and B1-B4). Furthermore, it is worth adding that the mass density ρ, the electrical permittivity ϵ, the kinematic viscosity ν, and the half-width of the domain h remain unchanged throughout this study; the values of which are reported in Table 2.2.

Initial profile of the electric charge density

In line with section 3.4.1, a preliminary simulation of turbulent channel flow in absence of electric charge is performed initially. When the flow becomes fully developed, an initial profile for the electric charge density is applied. As illustrated in Figure 4.1, the initial profile of ρ_{el} depends on the value of the Debye length. More specifically, the initial thickness of the diffuse layer is thicker for Cases B1-B2 ($\gamma = 6.45 \times 10^{-4}$ m) than for Cases A1-A6 ($\gamma = 2.15 \times 10^{-4}$ m). By contrast, it is thinner for Cases B3-B4, namely $\gamma = 7.17 \times 10^{-5}$ m. From Figure 4.1, we observe that the electrical conductivity σ and the diffusion coefficient D act only via the Debye length. In other words, initially, profiles of Cases B1 (increased diffusion) and B2 (decreased conductivity) are similar; as well as Cases B3 (decreased diffusion) and B4 (increased conductivity). As will be established later, as soon as the turbulent flow is induced, this feature no longer applies. In particular, the ohmic resistance (conductive currents) and the diffusive term of (2.21) play different roles in turbulent flow electrification.

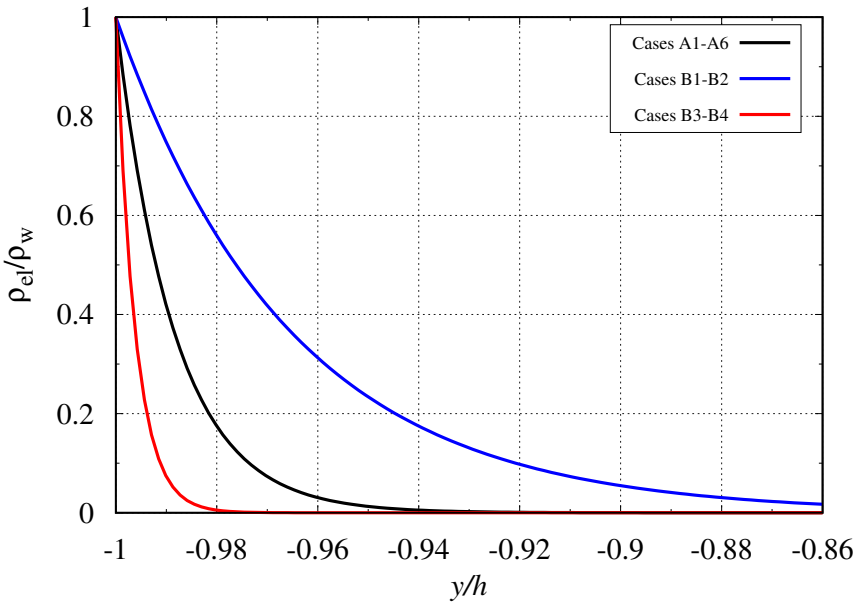

Figure 4.1: Initial profiles of the electric charge density for all cases considered herein.

Parallelization and cost simulations

The preliminary simulations for the cases examined herein lasted between 50 and 80 flow-through times, where a flow-through time is equal to $4\pi h/u_{\mathrm{m}}$. As an example, for simulations of cases in Group B ($Re_\tau = 180$), the computational time for one flow-through time corresponds approximately to 160 minutes. As mentioned in section 2.3, pafiX is parallelized via the MPI protocol. Further, pafiX employs a parallel domain decomposition in the streamwise x direction, which ensures a load balance between processors [146]. As a result, the number of processors is limited by the number of grid points used in the streamwise direction. For all the DNS considered herein, 48 processors (AMD Epyc Rome) were employed.

The computational cost to simulate the process of flow electrification depends on the specific case examined. For example, in Case A1 ($Re_\tau = 80$), 135 flow-through times were required to reach the stationary stage. Whereas, it required 95 flow-through times to reach the stationary stage in Case A6 ($Re_\tau = 210$). Once the stationary

	Distance	Time	Velocity	Charge density
Group A	h	$\tau_e = \frac{\epsilon}{\sigma}$	$\frac{h}{\tau_e} = \frac{h\,\sigma}{\epsilon}$	ρ_w
Group B	h	$\tau_c = \frac{h}{u_\tau}$	$\frac{h}{\tau_c} = u_\tau$	ρ_w

Table 4.3: Reference values (distance, time, velocity, and charge density) for all simulations considered herein.

stage is reached, in each simulation, the period of averaging lasted approximately 80 flow-through times. Thus, in general, the cost for simulating the process of charge generation and taking statistics is approximately two times higher than performing the preliminary simulations, *i.e.*, obtaining a fully developed turbulent channel flow in absence of charges.

4.1.2 Notation

The time and area (at the xz-plane) average of a generic quantity ψ is denoted by $\langle\psi\rangle$. We indicate the time average of ψ by $\langle\psi\rangle_t$, while area averaging is denoted by $\langle\psi\rangle_{xz}$. Further, ψ' stands for the fluctuating component of ψ; see (3.24). Finally, we denote the root-mean-square (r.m.s) of the fluctuating component ψ' by ψ_{rms}. It reads,

$$\psi_{rms} = \langle\psi'\psi'\rangle^{1/2} . \tag{4.1}$$

The turbulent kinetic energy (TKE) is defined as [168, 169],

$$k = \frac{1}{2}\langle u'u' + v'v' + w'w'\rangle_t . \tag{4.2}$$

In a similar manner, one can introduce below the notion of fluctuating charge-density variance (FCV). It corresponds to an equivalent of the turbulent kinetic energy for the electric charge density. Let us define k_{el} by,

$$k_{el} = \frac{1}{2}\rho'_{el}\rho'_{el} . \tag{4.3}$$

Then, the fluctuating charge-density variance (FCV) equals,

$$\text{FCV} = 2\langle k_{el}\rangle_t = \langle\rho'_{el}\rho'_{el}\rangle_t . \tag{4.4}$$

With regards to non-dimensionalization, we note the following. All the figures presented in Section 3 show results of dimensionless quantities. Accordingly, we employ the half-width of the channel h as the reference length scale. However, on certain occasions (explicitly mentioned), we measure distances in wall units. The reference charge density is the prescribed value at the walls ρ_{w}. Moreover, the reference time scale corresponds to τ_{e} for simulations of cases in Group A (variation of Re_τ). It is τ_{c} for simulations of cases in Group B (variation of λ_{D}). Then, the reference velocity scale is respectively equal to $h\sigma/\epsilon$ and u_τ for simulations of cases in Groups A and B. We summarize these modifications in Table 4.3. For simplicity of notation, we do not use different symbols for dimensionless quantities because it seems straightforward to determine if a given variable is provided in dimensionless or dimensional form without loss of clarity.

4.2 Convection of charge towards the bulk of the flow domain

This section describes the transport of electric-charge carriers (ions) from the diffuse layer towards the bulk of the channel. As mentioned in section 4.1, this phenomenon takes place only for turbulent flows. Accordingly, we present below numerical results concerning the electrification rate, the streaming current in the liquid, and the spatial variation of the electric charge density. In our study, the *electrification rate* is defined as the rate of change of the area-averaged electric charge $\langle \rho_{\mathrm{el}} \rangle_{xz}$ at the midplane of the flow domain.

4.2.1 Electrification rate

In Figure 4.2, we present plots of the evolution of $\langle \rho_{\mathrm{el}} \rangle_{xz}$ located at the midplane for simulations of cases in Group A. According to this figure, we identify three stages of electrification, regardless of the turbulence intensity of the flow. The first one is characterized by a rapid and almost linear buildup of charge, *i.e.*, at a high and almost constant electrification rate. In the second stage, the electrification rate decreases, implying that the ohmic resistance becomes progressively more significant and counter-acts the convective transport of charge. In general, the duration of the first stage is approximately half of the duration of the second one. For example, in Case A3 ($Re_\tau = 120$), the first stage terminates at $t/\tau_{\mathrm{e}} \approx 0.5$ while the second one lasts from $t/\tau_{\mathrm{e}} \approx 0.5$ until

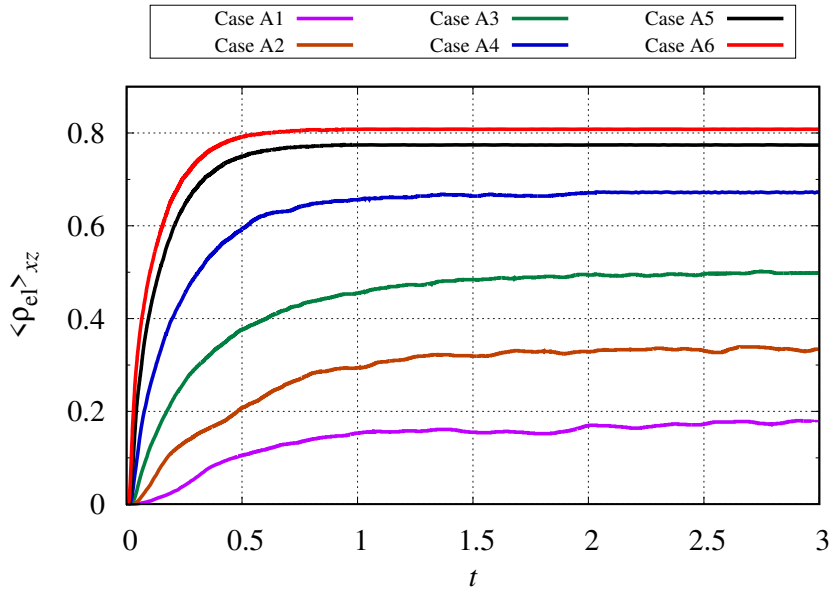

Figure 4.2: Evolution of the area-averaged charge density $\langle \rho_{\mathrm{el}} \rangle_{xz}$ at the midplane ($y = 0$) for simulations of cases in Group A.

$t/\tau_{\mathrm{e}} \approx 1.5$. Finally, in the third stage, $\langle \rho_{\mathrm{el}} \rangle_{xz}$ becomes statistically stationary. As mentioned in section 3.4.3, this period corresponds to the stationary stage, *i.e.,* when the diffuse layer is considered fully perturbed. During the stationary stage, the convective transport of charge in the bulk is counter-balanced by the ohmic resistance. Accordingly, the overall charge has reached its peak value, as is the case in the diffuse layer; *cf.* section 3.4.

Upon inspection of the slopes of $\langle \rho_{\mathrm{el}} \rangle_{xz}$ at the midplane, as illustrated in Figure 4.2, we readily infer that the electrification rate increases excessively in terms of Re_τ. For instance, with $Re_\tau = 180$ (A5), the electrification rate is approximately two times higher than in Case A3, for which $Re_\tau = 120$. Further, the required time for the total charge to reach its final value scales inversely. For example, in Case A3, the combined duration of the first two stages is approximately $1.5\tau_{\mathrm{e}}$. In contrast, in Case A5, it is only $0.5\tau_{\mathrm{e}}$. The final value of $\langle \rho_{\mathrm{el}} \rangle_{xz}$ at the midplane also increases with the turbulence intensity of the flow. Nonetheless, the resulting gap between two peaks reduces with Re_τ.

For $Re_\tau = 180$ (A5), the peak is approximately 15% higher than that for $Re_\tau = 150$ (A4). Between $Re_\tau = 210$ (A6) and $Re_\tau = 180$, it is approximately 5%. During the stationary stage, the electric charge density continues to oscillate weakly with time. These oscillations become significant for transitional laminar/turbulent flows (*i.e.*, $Re_\tau \leq 100$), whereas they substantially reduce at higher turbulence intensities; see, for instance, a comparison between Cases A1 and A6 in Figure 4.2.

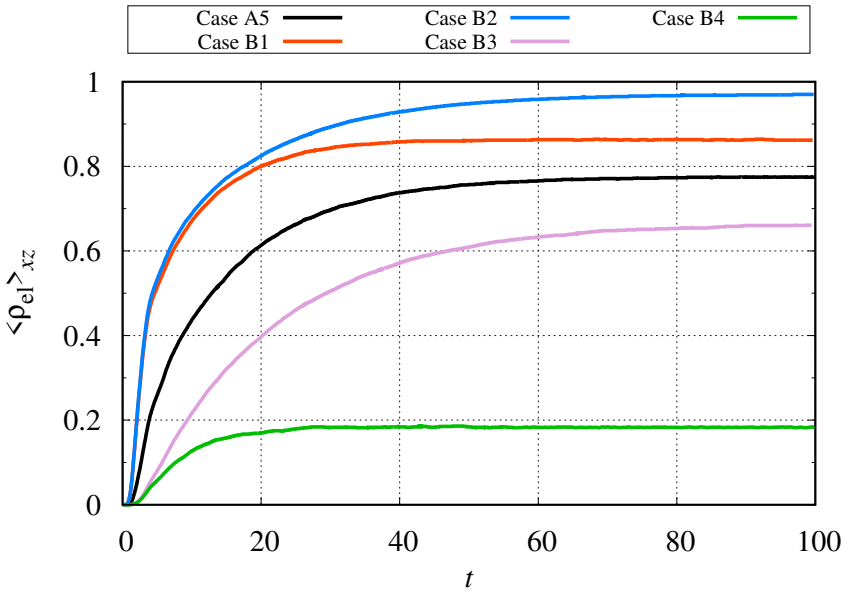

Figure 4.3: Evolution of the area-averaged charge density $\langle \rho_{\mathrm{el}} \rangle_{xz}$ at the midplane for simulations of cases in Group B.

Similarly, we have plotted in Figure 4.3 the evolution of the area-averaged charge density $\langle \rho_{\mathrm{el}} \rangle_{xz}$ at the midplane for simulations of cases in Group B. A comparison of the results between Cases B2, B4, and A5 indicates that the effect of the electrical conductivity σ (hence τ_{e}; see (2.26)) on the electrification rate is significant. For example, in Case B4, the liquid (benzene) gets electrified approximately three times faster than in Case A5. Whereas in Case B2, the time to reach the stationary stage is longer than in Case A5. Additionally, σ has a noticeable effect on the electric charge's final value.

According to our simulations, when σ increases by a factor of 9 (B4), the peak value of the midplane charge-density $\langle \rho_{\mathrm{el}} \rangle_{xz}$ decreases by approximately 76%.

Further, increasing the conductivity results in a mild increase of the fluctuations. However, the oscillation amplitude is low compared to transitional laminar/turbulent flows; see comparisons between Cases A1 and B4. By comparing the results for Cases B1, B3, and A5, we readily infer that the electrification rate also depends on the diffusion coefficient (hence τ_{d}; see (2.26)). The diffusion process affects flow electrification since the electric charge density increases with Re_τ. Nonetheless, the influence of the electrical conductivity σ (or, equivalently, τ_{e}) on both the electrification rate and the final value of $\langle \rho_{\mathrm{el}} \rangle_{xz}$ is more significant than the diffusion coefficient D (or, equivalently, τ_{d}). Our simulations also predict that, during the first stage of electrification (rapid buildup of charge), the profile of the electric charge density $\langle \rho_{\mathrm{el}} \rangle_{xz}$ is almost identical for Cases B1-B2 ($t/\tau_{\mathrm{c}} < 10$), and for Cases B3-B4 ($t/\tau_{\mathrm{c}} < 3$). In other words, during this stage, the Debye length controls the electrification rate.

Concerning the influence of the dimensionless parameters presented in Table 4.1 (*i.e.*, Re_τ, Re_{e}, Pe, and Re_λ), we note the following. The electrification rate and the peak value of the electric charge density increase with respect to the electric Reynolds number Re_{e}. This rise is due to two distinct factors. The first one concerns the charge-relaxation time scale τ_{e} via the electrical conductivity σ. The second one concerns the convection time scale τ_{c} via the friction velocity u_τ. According to Figures 4.2 and 4.3, the convection time scale τ_{c} has a stronger influence than the charge-relaxation time scale τ_{e}. For example, a comparison between Cases A1 and B4 suggests that the final value of $\langle \rho_{\mathrm{el}} \rangle_{xz}$ is almost the same. On the one hand, it required an increase by a factor of 9 for τ_{e}, while the convection time scale τ_{c} only decreased by a factor of 2.25. Similarly, one can also observe that the charge diffusion time scale τ_{d} has a weaker influence than the charge-relaxation time scale τ_{e} (hence τ_{c}). In other words, the Péclet number is of less significance compared to both the electric and friction Reynolds numbers. This is directly inferred upon comparisons between Cases B1-B2 or B3-B4. Finally, by comparing the plots of $\langle \rho_{\mathrm{el}} \rangle_{xz}$ at the midplane in Figures 4.2 and 4.3, we observe that the oscillations during the stationary stage are primarily caused by the turbulent convective term of (2.21). In particular, these oscillations are significant only in transitional flows. This is explained by the fact that as the turbulence inten-

sity increases, the mixing of electric-charge carriers becomes more efficient, thereby reducing the fluctuations of ρ_{el}.

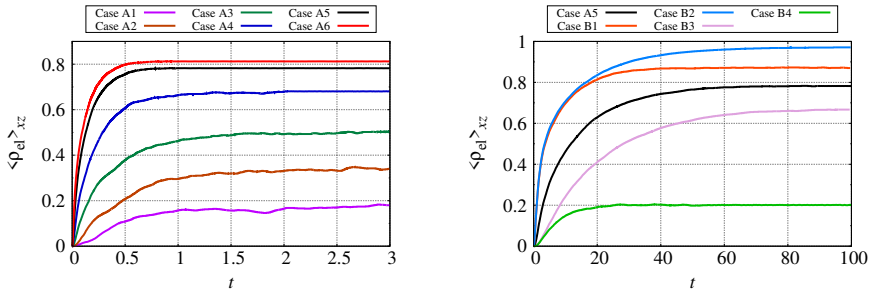

(a) Group A.

(b) Group B.

Figure 4.4: Evolution of the area-averaged charge density $\langle \rho_{el} \rangle_{xz}$ at $y = \pm h/2$ for simulations of cases in Groups A and B.

For the sake of completeness, we have plotted in Figure 4.4 the evolution of $\langle \rho_{el} \rangle_{xz}$, located at $y = \pm h/2$ for simulations of cases in Groups A and B. Accordingly, regardless of the case, the profiles of $\langle \rho_{el} \rangle_{xz}$ at $y = 0$ and $y = \pm h/2$ are nearly identical. This implies that, for a given Reynolds number, the evolution of the electric charge density in the bulk of the channel is almost the same.

4.2.2 Spatial variation of the electric charge density

As discussed in section 3.4.2, the fully developed channel flow is statistically one-dimensional. However, at any given instance, the velocity field $\boldsymbol{u}$ varies with respect to the streamwise x and spanwise z directions, via its fluctuation $\boldsymbol{u}'$. In what follows, we investigate if this pattern is also present for the electric charge density.

In Figures 4.5 and 4.6, we present contour plots for ρ_{el} and u at the xy- and yz-planes, respectively. These plots correspond to Case A5 ($Re_\tau = 180$) at $t/\tau_e = 3$, *i.e.*, when the charge-density distribution is statistically stationary. According to them, the contour plots of the instantaneous electric charge density and the streamwise velocity bear certain similarities. More specifically, we observe in both figures the same turbulent structures located at the same positions between these two quantities. Further, this pattern is not restricted to a specific zone, such as the diffuse layer, but applies every-

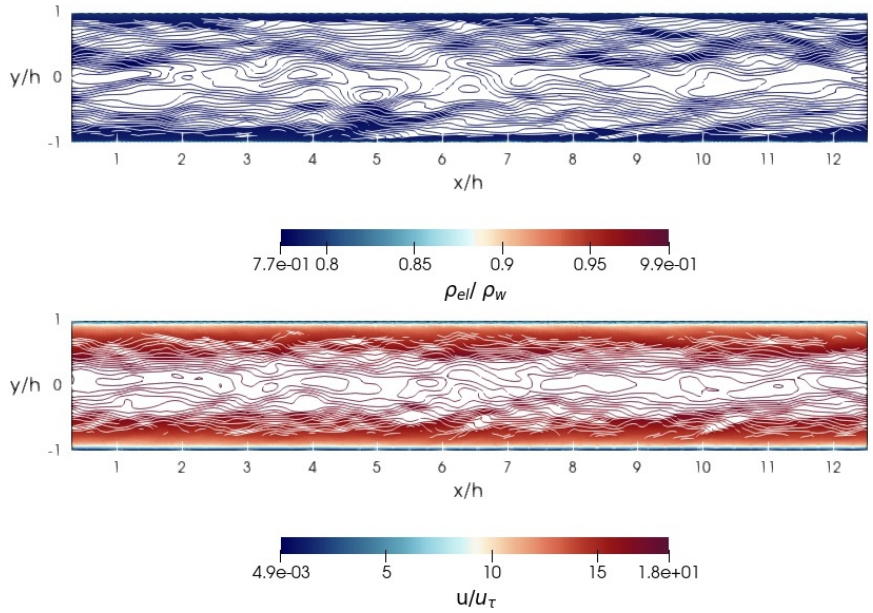

Figure 4.5: Instantaneous contour plots of ρ_{el} (top) and u (bottom) at the xy-plane during the statistically stationary stage. Top: the electric charge density contains 400 contours of equally spaced contour-levels. Bottom: the streamwise velocity contains 100 contours of equally spaced contour-levels.

where in the flow domain. Consequently, our findings concerning the electrification rate and the spatial variation of the electric charge density impel us to consider that turbulent flow electrification takes place everywhere in the flow domain. In particular, it is essential to compute numerically the streaming current and the total charge everywhere in the liquid, and not only in the diffuse layer as is common practice; see, for example, [88, 92, 93, 98, 106] and references therein.

4.2.3 Accumulation of electric-charge carriers in the bulk

As described in section 3.4.3, in the diffuse layer, turbulence results in a monotonically increasing streaming current while the total charge reaches a plateau, corresponding to $3.92Q^0_{\mathrm{DL}}$ in our study; *cf.* (3.30). Similarly, our simulations indicate that the streaming current I and the total charge Q follow, respectively, the same behavior as I_{DL} and

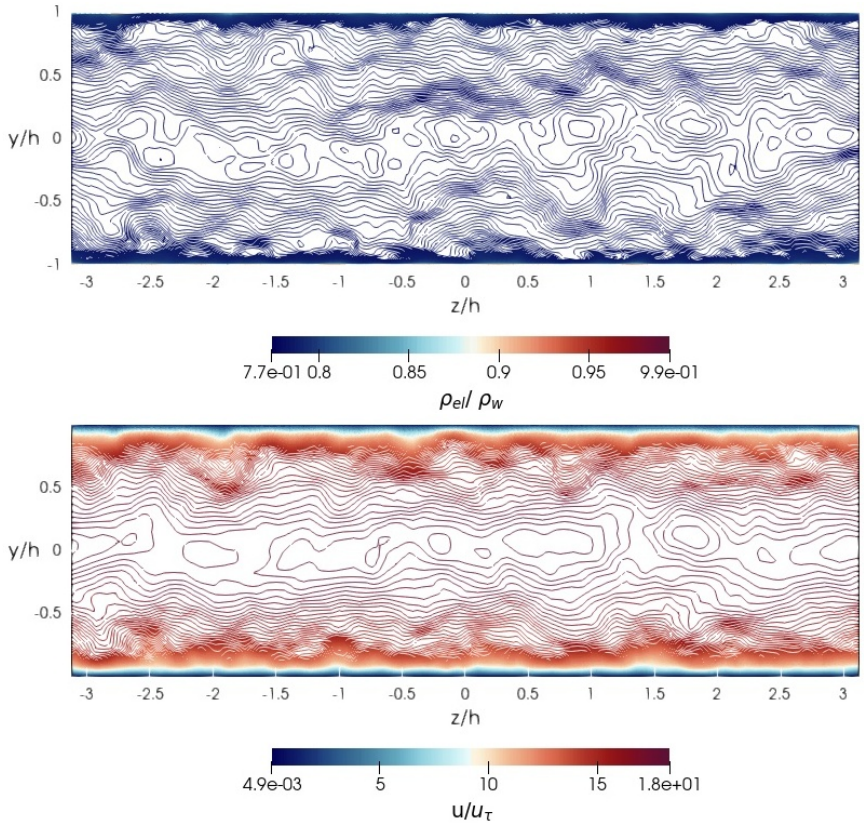

Figure 4.6: Instantaneous contour plots of ρ_{el} (top) and u (bottom) at the yz-plane during the statistically stationary stage. Top: the electric charge density contains 400 contours of equally spaced contour-levels. Bottom: the streamwise velocity contains 100 contours of equally spaced contour-levels.

Q_{DL}; see Figures 4.7a and 4.8a. Further, we present in Figure 4.7b the ratio between the total streaming current I and the streaming current in the diffuse layer I_{DL}. As can be seen from this figure, I/I_{DL} decreases with Re_τ. In other words, at high turbulence intensity, the convection of charge in the diffuse layer becomes significant so as to be comparable with the convection of charge in the bulk of the channel. Indeed, as mentioned in section 3.4, the viscous sublayer covers only a small portion of the diffuse layer at high values of Re_τ. Therefore, the velocity becomes more and more consid-

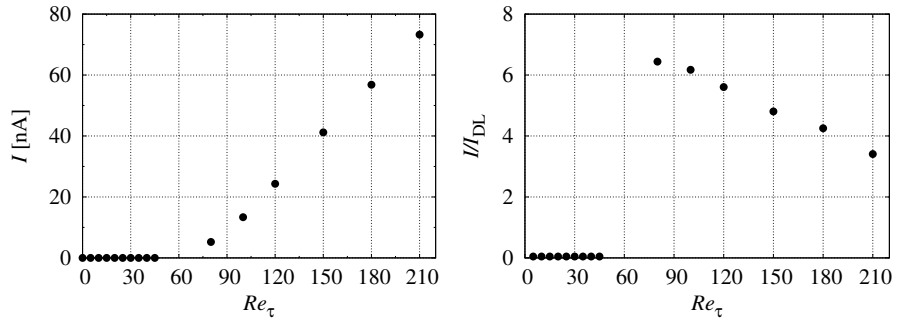

(a) Streaming current I. (b) Ratio I/I_{DL}.

Figure 4.7: Numerical estimation of the total streaming current I (a) and the ratio I/I_{DL} (b) in terms of the friction Reynolds numbers considered herein.

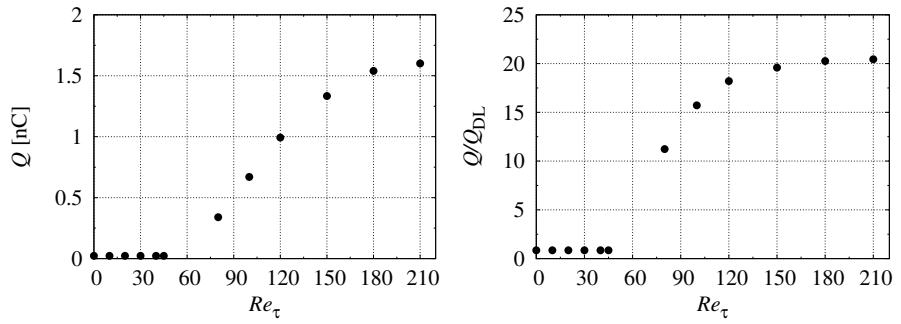

(a) Total charge Q. (b) Ratio Q/Q_{DL}.

Figure 4.8: Numerical estimation of the total charge Q (a) and the ratio Q/Q_{DL} (b) in terms of the friction Reynolds numbers considered herein.

erable in this region, resulting in a decrease of I/I_{DL} with respect to the turbulence intensity of the flow.

In addition, we have plotted in Figure 4.8b the ratio between the total charge Q and the amount of charge in the diffuse layer Q_{DL}. According to it, the ratio Q/Q_{DL} and the accumulation of electric carriers increase as Re_τ increases. As a result, the amount of electric-charge is significantly larger in the bulk of the channel than in the diffuse layer. We attribute this to the fact that the thickness of the diffuse layer is thin compared to the bulk of the channel: only 1.11% of the channel is covered by

the diffuse layer. More specifically, via definitions (3.1) and (3.3), it is expected that Q/Q_{DL} converges towards $h/4\lambda_{\mathrm{D}}$. Thus, a thicker diffuse layer implies a lower value for the ratio Q/Q_{DL}.

Globally, our simulations show that the electrification rate, the spatial variations, the total charge, and the streaming current increase considerably with the turbulence intensity of the flow. These patterns are predictable since, as suggested above, the thickness of the viscous sublayer decreases with Re_τ. Therefore, the number of turbulent structures inside the diffuse layer increases.

4.3 Charge-density statistics

In this section, we present first- and second-order statistics for the electric charge density during the third stage of electrification. These statistics allow a better understanding of the phenomenon of turbulent flow electrification.

4.3.1 First- and second-order statistics

The convective (or advective) term $\rho_{\mathrm{el}}u$ is fundamental for estimating flow electrification since it directly appears in the definition (3.2) of the total streaming current I. Accordingly, we have plotted respectively in Figures 4.9 and 4.10 the mean profiles of $\rho_{\mathrm{el}}u$ and u for simulations of cases in Group A. In general terms, we observe from these figures that the profiles of the convective term bear certain similarities with the mean streamwise velocity $\langle u\rangle$. More specifically, the profile of $\langle\rho_{\mathrm{el}}u\rangle$ can be approximated by a logarithmic growth away from the wall, as is the case for $\langle u\rangle$ at $y^+ > 30$; *cf.* section 3.4.2. Further, this trend accentuates at higher turbulence intensities. According to Figure 4.11, $\langle\rho_{\mathrm{el}}u\rangle$ increases almost linearly with the wall unit y^+ inside the viscous sublayer, *i.e.*, $y^+ < 5$, as is the case for $\langle u\rangle$; see, for example, Case A5. In other words, for large values of Re_τ, the convective term $\langle\rho_{\mathrm{el}}u\rangle$ can be approximated by $\langle\rho_{\mathrm{el}}u\rangle \approx \langle\rho_{\mathrm{el}}\rangle\langle u\rangle$. Additionally, our simulations suggest that both the electrical conductivity and the diffusion coefficient affect $\langle\rho_{\mathrm{el}}u\rangle$. According to Figure 4.12, there is a symmetry between the profiles of Cases B1 and B3 with respect to Case A5. Consequently, increasing or decreasing D by the same factor (9 in this study) results in an opposite effect with the same magnitude. Based on the DNS results with Cases B2 and B4 in Figure 4.12, we deduce that this feature does not apply to the electrical

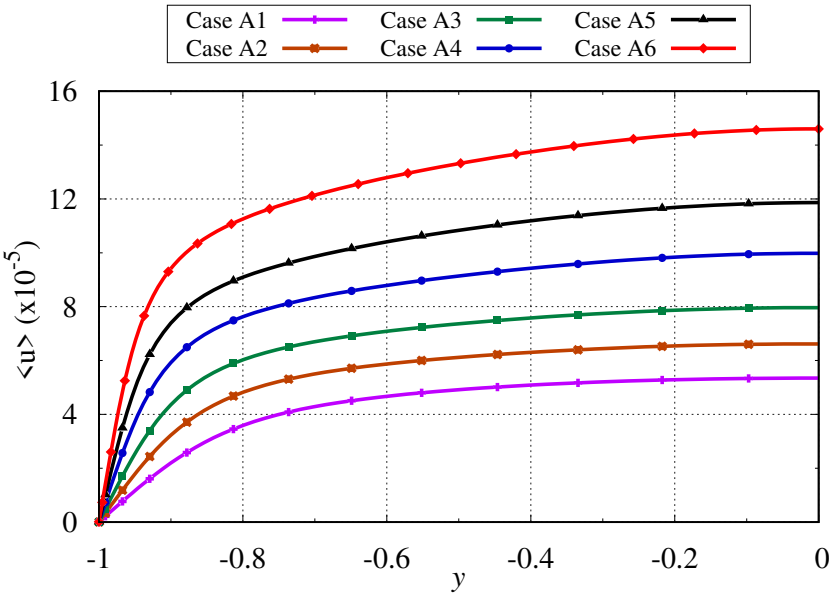

Figure 4.9: Profiles of the mean streamwise velocity $\langle u \rangle$ for the friction Reynolds numbers considered herein.

conductivity. Further, as was the case for the electrification rate, σ (or, equivalently, τ_e) is more influential than D (or, equivalently, τ_d). More specifically, compared to the ohmic resistance, the influence that the process of charge diffusion has on the total charge accumulated in the bulk of the channel may be regarded as insignificant.

Another relevant term for a better understanding of flow electrification is the spanwise turbulent flux $\langle \rho_{el} v \rangle$ since it appears directly in the mean charge-density equation. This equation is obtained by applying the time and area averaging operator, $\langle\ \rangle$, in (2.21). It reads,

$$\frac{\mathrm{d}}{\mathrm{d}y}\langle \rho_{el} v \rangle \;=\; -\frac{\sigma}{\epsilon}\langle \rho_{el} \rangle + D\frac{\mathrm{d}^2}{\mathrm{d}y^2}\langle \rho_{el} \rangle \,. \tag{4.5}$$

Please note that, since $\langle v \rangle = 0$ [168], we have,

$$\langle \rho_{el} v \rangle \;=\; \langle \rho_{el}^{'} v^{'} \rangle \,. \tag{4.6}$$

Next, we provide plots of the spanwise turbulent flux in Figures 4.13 and 4.14 for the simulations of the cases of Groups A and B, respectively. First of all, we note that the

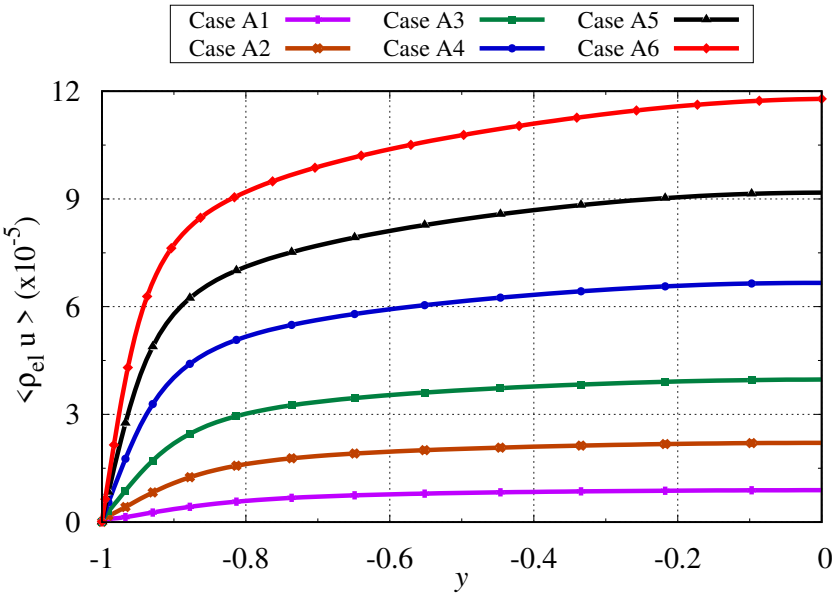

Figure 4.10: Profiles of $\langle \rho_{el} u \rangle$ for simulations of cases in Group A.

profiles of $\langle \rho_{el} v \rangle$ are anti-symmetric with respect to the midplane, in contrast to $\langle \rho_{el} u \rangle$. We can explain this feature from (4.5). Due to the symmetry of $\langle \rho_{el} \rangle$ and its second-order derivative, the right-hand side of (4.5) is symmetric. This, in turn, implies that the derivative of $\langle \rho_{el} v \rangle$ is symmetric. Thus, by definition, $\langle \rho_{el} v \rangle$ is anti-symmetric.

As indicated in Figures 4.13 and 4.14, the maxima of $\langle \rho_{el} v \rangle$ are located at approximately $y/h = \mp 0.5$, *i.e.*, midway between the channel walls and the midplane. In particular, our simulations predict that the location of the peak and the shape of $\langle \rho_{el} v \rangle$ are independent of dimensionless quantities such as the Péclet number, the friction, and the electric Reynolds numbers. Also, according to Figure 4.13, the effect of the turbulence intensity of the flow on the value of $\langle \rho_{el} v \rangle$ is much less pronounced than for $\langle \rho_{el} u \rangle$: an increase of Re_τ results in a mild increase of the spanwise turbulent flux. Moreover, the influence of the electrical conductivity σ is stronger; see comparisons between Cases B2, B4, and A5 in Figure 4.14. Again, modifying the diffusion coefficient D has little impact; see Cases B1 and B3 in Figure 4.14.

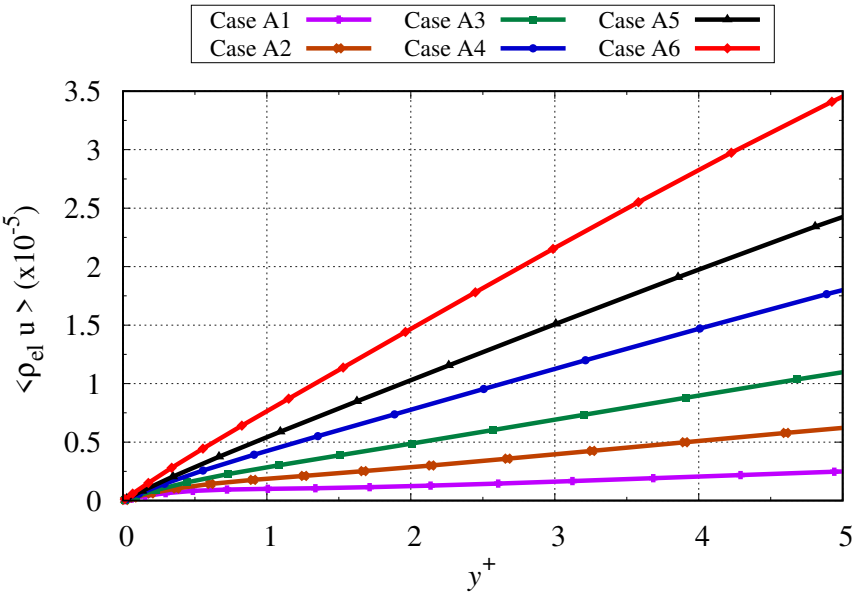

Figure 4.11: Profiles of $\langle \rho_{el} u \rangle$ inside the sublayer ($y^+ < 5$) for simulations of cases in Group A.

It is worth adding that the values of the spanwise turbulent flux $\langle \rho_{el} v \rangle$ are several orders smaller (10^4) than $\langle \rho_{el} u \rangle$. A possible explanation for this might be the aprroximation of $\langle \rho_{el} v \rangle$ by $\langle \rho_{el} \rangle \langle v \rangle = 0$. The purpose of this approximation is only to explain the difference in magnitude between $\langle \rho_{el} u \rangle$ and $\langle \rho_{el} v \rangle$. However, supposing that $\langle \rho_{el} v \rangle$ may be equal to zero leads to misconceptions about turbulent flow electrification. Indeed, on the basis of (4.5), a zero spanwise turbulent flux implies that the mean charge-density profile is the same as if the fluid was at rest, which contradicts the results obtained until now.

As illustrated by the plots of Figure 4.16, the root-mean-square (r.m.s) values of the electric charge density across the channel drop with increasing Re_τ. In other words, the fluctuations of ρ_{el} decrease with the turbulence intensity of the flow. As mentioned in section 4.2.1, as the turbulence intensity increases, the mixing of electric-charge carriers becomes more efficient, thereby reducing its fluctuations. The same trend is also observed in passively advected scalars in turbulent flows. For example, in free

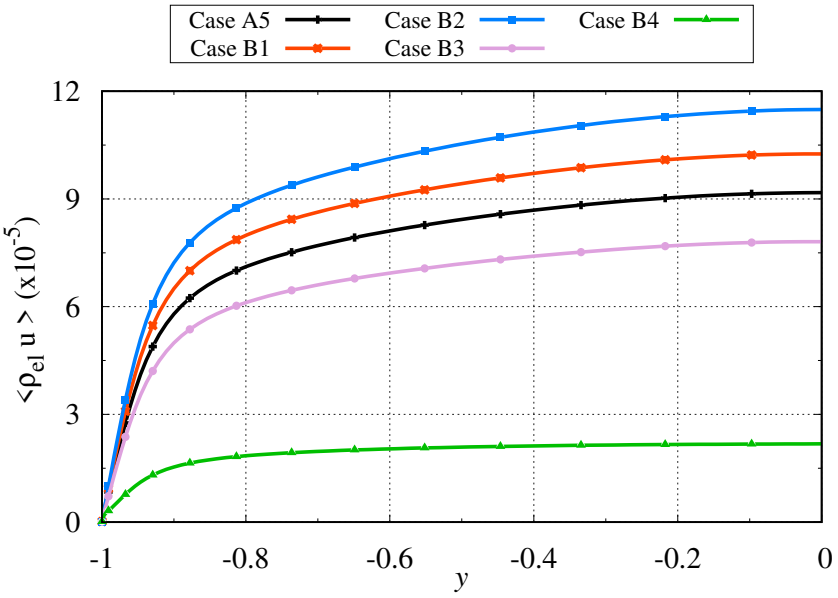

Figure 4.12: Profiles of $\langle \rho_{\mathrm{el}} u \rangle$ for simulations of cases in Group B.

convection, the r.m.s of the (normalized) temperature decreases as the turbulent flow becomes more intense [176, 177]. In summary, increasing the turbulence intensity results in higher and faster flow electrification and less fluctuating charge. Further, the location of the peak of the r.m.s values varies very slightly in terms of the friction Reynolds number, in contrast to the streamwise velocity u; see Figure 4.15. For instance, only two grid points separate the peak of $\rho_{\mathrm{el,rms}}$ between $Re_\tau = 80$ (A1) and $Re_\tau = 180$ (A5). On the contrary, there is a gap of eight grid points for the peak of u_{rms}; see Figure 4.15.

Additionally, the plots presented in Figure 4.17 indicate that the ohmic resistance has the opposite effect to the charge-density fluctuations. As the electrical conductivity σ increases (respectively, decreases), the r.m.s values of ρ_{el} across the channel increase (respectively, decrease). In other words, the ohmic resistance reduces the efficiency of turbulent mixing of ions in the liquid. Also, we point out from Figure 4.17 that the profiles of Cases B1, B3, and A5 are identical away from the wall. This, in turn, implies that the charge-diffusion process does not influence the fluctuations of

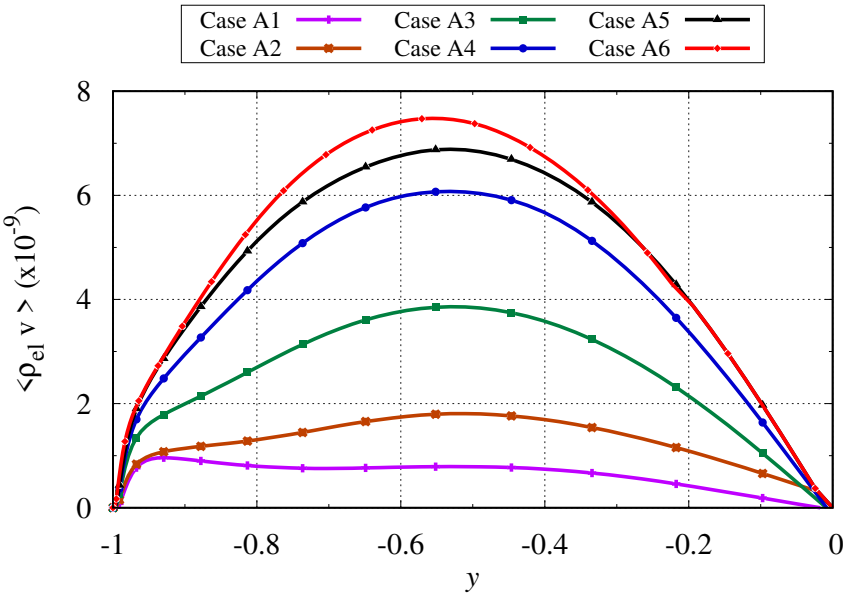

Figure 4.13: Profiles of the spanwise turbulent flux $\langle \rho_{\mathrm{el}} v \rangle$ for simulations of cases in Group A.

the electric charge density in this region. However, near the wall, the diffusive term appears to slightly modify the values of the r.m.s of the electric charge density. Most notably, the diffusion process shifts the location of the peak, in contrast to the electrical conductivity; see comparisons between Cases B1, B3 and A5 in the bottom of Figure 4.17.

4.3.2 Budget of the fluctuating charge-density variance

Below, we derive the fluctuating charge-density variance (FCV) equation. Further, we elaborate on the FCV budget during the statistically stationary stage. Then, we present numerical results of this budget for Cases A4 ($Re_\tau = 150$), A5 ($Re_\tau = 180$), B1 (increased diffusion), and B4 (increased conductivity). These four cases help assess the influence of the turbulence intensity, the diffusion coefficient, and the electrical conductivity on the FCV budget. In particular, to avoid redundancy, we assume that there is no need to provide a budget for the remaining six cases. The procedure for

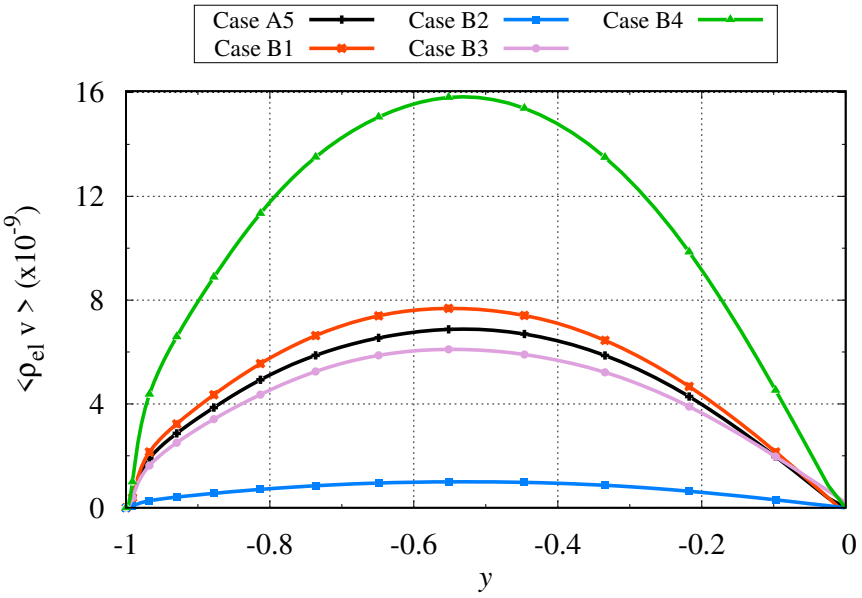

Figure 4.14: Profiles of the spanwise turbulent flux $\langle \rho_{\mathrm{el}} v \rangle$ for simulations of cases in Group B.

deriving the transport equation for $\langle k_{\mathrm{el}} \rangle$ is standard and consists of three steps. First, we multiply every term of (2.21) with ρ_{el} and then average the result,

$$\langle \boldsymbol{u} \cdot \boldsymbol{\nabla} \rho_{\mathrm{el}}^2 \rangle_{\mathrm{t}} \;=\; -\frac{2\sigma}{\epsilon} \langle \rho_{\mathrm{el}}^2 \rangle_{\mathrm{t}} + D \left(\nabla^2 \langle \rho_{\mathrm{el}}^2 \rangle_{\mathrm{t}} - 2 \langle \left(\frac{\partial \rho_{\mathrm{el}}}{\partial x_{\mathrm{j}}} \right)^2 \rangle_{\mathrm{t}} \right) . \tag{4.7}$$

In the second step, we take the average of (2.21) and multiply the result with $\langle \rho_{\mathrm{el}} \rangle_t$,

$$\langle \rho_{\mathrm{el}} \rangle_{\mathrm{t}} \langle \boldsymbol{u} \cdot \boldsymbol{\nabla} \rho_{\mathrm{el}} \rangle_{\mathrm{t}} \;=\; -\frac{2\sigma}{\epsilon} \langle \rho_{\mathrm{el}} \rangle_{\mathrm{t}}^2 + D \left(\nabla^2 \langle \rho_{\mathrm{el}} \rangle_{\mathrm{t}}^2 - 2 \left(\frac{\partial \langle \rho_{\mathrm{el}} \rangle_{\mathrm{t}}}{\partial x_{\mathrm{j}}} \right)^2 \right) . \tag{4.8}$$

Then, we subtract equation (4.7) from (4.8). Consequently, the FCV equation reads,

$$\underbrace{-\langle \boldsymbol{u} \rangle_t \cdot \nabla \langle k_{\mathrm{el}} \rangle_t}_{\mathscr{A}_{\mathrm{e}}} \underbrace{-\langle \rho_{\mathrm{el}}^{'} \boldsymbol{u}^{'} \rangle_t \cdot \nabla \langle \rho_{\mathrm{el}} \rangle_t}_{\mathscr{P}_{\mathrm{e}}} \underbrace{-\langle \boldsymbol{u}^{'} \cdot \nabla k_{\mathrm{el}} \rangle_t}_{\mathscr{T}_{\mathrm{e}}} + \underbrace{D \nabla^2 \langle k_{\mathrm{el}} \rangle_t}_{\mathscr{D}_{\mathrm{e}}}$$

$$\underbrace{-D \langle \nabla \rho_{\mathrm{el}}^{'} \cdot \nabla \rho_{\mathrm{el}}^{'} \rangle_t}_{\mathscr{E}_{\mathrm{e}}} \underbrace{-2 \frac{\sigma}{\epsilon} \langle k_{\mathrm{el}} \rangle_t}_{\mathscr{F}_{\mathrm{e}}} \;=\; 0 . \tag{4.9}$$

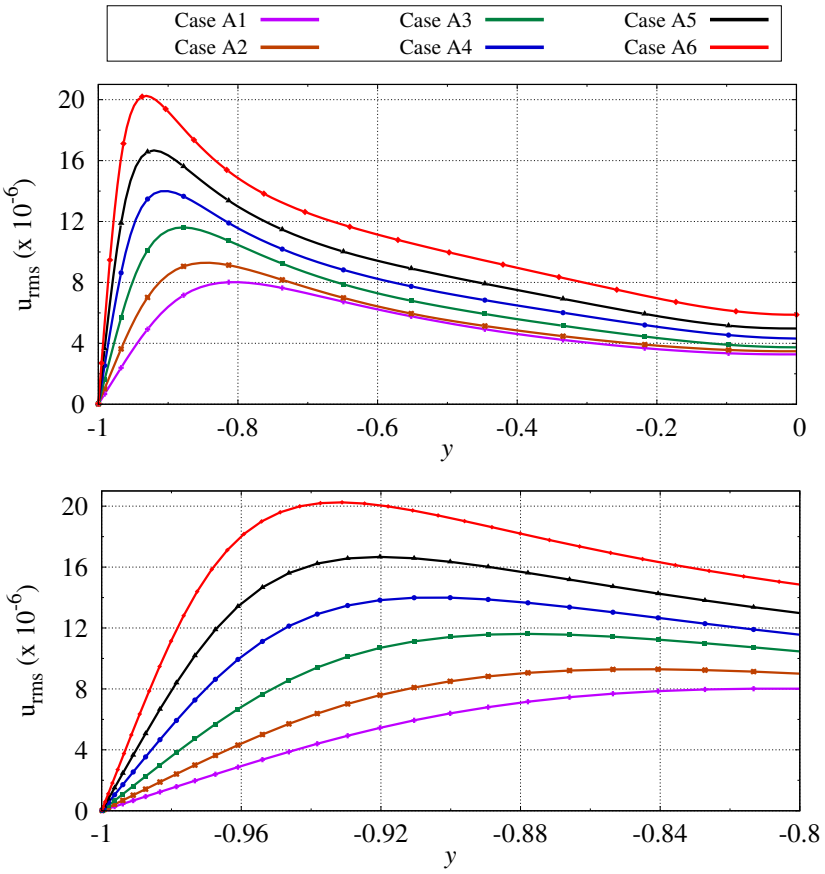

Figure 4.15: Root-mean-square profiles of the streamwise velocity u for the friction Reynolds numbers considered in our study. Top: profiles of u_{rms} across half of the channel. Bottom: zoom of the profiles in the near-wall region.

In the above equation, $\mathscr{A}_{\mathrm{e}}$, $\mathscr{P}_{\mathrm{e}}$, and $\mathscr{T}_{\mathrm{e}}$ describe the advection, production, and turbulent transport of the fluctuating charge-density variance. The terms $\mathscr{D}_{\mathrm{e}}$ and $\mathscr{E}_{\mathrm{e}}$ stand for molecular transport and dissipation. Finally, $\mathscr{F}_{\mathrm{e}}$ corresponds to a sink term for the FCV due to the ohmic resistance. In the case of a channel flow with periodic streamwise and spanwise directions, one can additionally perform area averaging. In this manner, the advection term $\mathscr{A}_{\mathrm{e}}$ vanishes and the budget equation (4.9) assumes the following

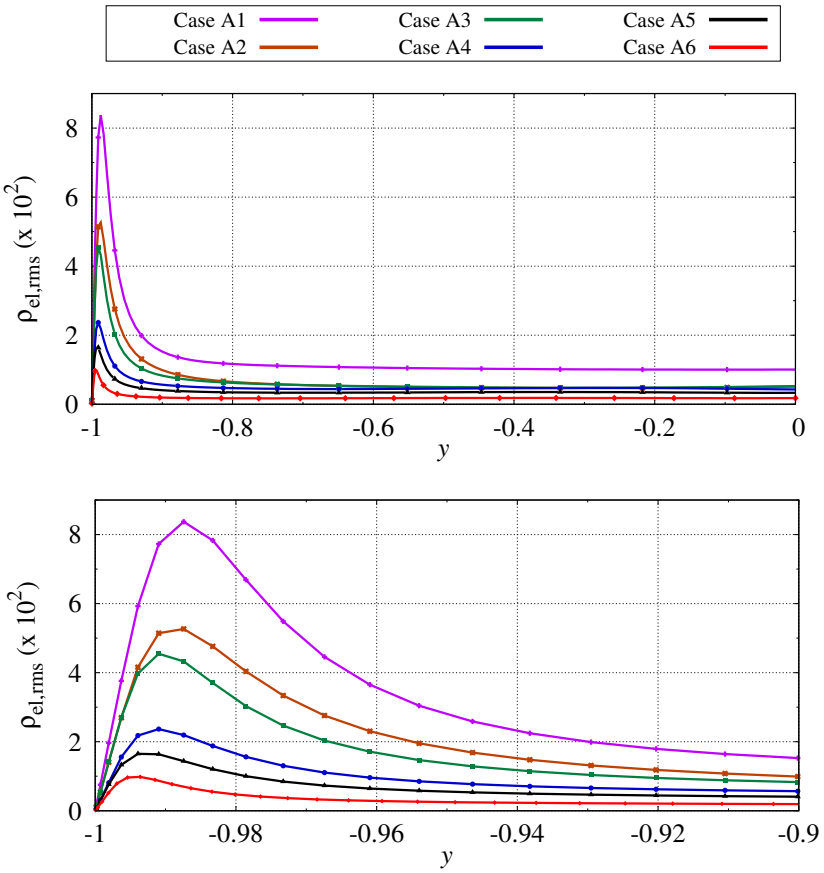

Figure 4.16: Root-mean-square profiles of the electric charge density ρ_{el} for simulations of cases in Group A. Top: profiles of $\rho_{el,rms}$ across half of the channel. Bottom: zoom of the profiles in the near-wall region.

simplified form,

$$\underbrace{-\langle \rho_{el}' v' \rangle \frac{d}{dy}\langle \rho_{el} \rangle}_{\mathscr{P}_e} \underbrace{-\frac{d}{dy}\langle v' k_{el} \rangle}_{\mathscr{T}_e} + \underbrace{D\frac{d^2}{dy^2}\langle k_{el} \rangle}_{\mathscr{D}_e} \underbrace{-D\langle \nabla \rho_{el}' \cdot \nabla \rho_{el}' \rangle}_{\mathscr{E}_e}$$
$$\underbrace{-2\frac{\sigma}{\epsilon}\langle k_{el} \rangle}_{\mathscr{F}_e} = 0. \tag{4.10}$$

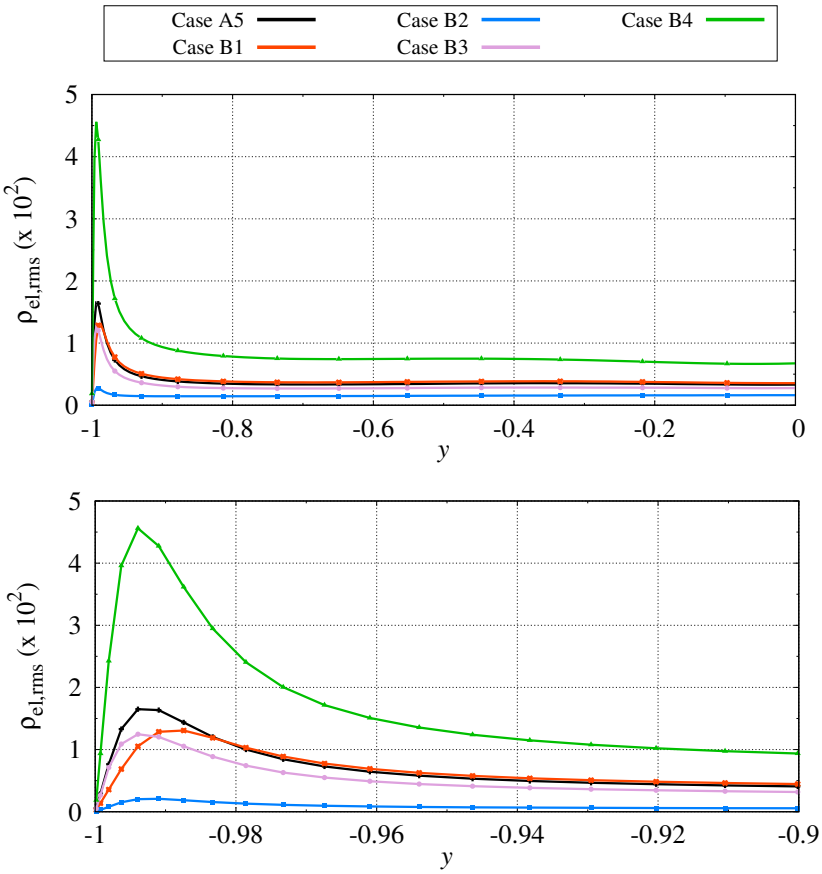

Figure 4.17: Root-mean square profiles of the electric charge density ρ_{el} for simulations of cases in Group B. Top: profiles of $\rho_{el,rms}$ across half of the channel. Bottom: zoom of the profiles in the near-wall region.

One can perform a similar procedure concerning the derivation of the (area-averaged) turbulent kinetic energy equation; see, for example, [168]. Accordingly, the area-

averaged TKE equation reads,

$$\underbrace{-\langle u_{\mathrm{i}}' v' \rangle \frac{\mathrm{d}}{\mathrm{d}y}\langle u_{\mathrm{i}} \rangle}_{\mathscr{P}} \underbrace{-\frac{1}{2}\langle \frac{\partial}{\partial x_{\mathrm{i}}} u_{\mathrm{j}}' u_{\mathrm{j}}' u_{\mathrm{i}}' \rangle}_{\mathscr{T}} + \underbrace{\nu \frac{\mathrm{d}^2}{\mathrm{d}y^2} k}_{\mathscr{D}} \underbrace{-\nu \langle \nabla u_{\mathrm{i}}' \cdot \nabla u_{\mathrm{i}}' \rangle}_{\mathscr{E}}$$
$$\underbrace{-\frac{1}{\rho}\langle \frac{\partial u_{\mathrm{i}}' p'}{\partial x_{\mathrm{i}}} \rangle}_{\mathscr{C}} = 0 \,, \tag{4.11}$$

where $\mathscr{C}$ represents the pressure diffusion. Please note that we do not incorporate the term associated with the volumetric electric force. Since this force does not affect the motion of the fluid (*cf.* section 2.2.2), the term associated with the TKE equation equals zero and is then assumed negligible, as predicted by our simulations.

In the analysis of the FCV budget, the various terms of (4.9) were area-averaged (along the periodic x and z directions) and time-averaged during the statistically stationary stage of the electrification process. In each simulation, the period of averaging $\overline{T}$ lasted more than 80 flow-through times, where a flow-through time is equal to $4\pi h/u_{\mathrm{m}}$. Hence, we have,

$$\overline{T} \geq \frac{10^3 h}{u_{\mathrm{m}}} \,. \tag{4.12}$$

In this manner, the sum of the terms on the left-hand side of (4.10) was smaller than 1% of the amplitude of the largest term, which is deemed sufficiently close to zero for this study.

We present respectively in Figures 4.18 and 4.19 the budget terms of the FCV equation for Cases A4 ($Re_\tau = 150$) and A5 ($Re_\tau = 180$). According to these plots, adjacent to the wall, the molecular transport $\mathscr{D}_{\mathrm{e}}$ is counter-balanced by the dissipation term $\mathscr{E}_{\mathrm{e}}$, while all other terms practically vanish. In the near-wall regions ($-0.99h < |y| <$ 0.95h), production $\mathscr{P}_{\mathrm{e}}$ and turbulent transport $\mathscr{T}_{\mathrm{e}}$ are dominant and balance out one another; *cf.* bottom of Figures 4.18 and 4.19. The peaks of these terms are located closed to the wall, corresponding to $|y| \approx 0.988h$. Away from the location of these peaks, both $\mathscr{P}_{\mathrm{e}}$ and $\mathscr{T}_{\mathrm{e}}$ decrease substantially in amplitude but are still the dominant terms in the FCV budget. Away from the wall, all terms have a small amplitude. Nonetheless, $\mathscr{P}_{\mathrm{e}}$ and $\mathscr{T}_{\mathrm{e}}$ are still the largest terms and compensate each other out. Also, it is worth pointing out that the amplitude of $\mathscr{F}_{\mathrm{e}}$, related to the ohmic resistance, appears negligible compared to all other terms across the channel. Globally, a comparison between

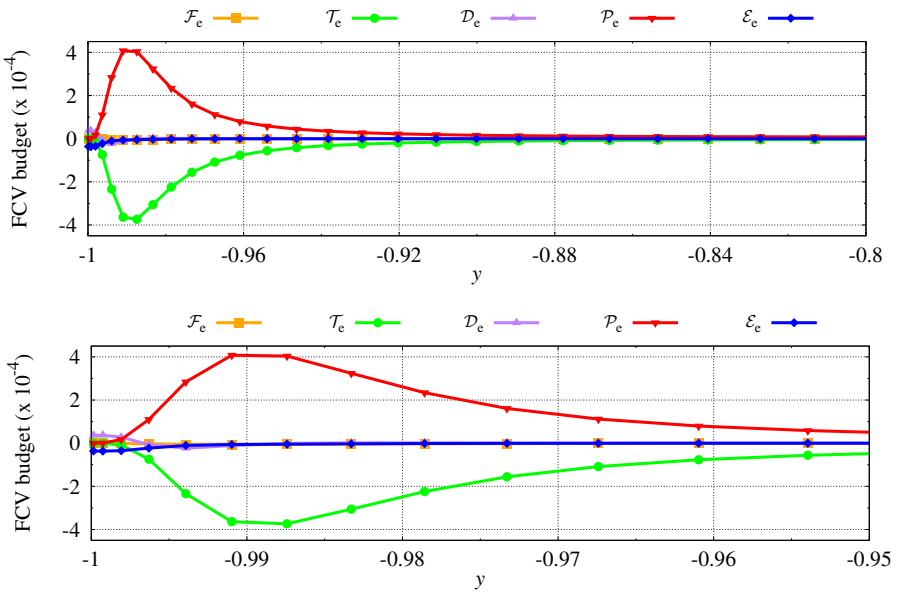

Figure 4.18: Profiles of the area-averaged terms in the fluctuating charge variance (FCV) budget. Top: budget of the FCV for Case A4 ($Re_\tau = 150$). Bottom: zoom of the profiles in the near-wall region.

Figures 4.18 and 4.19 indicates that the values of all the terms in the FCV budget decrease as the turbulence intensity of the flow increases. In other words, the fluctuations of the electric charge density are reduced when Re_τ increases, as predicted in section 4.3.1 via the r.m.s profiles of ρ_{el}. As a matter of fact, according to our simulations, this is the only noticeable difference. Therefore, the influence that the turbulence intensity of the flow has on the terms in the FCV budget is radically different to that on the terms in the TKE budget. For visualization purposes, we have plotted in Figure 4.20 the area-averaged terms in the TKE budget for $Re_\tau = 150$ (A4) and $Re_\tau = 180$ (A5). Please note that similar analyses on the TKE have been performed extensively in the past and are available in standard textbooks; see, for example, [168]. By virtue of the plots presented in Figures 4.18, 4.19, and 4.20, we note the following.

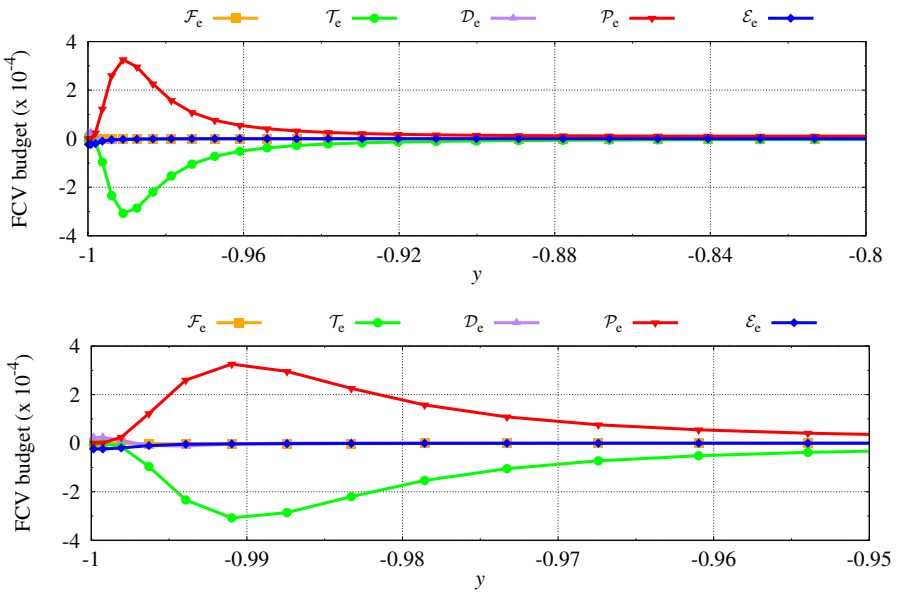

Figure 4.19: Profiles of the area-averaged terms in the fluctuating charge variance (FCV) budget. Top: budget of the FCV for Case A5 ($Re_\tau = 180$). Bottom: zoom of the profiles in the near-wall region.

- The values of the terms in the FCV budget are several orders of magnitude smaller than the terms in the TKE budget. Moreover, in the FCV budget, these values decrease with Re_τ; whereas they increase in the TKE budget.
- In the FCV budget, the dissipation term $\mathscr{E}_e$ is non-negligible only at the wall. On the contrary, the dissipation term $\mathscr{E}$ in the TKE budget counter-balances the production term $\mathscr{P}$ away from the wall.
- The terms in the FCV budget vanish at a distance Δ from the wall far closer to those in the TKE budget: $\Delta \approx 0.2h$ in the TKE budget. Whereas, it corresponds to $\Delta \approx 0.05h$ in the FCV budget.

The aforementioned second point has major consequences concerning the presence of microscales in the electric charge density. According to Tennekes and Lunley [169],

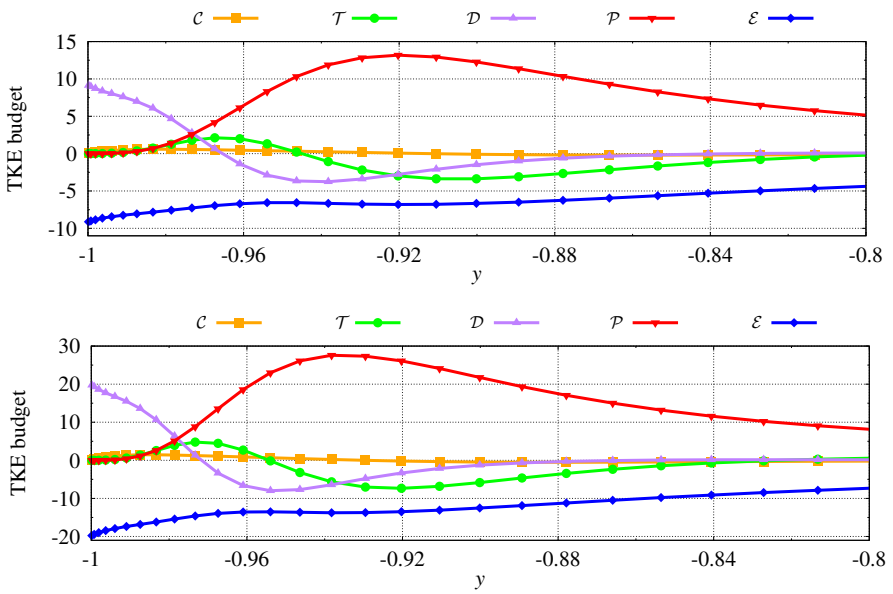

Figure 4.20: Profiles of the area-averaged terms in the turbulent kinetic energy (TKE) budget. Top: budget of the TKE for Case A4 ($Re_\tau = 150$). Bottom: budget of the TKE for Case A5 ($Re_\tau = 180$).

the Taylor microscale λ_ψ of a generic passive scalar ψ is defined by,

$$\langle \left(\frac{\partial \psi'}{\partial x_j} \right)^2 \rangle = 2 \frac{\langle \left(\psi' \right)^2 \rangle}{\lambda_\psi^2} \,. \tag{4.13}$$

As suggested by Tennekes and Lunley [169], the estimation of λ_ψ is based on the equality between the production term and the dissipation term of the corresponding governing equation for the passive-scalar fluctuations (such as temperature). However, for the problem of interest, the production term $\mathscr{E}_e$ of (4.10) essentially compensates the turbulent transport $\mathscr{T}_e$, not the dissipation term; see Figures 4.18 and 4.19. In particular, we have,

$$\langle \rho_{el}' v' \rangle \frac{d}{dy} \langle \rho_{el} \rangle \;\approx\; -\frac{1}{2} \frac{d}{dy} \langle v' \rho_{el}' \rho_{el}' \rangle \,. \tag{4.14}$$

This equation implies that the introduction of a corresponding Taylor microscale for the electric charge density may not be feasible.

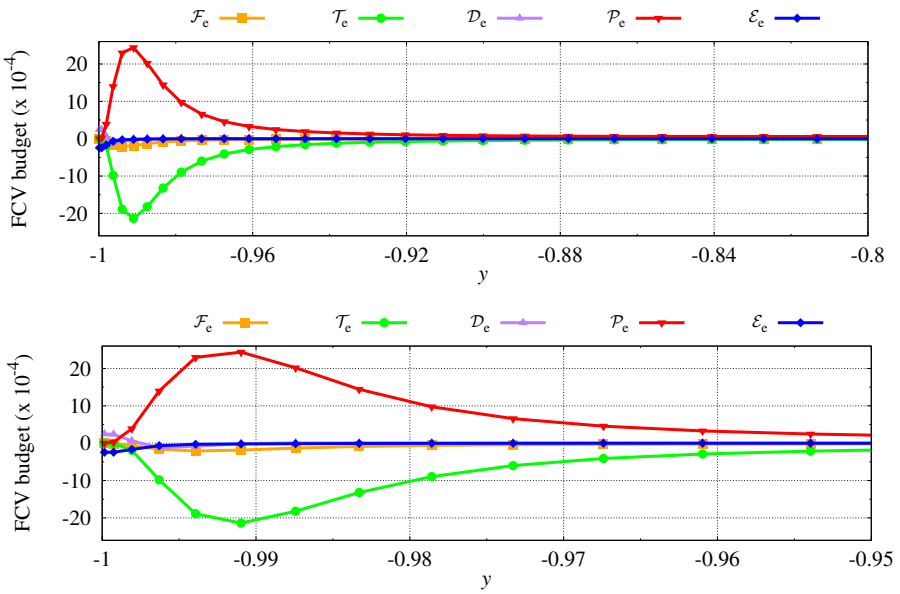

Figure 4.21: Profiles of the area-averaged terms in the fluctuating charge variance (FCV) budget. Top: budget of the FCV for Case B4 (σ increased). Bottom: zoom of the profiles in the near-wall region.

Additionally, for a given Reynolds number ($Re_\tau = 180$), our simulations indicate that each term of the FCV equation increases (respectively, decreases) in terms of the electrical conductivity. More specifically, the fluctuations of ρ_{el} increase with respect to σ, as highlighted in section 4.3.1. As a result, at higher values of σ, the influence of the sink term $\mathcal{F}_e$ cannot be considered negligible anymore, especially close to the wall, namely $0.98h < |y| < h$; see Figure 4.21. Further, we readily infer that the location of the peak (attributed to the production) is not modified by the electrical conductivity, in contrast to the diffusion coefficient. In fact, as indicated in Figure 4.22, an increase of D (Case B1) results in higher values for the dissipation and molecular transport in the near-wall regions, which corresponds to the zone of influence of the diffusive term.

Please note that the main features concerning the FCV budget, *i.e.*, the location of the peak and the magnitude of each term, are in excellent agreement with regards to the findings presented in section 4.3.1.

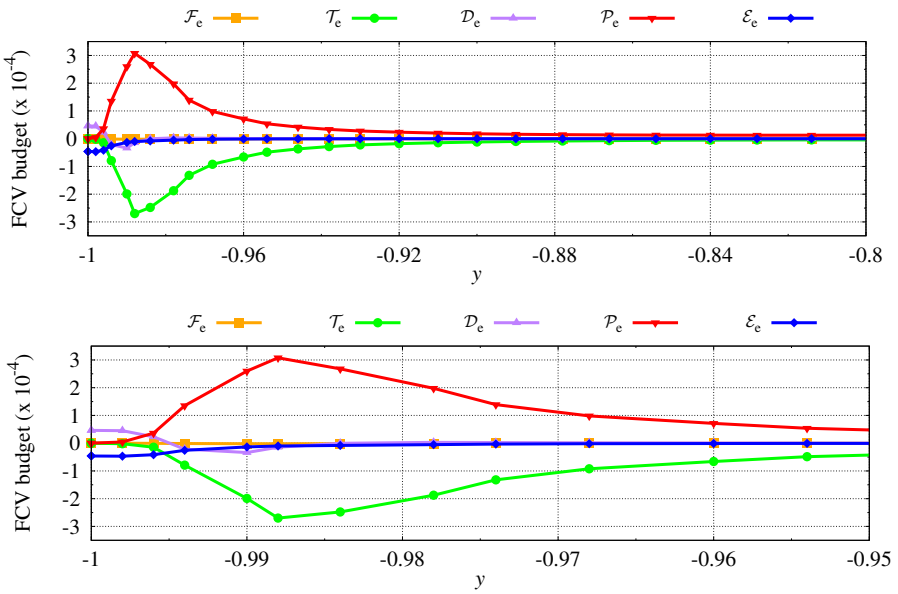

Figure 4.22: Profiles of the area-averaged terms in the fluctuating charge variance (FCV) budget. Top: budget of the FCV for Case B1 (D increased). Bottom: zoom of the profiles in the near-wall region.

4.4 Mean charge-density profile

In this section, we consider the mean charge-density equation (4.5) and derive an approximate solution of it that is close to our numerical predictions. The primary purpose of derivating closed-form expressions for the mean charge-density profiles is to provide insight into potential scaling laws for the problem in hand. It also helps for the development of turbulence models in the context of Reynolds-Averaged Navier-Stokes (RANS) and Large Eddy Simulations (LES); *cf.* Chapter 5. The mean charge-density profile for flows in circular pipes has been studied before by Abedian and Sonin [61], and earlier studies [178–180]. Herein we perform an analogous analysis in channel flows. The basic idea behind the derivation of a closed-form solution for the mean charge-density is to replace the product $\langle \rho'_{\mathrm{el}} v' \rangle$ (or, equivalently, $\langle \rho_{\mathrm{el}} v \rangle$) in (4.5) by a gradient term so that the left-hand side becomes a linear elliptic operator. In the context of turbulence modeling, this is referred to as the gradient assumption; see, for example,

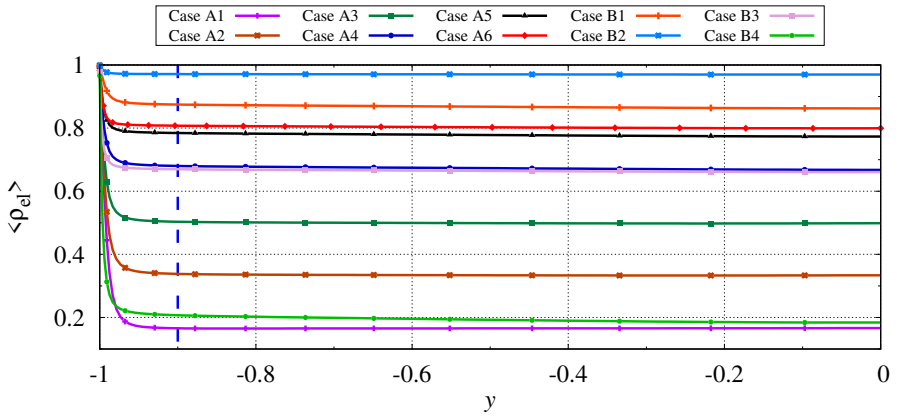

Figure 4.23: Profiles of the mean charge density $\langle \rho_{el} \rangle$ for the DNS considered herein. Globally, three distinct zones can be discerned. The vertical dashed line marks, approximately, the end of the second zone and the start of the third one.

[181]. Let D_t denote the *turbulent eddy diffusivity* of the electric charge density. Then, the spanwise turbulent flux $\langle \rho'_{el} v' \rangle$ is approximated as,

$$\langle \rho'_{el} v' \rangle \approx -D_t \frac{d}{dy} \langle \rho_{el} \rangle . \tag{4.15}$$

By introducing (4.15) into (4.5), we obtain,

$$-\frac{\sigma}{\epsilon} \langle \rho_{el} \rangle + \frac{d}{dy} \left((D + D_t) \frac{d}{dy} \langle \rho_{el} \rangle \right) = 0 . \tag{4.16}$$

As explained in section 1.2.4, the eddy diffusivity operates as an additional diffusion process to account for the loss of turbulent effects when averaging. To determine a closed-form solution of (4.16), D_t must be approximated. To this end, we propose below to evaluate the turbulent eddy diffusivity in two different manners. In the first model, we draw on the procedure of Abedian and Sonin [61] for our specific case of turbulent channel flows. On the other hand, the second model make use of our numerical results concerning the spanwise turbulent flux $\langle \rho'_{el} v' \rangle$ and the production term $\mathscr{P}_e$ of the FCV equation (4.10).

4.4.1 First model: separation of D_t into three zones

Abedian and Sonin [61] proposed a simplified expression for the turbulent eddy diffusivity. It consists of the separation of D_t into three zones. Inside the first zone, D_t is much smaller than the diffusion coefficient D. As a result, the turbulent eddy diffusivity is approximated by zero. In the second zone, D_t increases linearly with the distance from the wall and the friction velocity. Finally, in the third zone, D_t is equal to a constant, the value of which is determined by requiring that the resulting mean charge-density profile be continuous. Although this model is simplistic, it is reasonable to try to apply it for the problem in hand. Indeed, on the basis of the shapes of the predicted profiles for the mean charge density, we can distinguish three different zones of charge distribution; *cf.* Figure 4.23. We describe below these three zones.

Zone I: effective diffusion sublayer ($h - \delta \leq |y| \leq h$)

The first zone is the effective diffusion sublayer, which has been identified in section 3.4.3 when investigating the charge-density distribution in the diffuse layer (in turbulent channel flows). In the present study, its thickness is denoted by δ. By definition, this zone is adjacent to the wall and inside both the viscous sublayer and the diffuse layer (*i.e.*, $\delta < \gamma$). Inside this zone, ions are only transported via diffusion, which implies that the turbulent eddy diffusivity D_t is negligible with regards to D. Therefore, in this zone, the profile of the mean charge density is similar to that for a fluid at rest, as observed in section 3.4.3. More specifically, we have,

$$\langle \rho_{el} \rangle (y) \;=\; \rho_w \frac{\sinh\left(\frac{h-y}{\lambda_D}\right) + \sinh\left(\frac{h+y}{\lambda_D}\right)}{\sinh\left(\frac{2h}{\lambda_D}\right)} \;, \quad \text{for} \;\; h - \delta \leq |y| \leq h \;. \tag{4.17}$$

To estimate numerically the thickness of the effective diffusion sublayer, we have plotted in Figures 4.24 and 4.25 the charge-density distribution for a fully perturbed diffuse layer and for a liquid at rest (*i.e.*, when $\langle \rho_{el} \rangle$ is determined by the expression (4.17)), for simulations of cases in Groups A and B, respectively. According to Figure 4.24 and as predicted in section 3.4.3, δ decreases as Re_τ increases. In particular, for $Re_\tau \geq 150$ (Cases A4, A5, and A6), the effective diffusion sublayer is located between the wall and the first grid point; *cf.* Figure 4.24. Therefore, the thickness of this zone is exceedingly thin. Also, from the plots of Figure 4.25, it is expected that δ increases with

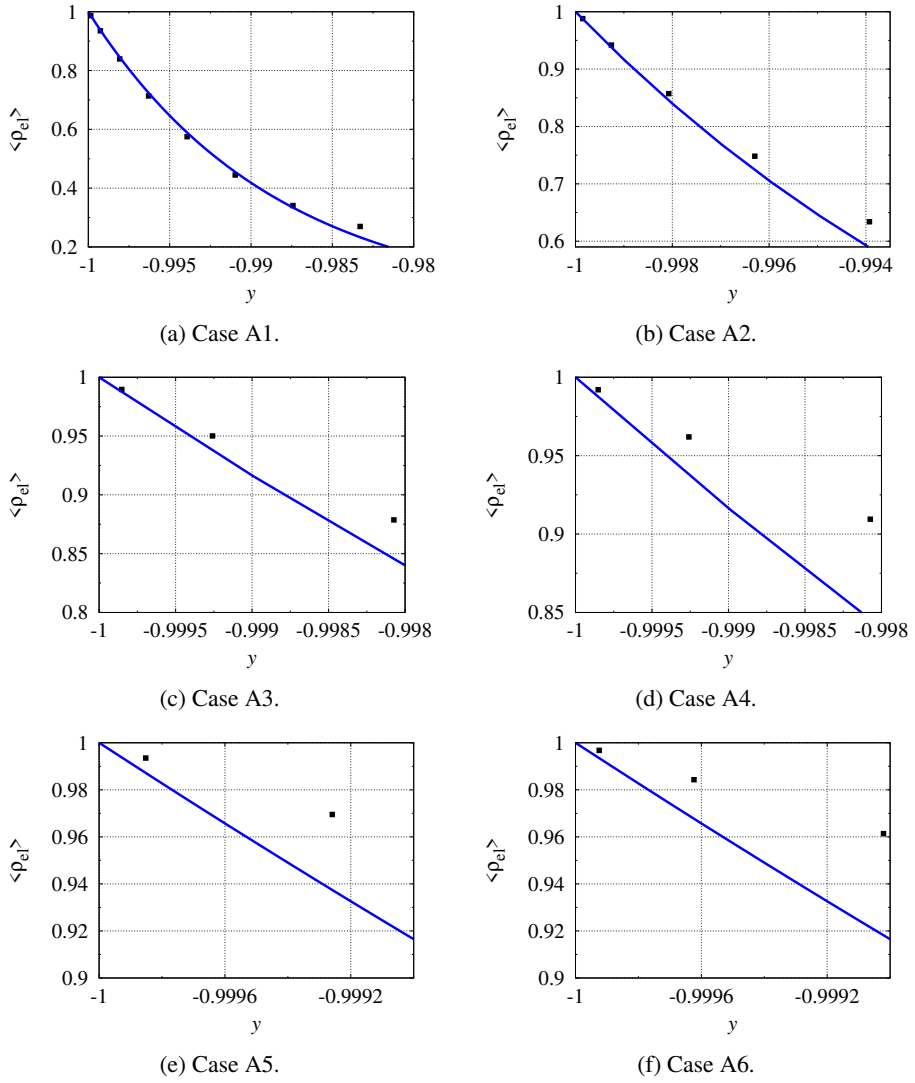

(a) Case A1. (b) Case A2.

(c) Case A3. (d) Case A4.

(e) Case A5. (f) Case A6.

Figure 4.24: Plots of the mean charge density $\langle \rho_{el} \rangle$ in the near-wall zone. The black squares "■" denote the charge-density distribution for a fully perturbed diffuse layer, computed via DNS of the six cases of Group A. Whereas, the blue line represents the initial charge-density distribution.

D and with σ. These results are in excellent agreement with our previous observations: inside the effective diffusion sublayer, the transport of charge is due to diffusion.

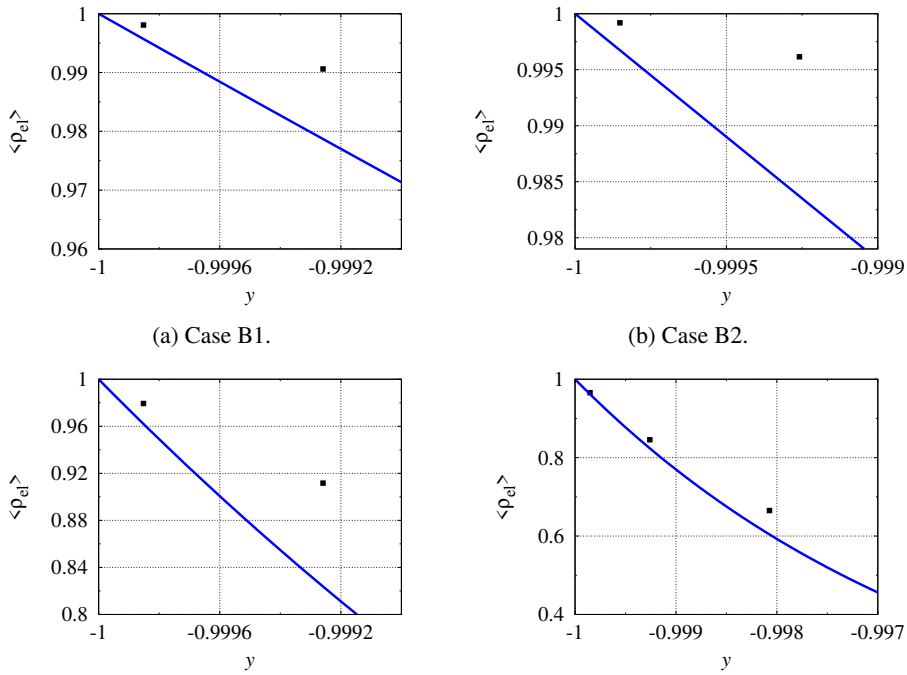

(a) Case B1. (b) Case B2.

(c) Case B3. (d) Case B4.

Figure 4.25: Plots of the mean charge density $\langle \rho_{el} \rangle$ in the near-wall zone. The black squares "■" denote the charge-density distribution for a fully perturbed diffuse layer, computed via DNS of the four cases of Group B. Whereas, the blue line represents the initial charge-density distribution.

However, at higher turbulence intensities, the convective transport of charge becomes more and more efficient, thus reducing the zone of influence of the diffusive term, *i.e.*, reducing δ. Also, when increasing σ, the efficiency of the turbulent mixing is reduced, thereby resulting in an increase of δ.

Zone II: transition zone ($0.9h \leq |y| \leq h - \delta$)

In the second zone, hereinafter referred to as the *transition zone*, the convective transport of charge becomes important since turbulent eddies displace electric-charge carriers away from the diffuse layer and towards the bulk of the channel. Therefore, the competing mechanisms in this zone are the convective and conductive currents. By

virtue of Figure 4.23, we infer that inside this zone, the mean electric charge density decreases away from the walls but at a lower rate than in the effective diffusion sublayer (first zone). In the cases examined herein, the transition zone terminates approximately at 0.1 unit length from the wall, namely $|y| \approx 0.9h$. This location corresponds to the moment in which the root-mean-square values of the electric charge density are almost constant and minimal; *cf.* Figures 4.16 and 4.17. It also corresponds to the moment for which the budget terms of the FCV vanish; see Figures 4.18-4.21. As assumed by Abedian and Sonin [61], we consider that inside this zone, D_t increases linearly with respect to the distance from the wall. Thus, the solution of (4.16) is given in terms of modified Bessel functions and reads, for $0.9h \leq |y| \leq h - \delta$,

$$\langle \rho_\mathrm{el} \rangle \, (y) \;=\; C_1 I_0 \left(2\sqrt{\frac{\sigma}{\epsilon\kappa}(h - |y|)} \right) + C_2 K_0 \left(2\sqrt{\frac{\sigma}{\epsilon\kappa}(h - |y|)} \right) \;, \tag{4.18}$$

where I_0 and K_0 denote the zeroth-order modified Bessel functions of the first and second kind, respectively. Also, κ is a quantity that has dimensions of velocity and corresponds to the proportionality coefficient for the turbulent eddy diffusivity, *i.e.*,

$$D_\mathrm{t} \;=\; \kappa \; (h - |y|) \;. \tag{4.19}$$

Abedian and Sonin [61] obtained a value of $\kappa = 0.4u_\tau$. In accordance with those authors, our simulations suggest that κ must depend on the friction velocity. However, for the specific case of channel flows, κ is approximated by $\kappa = 4u_\tau$. Then, the eddy diffusivity reads, for $0.9h \leq |y| \leq h - \delta$,

$$D_\mathrm{t} \;=\; 4u_\tau \; (h - |y|) \;. \tag{4.20}$$

Finally, the terms C_1 and C_2 of (4.18) are integration constants. More specifically, the values of C_1 and C_2 are determined via the following boundary conditions,

$$\langle \rho_\mathrm{el} \rangle \big|_{\pm(h-\delta)} \;=\; C_1 I_0 \left(2\sqrt{\frac{\sigma}{\epsilon\kappa}\delta} \right) + C_2 K_0 \left(2\sqrt{\frac{\sigma}{\epsilon\kappa}\delta} \right) \;, \tag{4.21}$$

$$\langle \rho_\mathrm{el} \rangle \big|_{\pm 0.9h} \;=\; C_1 I_0 \left(2\sqrt{\frac{\sigma}{10\epsilon\kappa}} \right) + C_2 K_0 \left(2\sqrt{\frac{\sigma}{10\epsilon\kappa}\delta} \right) \;. \tag{4.22}$$

Then, C_1 and C_2 read,

$$C_1 = \frac{\langle\rho_{\mathrm{el}}\rangle\big|_{\pm(h-\delta)} K_0\left(2\sqrt{\frac{\sigma}{10\epsilon\kappa}}\delta\right) - \langle\rho_{\mathrm{el}}\rangle\big|_{\pm 0.9h} K_0\left(2\sqrt{\frac{\sigma}{\epsilon\kappa}}\delta\right)}{I_0\left(2\sqrt{\frac{\sigma}{\epsilon\kappa}}\delta\right) K_0\left(2\sqrt{\frac{\sigma}{10\epsilon\kappa}}\delta\right) - I_0\left(2\sqrt{\frac{\sigma}{10\epsilon\kappa}}\right) K_0\left(2\sqrt{\frac{\sigma}{\epsilon\kappa}}\delta\right)},$$

$$C_2 = \frac{\langle\rho_{\mathrm{el}}\rangle\big|_{\pm(h-\delta)} I_0\left(2\sqrt{\frac{\sigma}{10\epsilon\kappa}}\delta\right) - \langle\rho_{\mathrm{el}}\rangle\big|_{\pm 0.9h} I_0\left(2\sqrt{\frac{\sigma}{\epsilon\kappa}}\delta\right)}{I_0\left(2\sqrt{\frac{\sigma}{10\epsilon\kappa}}\right) K_0\left(2\sqrt{\frac{\sigma}{\epsilon\kappa}}\delta\right) - I_0\left(2\sqrt{\frac{\sigma}{\epsilon\kappa}}\delta\right) K_0\left(2\sqrt{\frac{\sigma}{10\epsilon\kappa}}\delta\right)}.$$

Zone III: core zone ($0 \leq |y| \leq 0.9h$)

The third zone, hereinafter referred to as the *core zone*, is characterized by a very slow decrease of the electric charge density away from the walls. Therein, $\langle\rho_{\mathrm{el}}\rangle$ and the degree of electrification increases considerably with the turbulence intensity of the flow, as described in section 4.2.3. In this zone, as assumed by Abedian and Sonin [61], we consider the eddy diffusivity to be uniform, hence constant. To ensure a continuous profile for the mean charge density, the value of this constant equals the value of D_{t} at the boundary of the transition zone, *i.e.*,

$$D_{\mathrm{t}} = \frac{2u_\tau h}{5}. \tag{4.23}$$

Next, the solution of (4.16) in the core zone is given by an analogous relation to that in the effective diffusion sublayer. It reads, for $0 \leq |y| \leq 0.9h$,

$$\langle\rho_{\mathrm{el}}\rangle(y) = \frac{\langle\rho_{\mathrm{el}}\rangle\big|_{0.9h} \sinh\left(\frac{|y|}{\tilde{\lambda}}\right) + \langle\rho_{\mathrm{el}}\rangle\big|_{0} \sinh\left(\frac{0.9h-|y|}{\tilde{\lambda}}\right)}{\sinh\left(\frac{0.9h}{\tilde{\lambda}}\right)}, \tag{4.24}$$

where $\tilde{\lambda}$ is a modified Debye length which reads,

$$\tilde{\lambda} := \sqrt{\frac{\epsilon D_{\mathrm{t}}}{\sigma}} = \sqrt{\frac{2\epsilon u_\tau}{5\sigma}}. \tag{4.25}$$

Please note that we do not take into account the diffusion coefficient D in the definition (4.25) of the modified Debye length. As discussed above, in this zone, its influence is

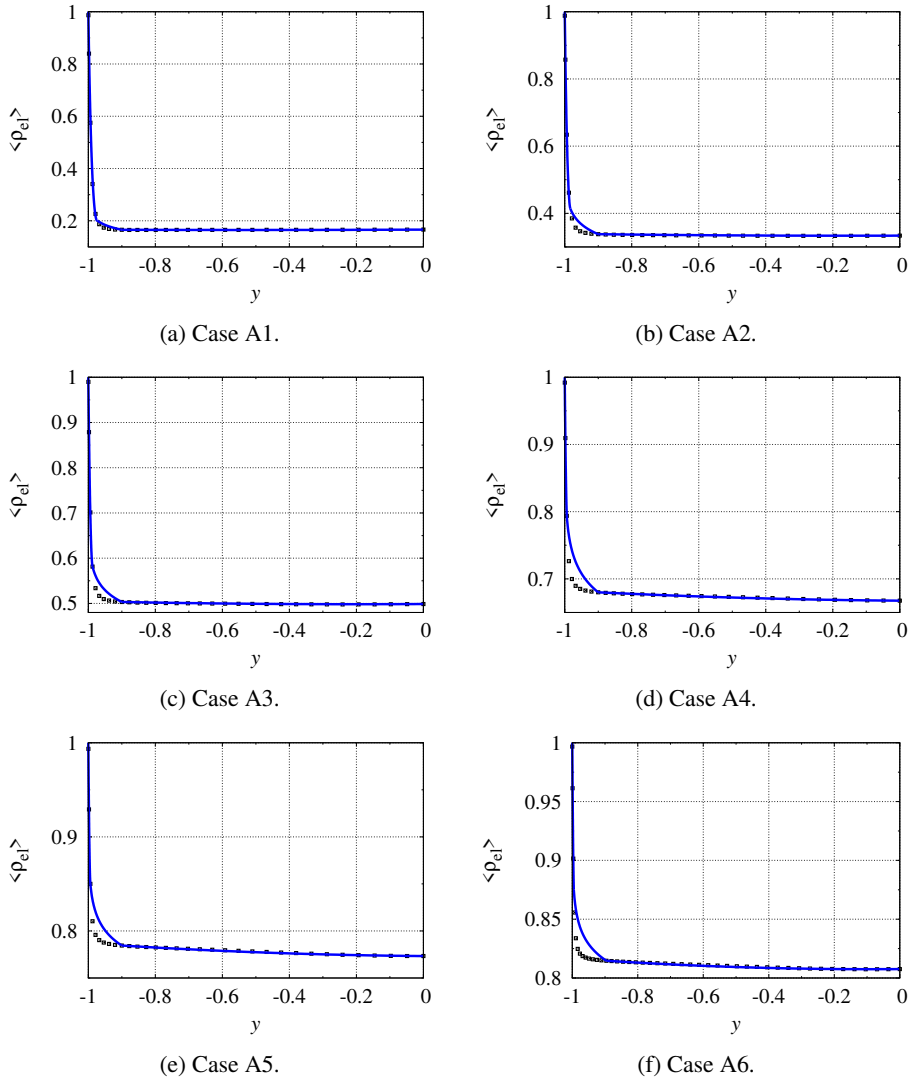

(a) Case A1.

(b) Case A2.

(c) Case A3.

(d) Case A4.

(e) Case A5.

(f) Case A6.

Figure 4.26: Plots of the mean charge density $\langle \rho_{el} \rangle$ along the y axis. The blue line denotes the profiles obtained via DNS of the six cases of Group A. Whereas, the black squares "■" represent the closed-form solution of (4.5).

assumed to be negligible. Indeed, by virtue of (4.23), D is several orders of magnitude smaller than the turbulent eddy diffusivity. For the simulations considered throughout this thesis, the ratio D_t/D varies between 3.1×10^4 (Case B1) and 2.5×10^6 (Case B3).

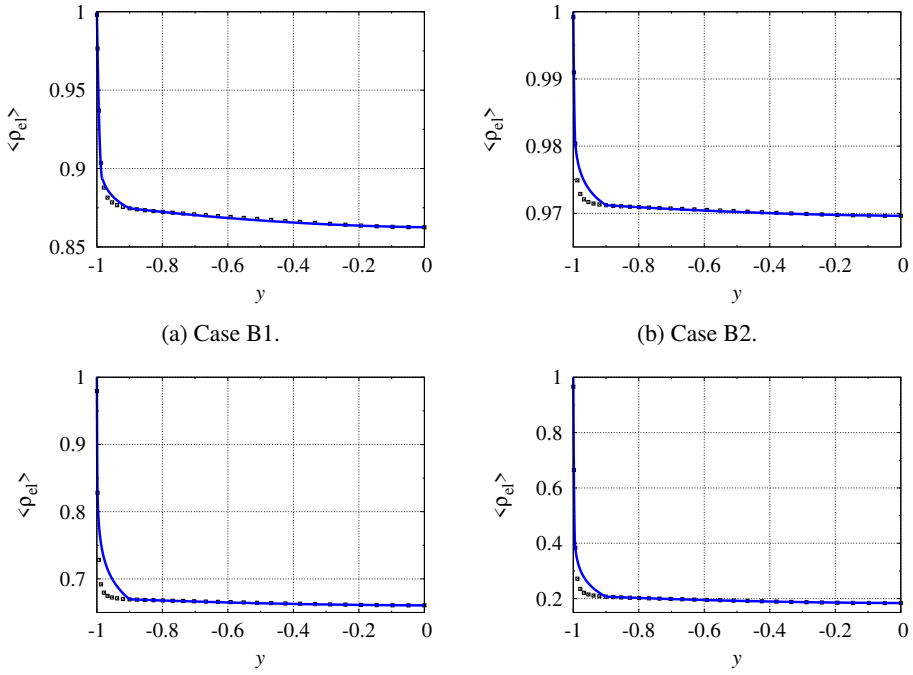

(a) Case B1. (b) Case B2.

(c) Case B3. (d) Case B4.

Figure 4.27: Plots of the mean charge density $\langle \rho_{\mathrm{el}} \rangle$ along the y axis. The blue line denotes the profiles obtained via DNS of the four cases of Group B. Whereas, the black squares "■" represent the closed-form solution of (4.5).

To summarize, the turbulent eddy diffusivity has the following parametrization,

$$D_{\mathrm{t}} = \begin{cases} << D & \text{for} \quad h - \delta < |y| < h, \\ 4u_{\tau}\ (h - |y|) & \text{for} \quad 0.9h < |y| < h - \delta\ , \\ \dfrac{2u_{\tau}h}{5} & \text{for} \quad 0 \leq |y| \leq 0.9h\ . \end{cases} \tag{4.26}$$

Accordingly, we present in Figures 4.26 and 4.27 plots of the closed-form profiles of $\langle \rho_{\mathrm{el}} \rangle$, obtained from (4.16) and (4.26), for simulations of cases in Groups A and B, respectively. These plots are juxtaposed with the corresponding results of our DNS. We observe that the closed-form approximate solution agrees reasonably well with the numerical results in the first and third zones. On the other hand, it slightly overestimates

the numerical results in the second zone (transition region), which can be attributed to the errors in the presumed simplified form (4.26) of D_t.

4.4.2 Second model: numerical estimation of D_T

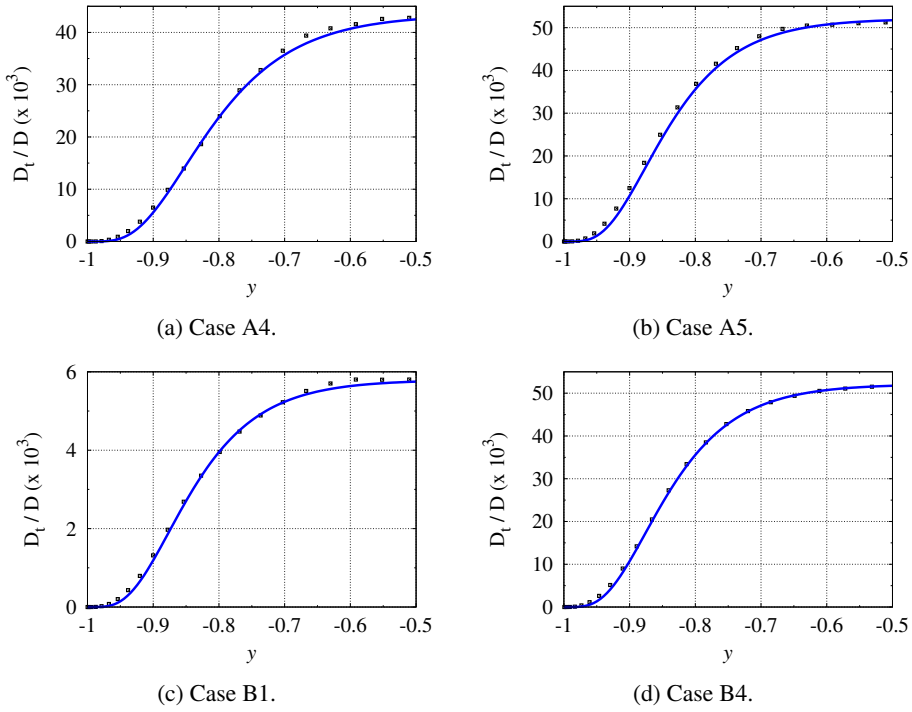

(a) Case A4.

(b) Case A5.

(c) Case B1.

(d) Case B4.

Figure 4.28: Plots of the turbulent eddy diffusivity D_T (normalized by D) between $y = -h$ and $y = -0.5h$. The blue line denotes the approximation (4.27) obtained via DNS of Cases A4, A5, B1, and B4. Whereas, the black squares "■" represent the fit of the (normalized) turbulent eddy diffusivity D_T, defined in (4.28).

In reality, the turbulent eddy-diffusivity profile is far more complex than the one presented in (4.26). It can be evaluated from numerical results for the spanwise turbulent flux $\langle \rho_{el} v \rangle$ and the production term $\mathscr{P}_e$ in the FCV budget. In particular, under the approximation (4.15), we have,

$$D_t = -\frac{\langle \rho_{el} v \rangle^2}{\mathscr{P}_e} . \tag{4.27}$$

Accordingly, we present in Figure 4.28 profiles of the turbulent eddy diffusivity for Cases A4 ($Re_\tau = 150$), A5 ($Re_\tau = 180$), B1 (increased diffusion), and B4 (increased conductivity). In this figure, D_T is evaluated via the expression (4.27), for $0 < |y| < 0.5h$. Additionally, we have juxtaposed in each plot a fit for the turbulent eddy diffusivity, which reads,

$$D_\mathrm{t} = \frac{3\nu Re_\tau}{40}\left(1 - \exp\left(-\frac{y^+}{13}\right)\right)^5 . \tag{4.28}$$

According to Figure 4.28, D_t increases with respect to the distance from the wall, until it reaches a plateau. Moreover, due to (4.28), we infer that the turbulent eddy diffusivity does not depends linearly on the friction velocity u_τ (or, equivalently, Re_τ), as suggested by Abedian and Sonin [61]. However, the main drawback of this fit is that a closed-form solution is not readily available, in contrast to the first model. It is for this particular reason that Abedian and Sonin [61] considered an overly simplified expression for the turbulent eddy diffusivity.

4.5 Concluding remarks

In this chapter, we studied electrification in turbulent channel flows by conducting DNS. As expected from earlier observations, turbulence results in transport of electric-charge carriers from the diffuse layer towards the bulk of the channel. According to our numerical results, the electrification rate and the total charge transferred to the liquid increase dramatically with the turbulence intensity of the flow. As a result, the values of the total streaming current become exceedingly large. This, in turn, explains observations of numerous electrokinetic accidents that occurred over the last 70 years when handling petrochemicals such as benzene.

As the turbulence intensity increases, the thickness of the inner layer becomes comparable to that of the diffuse layer, which enhances the convective transport of electric-charge carriers. Then, the electric charge is built up rapidly in the bulk of the flow domain until it reaches a plateau. Accordingly, the charge-density distribution becomes statistically stationary everywhere in the liquid. A comparison of root-mean square-values revealed that turbulence reduces the fluctuations of the electric charge density. Further, our analysis of the FCV budget indicated that, inside the effective diffusion sublayer, diffusion and dissipation dominate and counter-balance one another.

Whereas, in the bulk of the channel, the dominant mechanisms are production and turbulent transport.

Additionally, we derived an expression for the mean charge-density profile based on the gradient assumption. To that end, we considered that the mean charge density consists of three zones. The first one is the effective diffusion sublayer. The second zone is a transition between the first and third regions. Inside, convective transport becomes significant due to the turbulent motions of the fluid. Then, the third zone extends throughout the bulk of the channel. Therein, the charge is almost constant. Accordingly, the closed-form profile agrees well with the numerical data for the limited range of DNS considered herein, except in the second region. For this purpose, we proposed a more complex profile for the eddy diffusivity that can be useful in the context of turbulence modeling.

Throughout this chapter, we also analyzed the role of the ohmic resistance and the diffusion of charge in turbulent flow electrification. On the one hand, the process of charge diffusion is restricted to the effective diffusion sublayer, whose thickness is very thin compared to the width of the channel. Nevertheless, this zone is of particular importance since it corresponds to the region in which gradients of the charge concentration are steep. Therefore, although limited to a specific zone (adjacent to the wall), the mechanism of charge diffusion in turbulent flow electrification should not be neglected. On the other hand, the ohmic resistance acts as a counter-balance for the convective term. This term is responsible of, *inter alia*, the decrease of the electrification rate and the variations of the electric charge density.

CHAPTER 5

Large eddy simulations of turbulent flow electrification

5.1 Introduction

The most accurate approach to treat numerically wall-bounded turbulent flows, such as pipes and channels, is via DNS. For this reason, we opted to perform DNS to study turbulent flow electrification in Chapters 3 and 4. As discussed in section 3.4.1, all flow scales are resolved in DNS, including very small vortical structures (eddies) in turbulent flows. Thus, DNS requires very fine grids, such as the ones employed in our study. On another note, the overall process of turbulent flow electrification is particularly slow. As demonstrated in Chapter 4, this phenomenon consists of three stages: a rapid buildup of charge, a transition phase, and a stationary stage in which taking statistics are required for analyzing turbulent flow electrification. As a result, our computational resources allow to perform DNS only at weak and moderate turbulence intensities (Re_τ not much higher than 250). Accordingly, the objectives of this chapter are i) to provide a subgrid-scale model for the electric charge density and ii) to conduct LES at higher Reynolds numbers.

Aside from DNS, the RANS and LES approaches are commonly employed in the field of CFD. In RANS, the turbulent structures are not resolved, thereby reducing considerably the computational cost. The LES approach, on the other hand, consists of filtering the governing equations spatially. In this manner, the grid directly resolves

the largest turbulent structures, which contain most of the turbulent kinetic energy. Consequently, in LES, only the smallest structures need to be modeled. Historically, LES is the most recent approach and is a compromise between computational cost and numerical accuracy. In particular, LES is less accurate than DNS but more accurate than RANS.

It is worth adding that several variants of RANS and LES are available in the literature. One can mention Unsteady Reynolds-Averaged Navier-Stokes models (URANS), Differential Second-Moment (DSM), Algebraic Stress Models (ASM), Implicit Large Eddy Simulations (ILES), Detached Eddy Simulations (DES), and so forth. Various factors influence the selection of a model, such as the geometries complexity and the application domain (academic or industrial). For further details about these different models and their recent advances, the interested reader is referred to [182].

The chapter is structured as follows. Section 2 describes the filtered governing equations for the fluid (Navier-Stokes) and the electric charge density. Section 3 discusses turbulence closure modeling: after validating the subgrid-scale eddy-viscosity model, we present four subgrid-scale eddy-diffusivity models for the filtered charge-density equation. We compare them with the DNS database at $Re_\tau = 180$ and $Re_\tau = 210$, presented in Chapter 4. Then, in Section 4, we carry out LES of turbulent flow electrification at higher Reynolds numbers, namely $Re_\tau = 300$ and $Re_\tau = 395$. Finally, Section 5 concludes.

5.2 Turbulence modeling

As mentioned above, the LES approach employs spatial filtering. We provide its definition as follows. The corresponding filtered field of a generic quantity ψ reads,

$$\widetilde{\psi}(\boldsymbol{x},t) = \int \psi(\boldsymbol{x}',t) G(\boldsymbol{x}-\boldsymbol{x}',t) d\boldsymbol{x}' \,, \tag{5.1}$$

where G represents the filter kernel associated with the cutoff scales in space. Three different filter kernels are widely employed in LES: Gaussian, box, and cutoff filters. As its name suggests, the first one has a Gaussian shape, while the box filter (or, equivalently, implicit filter) consists of a simple local average. The cutoff filter, on the other hand, eliminates all Fourier coefficients belonging to wavenumbers above a cutoff; see [150] for further details. For this study, we opt for the box filter because it can di-

rectly filter out the unresolved scales via the computational mesh. In particular, we can decompose ψ in a resolved and an unresolved part, $\widetilde{\psi}$ and ψ', respectively,

$$\psi \;=\; \widetilde{\psi} + \psi' \,. \tag{5.2}$$

Turbulent kinetic energy cascades from the largest (resolved) structures to the smallest ones (unresolved). In order to have an accurate computation of the resolved eddies, we must provide closure models for the filtered equations since these models account for the energy transfer to the unresolved scales. Thus, although the small scales are unresolved in LES, their effect on the resolved scales is taken into account. Accordingly, we present below the filtered governing equations (hydrodynamics and electrostatics equations) and appropriate subgrid-scale models (SGS).

5.2.1 Filtered Navier-Stokes equations

The filtered version of the governing equations for the fluid reads,

$$\nabla \cdot \widetilde{\boldsymbol{u}} \;= 0\,, \tag{5.3}$$

$$\frac{\partial \widetilde{\boldsymbol{u}}}{\partial t} + \left(\widetilde{\boldsymbol{u}} \cdot \boldsymbol{\nabla}\right) \widetilde{\boldsymbol{u}} \;=\; -\frac{1}{\rho}\nabla \widetilde{p} + \nu \nabla^2 \widetilde{\boldsymbol{u}} - \boldsymbol{\nabla} \cdot \boldsymbol{\tau}\,, \tag{5.4}$$

where the residual stress tensor $\boldsymbol{\tau} := \left(\boldsymbol{\tau}_{ij}\right)$ represents the unclosed terms of the filtered Navier-Stokes equations and is given by,

$$\boldsymbol{\tau}_{\mathrm{ij}} \;=\; \widetilde{u_{\mathrm{i}} u_{\mathrm{j}}} - \widetilde{u}_{\mathrm{i}} \widetilde{u}_{\mathrm{j}} \,. \tag{5.5}$$

Typically, the *eddy-viscosity* approach is employed to model the stress tensor [150, 168, 183]. This method considers $\boldsymbol{\tau}_{ij}$ as an additional dissipative mechanism. Then, we have,

$$\boldsymbol{\tau}_{\mathrm{ij}} - \frac{1}{3}\boldsymbol{\tau}_{\mathrm{kk}}\delta_{\mathrm{ij}} \;=\; -2\nu_{\mathrm{s}}\widetilde{S}_{\mathrm{ij}} \,, \tag{5.6}$$

where δ_{ij} and ν_{s} represent the Kronecker delta and the subgrid-scale eddy viscosity, respectively. Further, $\widetilde{\boldsymbol{S}} := \left(\widetilde{S}_{\mathrm{ij}}\right)$ stands for the filtered strain-rate tensor. It reads,

$$\widetilde{\boldsymbol{S}} = \frac{1}{2}\left(\nabla \widetilde{\boldsymbol{u}} + \left(\nabla \widetilde{\boldsymbol{u}}\right)^{\top}\right) . \tag{5.7}$$

Then, the filtered Navier-Stokes equations reads,

$$\nabla \cdot \widetilde{\boldsymbol{u}} = 0\,, \tag{5.8}$$

$$\frac{\partial \widetilde{\boldsymbol{u}}}{\partial t} + \left(\widetilde{\boldsymbol{u}} \cdot \boldsymbol{\nabla}\right) \widetilde{\boldsymbol{u}} = -\frac{1}{\rho}\nabla \widetilde{p} + \nabla \cdot \left(2\left(\nu + \nu_{\mathrm{s}}\right) \widetilde{\boldsymbol{S}}\right)\,. \tag{5.9}$$

We deduce from the above equation that it remains to determine the subgrid-scale eddy viscosity. As is common practice, we model ν_{s} via,

$$\nu_{\mathrm{s}} = \left(C_{\mathrm{S}}\,\Delta\right)^2 |\widetilde{S}|\,, \tag{5.10}$$

where C_{S} stands for the Smagorinsky coefficient and Δ denotes the nominal filter width. It is worth noting that the literature on SGS modeling is vast; see, for example, [150, 168, 183] and references therein. In this work, we define Δ as,

$$\Delta = (\Delta x \Delta y \Delta z)^{1/3}\,. \tag{5.11}$$

At first, previous authors employed static approaches to compute the Smagorinsky coefficient, consisting of taking C_{S} constant. However, these approaches resulted in certain inaccuracies, especially in the near-wall regions. This can be easily understood since, in this zone, it is expected that the molecular viscosity dominates due to friction with the wall. In particular, the subgrid-scale eddy viscosity ν_{s} must tend to zero as approaching the wall.

Subsequently, dynamic approaches were proposed. The first dynamic model (and the most popular one) was presented by Germano et al. [184] according to which C_{S} is computed dynamically (in space and time) based on the local properties of the flow field. As a consequence, the dynamic approach is computationally costlier than the static one but regarded as more accurate. The Germano's model is adequate when the turbulent flow has homogenous directions (*e.g.*, in channel flow) but is not as accurate in nonhomogeneous flow. To this end, several extensions have been presented in the literature; see, for example, [185, 186]. Notably, the *Lagrangian method* of Menneveau and Sreenivasan [186] remedies this inaccuracy by performing the computations in the Lagrangian frame of reference.

For the sake of simplicity and reduction of computational cost, we use in this work a constant Smagorinsky coefficient set equal to $C_{\mathrm{S}} = 0.17$, which is the value proposed by Lilly [187]. As is well known, C_{S} is not a universal constant but depends on the

flow domain; see, for example [188]. Hence, different values for the Smagorinsky coefficient are available in the literature. Typically, C_S ranges between 0.1 and 0.2; see [168, 183, 188, 189] and references therein. Further, to correct the behavior of the eddy viscosity in the near-wall regions, we also add in (5.10) the van Driest damping function, as is common practice [168]. Therefore, the subgrid-scale eddy viscosity reads,

$$\nu_s = \left(0.17\,\Delta\left(1 - e^{-y^+/25}\right)\right)^2 |S| , \tag{5.12}$$

where y^+ denotes the distance from the wall measured in wall units; *cf.* (3.23).

5.2.2 Filtered charge-density equation

The filtered charge-density equation is given by,

$$\frac{\partial \widetilde{\rho}_{el}}{\partial t} + \widetilde{\boldsymbol{u}} \cdot \boldsymbol{\nabla}\widetilde{\rho}_{el} = -\frac{\sigma}{\epsilon}\widetilde{\rho}_{el} + D\nabla^2\widetilde{\rho}_{el} - \nabla \cdot \boldsymbol{\zeta} , \tag{5.13}$$

where $\boldsymbol{\zeta} := \left(\zeta_j\right)$ represents the first-order tensor (*i.e.*, vector) corresponding to the unclosed terms of the filtered charge-density equation. It reads,

$$\zeta_j = \widetilde{\rho_{el} u_j} - \widetilde{\rho}_{el}\widetilde{u}_j . \tag{5.14}$$

Similarly to the derivation of the stress tensor $\boldsymbol{\tau}_{ij}$ in (5.6), we consider that the unclosed terms ζ_j of the first-order tensor $\boldsymbol{\zeta}$ operate as an additional dissipative mechanism in (5.13). Then, we have,

$$\boldsymbol{\zeta} = -D_s \boldsymbol{\nabla}\widetilde{\rho}_{el} , \tag{5.15}$$

where D_s denotes the *subgrid-scale eddy diffusivity*. Subsequently, the final form of the filtered charge-density equation reads,

$$\frac{\partial \widetilde{\rho}_{el}}{\partial t} + \widetilde{\boldsymbol{u}} \cdot \boldsymbol{\nabla}\widetilde{\rho}_{el} = -\frac{\sigma}{\epsilon}\widetilde{\rho}_{el} + \nabla \cdot \left(\left(D + D_s\right)\nabla\widetilde{\rho}_{el}\right) . \tag{5.16}$$

5.3 Grid resolution requirements

For comparison purposes, the computational setup proposed in this chapter is almost identical to that presented in section 2.4. These similarities include the geometry of the domain (channel flow), the material properties of benzene (*cf.* Table 2.2), and the boundary conditions. The only change concerns the size of the domain, reduced by half

Re_τ	L_x	L_z	$N_x \times N_y \times N_z$	Δx^+	Δz^+	Δy^+_{max}
180	$4\pi h$	$2\pi h$	$96 \times 65 \times 80$	23.56	14.14	8.71
210	$4\pi h$	$2\pi h$	$96 \times 65 \times 80$	27.48	16.49	10.16
300	$2\pi h$	πh	$96 \times 65 \times 96$	19.63	9.81	14.49
395	$2\pi h$	πh	$128 \times 96 \times 128$	19.38	9.70	12.92

Table 5.1: Summary of the parameters for the four LES considered herein. Δy_{max} corresponds to the resolution in the center of the channel, considered as the largest grid spacing in the cross-stream y direction. Further, $N_x \times N_y \times N_z$ denotes the number of grid points in each direction. Finally, L_x and L_z stand for the length and depth of the channel, respectively.

in each direction, for $Re_\tau = 300$ and $Re_\tau = 395$. The computational mesh consists of $96 \times 65 \times 80$ grid cells for $Re_\tau = 180$ and $Re_\tau = 210$. In this manner, the grid employed for LES at $Re_\tau = 180$ is 8 times finer than the one used for DNS. Whereas, it is 23 times finer for LES at $Re_\tau = 210$; see section 3.4.1.

Wu and Kasagi [190, 191, 192] and Moser et al. [193] conducted DNS of turbulent channel flow for $Re_\tau = 300$ and $Re_\tau = 395$, respectively. We use their findings for the validation of LES carried out herein. For $Re_\tau = 300$, we employ a mesh of $96 \times 65 \times 96$ grid points; while for $Re_\tau = 395$, the grid consists of $128 \times 96 \times 128$ cells. Thus, these grids contain respectively, 16 and 8 times fewer points than the computational mesh employed by Moser et al. [193] and Wu and Kasagi [190]. For clarity purposes, Table 5.1 summarizes the parameters employed for the four LES considered in this chapter. Please note that the width of the channel remains the same and is equal to $L_y = 2h$; *cf.* section 2.4.2.

5.4 Presentation of subgrid-scale eddy-diffusivity models

For this study, we present four different models for the subgrid-scale eddy diffusivity. As specified above, no closure model has been presented in the literature for D_s, to the best of our knowledge. Consequently, we compare the performance of the four models and this comparison can also be used as a baseline in future research.

5.4.1 Model 1: unresolved smallest turbulent structures (no model)

In Model 1, we assume that $D_s = 0$. In other words, it is a no-model approach. In the past, some authors advocated this approach for the eddy viscosity ν_s, commonly known as Monotonically Integrated LES (MILES); see, for example, [194, 195]. The underlying idea of no modeling the smallest turbulent structures is that the numerical dissipation is expected to be a sufficient additional diffusivity mechanism. Then, the filtered charge-density equation reads,

$$\frac{\partial \widetilde{\rho}_{el}}{\partial t} + \widetilde{\boldsymbol{u}} \cdot \boldsymbol{\nabla} \widetilde{\rho}_{el} = -\frac{\sigma}{\epsilon} \widetilde{\rho}_{el} + D \nabla^2 \widetilde{\rho}_{el} \,. \tag{5.17}$$

By ignoring the subgrid fluctuations, this approach may introduce numerical errors but their magnitude is to be assessed via numerical tests. Also, this case is of particular interest for the present study since it can serve as a reference point for the other models.

5.4.2 Model 2: uniform subgrid-scale eddy diffusivity

In the second model, we employ a constant value for D_s: the additional diffusion due the subgrid-scale eddy diffusivity is uniform inside the whole channel. Hence, we have,

$$\frac{\partial \widetilde{\rho}_{el}}{\partial t} + \widetilde{\boldsymbol{u}} \cdot \boldsymbol{\nabla} \widetilde{\rho}_{el} = -\frac{\sigma}{\epsilon} \widetilde{\rho}_{el} + \left(D + D_s\right) \nabla^2 \widetilde{\rho}_{el} \,. \tag{5.18}$$

The major drawback of employing an uniform eddy-diffusivity may concern the estimation of the unclosed terms (5.15) in the near-wall regions. In particular, it is expected that D_s tends to zero as approaching the wall, as is the case for ν_s via the van Driest damping function.

Via an *a posteriori* analysis for the value of D_s, conducted in the framework of this study, the constant value was chosen to be $D_s = 10^{-9}$ m^2/s. Please note that, like the Smagorinsky coefficient C_S, the value of this constant should not be considered as universal. Instead, it should depend on the material properties of the liquid of interest but also on the flow domain.

5.4.3 Model 3: estimation of D_s via a damping function

In the third model, we consider that the contribution of the SGS eddy diffusivity in the filtered charge-density equation is negligible at the wall, in contrast to the second

model. To this end, D_s is estimated via a damping function. The latter stems from the approximative expression for the turbulent eddy diffusivity D_t that was derived in section 4.4.2. In particular, we assume that with regards to the distance from the wall, the behavior of D_t is identical to that of D_s. Then, we have,

$$D_s = K\left(1-\exp\left(-\frac{y^+}{13}\right)\right)^5 , \tag{5.19}$$

where K denotes a constant, the value of which has been determined in this study to be $K = 7\times10^{-6}$ m^2/s. By virtue of (5.19) we infer that, at a given distance from the wall, the subgrid-scale eddy diffusivity converges towards the constant value K as the turbulent flow becomes more intense.

5.4.4 Model 4: computation of D_s via the subgrid Schmidt number

For a passive scalar in turbulent flow, LES approaches generally introduce the notion of *subgrid Schmidt number*. It consists of correlating the eddy viscosity with the eddy diffusivity of the passive scalar; see [196, 197] and references therein. In Model 4, we employ an analogous approach for the electric charge density. More specifically, we associate the eddy diffusivity with the eddy viscosity by introducing the (electric) subgrid Schmidt number, defined as,

$$Sc_s = \frac{\nu_s}{D_s} . \tag{5.20}$$

On the basis of (5.12) and (5.20), the subgrid-scale eddy diffusivity D_s is thus negligible at the wall, as is the case in Model 3.

In the specific context of turbulent heat transfer, the *subgrid Prandtl number* is more used instead of the subgrid Schmidt number since it enters the diffusive term in the temperature equation. Typically, the subgrid Prandtl number is at the order of unity (often less than one) when modeling convective heat transfer in turbulent channel flows [198–202]. For example, Georgiou and Papalexandris [201] obtained a value of 0.9 for forced convection in channels and T-junctions, while Hay and Papalexandris [202] determined the subgrid Prandtl number to equal 0.4 for natural convection.

However, to the best of our knowledge, no values for the electric subgrid Schmidt number are available in the literature. Accordingly, we have conducted an *a posteriori* analysis to determine, for the problem of interest, an appropriate estimation of the

(electric) subgrid Schmidt number. For the purpose of this study, we assume that $Sc_s = 4$. In particular, the (electric) subgrid Schmidt number is higher than one, whereas the subgrid Prandtl and Schmidt numbers are usually taken to be less than unity.

5.5 Validation of turbulence modeling

In this section, we provide a validation of turbulence modeling for the problem in hand. First, this validation involves the LES modeling for the Navier-Stokes equations without flow electrification. Then, we discuss the validity of the four SGS eddy-diffusivity models presented above.

5.5.1 SGS eddy-viscosity model

The validation of subgrid-scale models typically involves comparisons between DNS and LES results of fundamental quantities associated with the problem of interest. Herein, they correspond to the mean profile of the velocity field (*i.e.*, $\langle u \rangle$, $\langle v \rangle$, and $\langle w \rangle$) and the diagonal components of the Reynolds stress tensor, namely, u_{rms}, v_{rms}, and w_{rms}. Accordingly, we provide below these comparisons for $Re_\tau = 180$, 210, 300, and 395. We utilize our DNS database for $Re_\tau = 180$ and $Re_\tau = 210$. On the other hand, as discussed in section 5.3, we employ the DNS database of Wu and Kasagi [190] and Moser et al. [193] for $Re_\tau = 300$ and $Re_\tau = 395$, respectively.

Overall, our simulations show that the SGS eddy-viscosity model (5.12) approximates well the residual stress tensor, represented by $\boldsymbol{\tau}_{ij}$. In particular, the DNS and LES profiles of the mean streamwise velocity are in excellent agreement for $Re_\tau = 300$ and $Re_\tau = 395$, as illustrated in Figures 5.1c and 5.1d. However, the SGS eddy-viscosity model results in a slight overestimation of $\langle u \rangle$ for $Re_\tau = 180$. Conversely, it results in a slight underestimation of $\langle u \rangle$ for $Re_\tau = 210$; *cf.* Figures 5.1a and 5.1b. Additionally, we note that the difference of profiles for the mean streamwise velocity between DNS and LES is relatively more significant for $Re_\tau = 180$ than $Re_\tau = 210$.

Further, we observe the same trend when comparing profiles of the r.m.s velocity, regardless of the direction (streamwise, cross-stream, and spanwise). Globally, our LES results for $Re_\tau = 300$ and $Re_\tau = 395$ agree well with the DNS database, as depicted in Figures 5.2, 5.3, and 5.4. For $Re_\tau = 180$ and $Re_\tau = 210$, our simulations

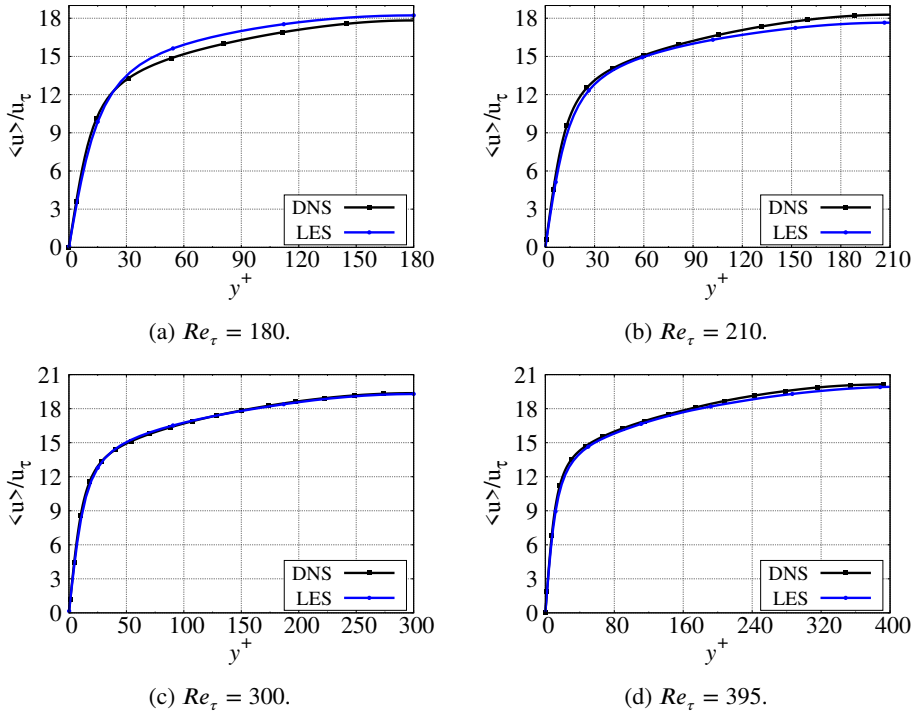

(a) $Re_\tau = 180$. (b) $Re_\tau = 210$.

(c) $Re_\tau = 300$. (d) $Re_\tau = 395$.

Figure 5.1: Comparison between DNS and LES profiles of the mean streamwise velocity $\langle u \rangle$. Our DNS database is used for $Re_\tau = 180$ and $Re_\tau = 210$. Whereas, we employ the DNS database of Wu and Kasagi [190] and Moser et al. [193] for $Re_\tau = 300$ and $Re_\tau = 395$, respectively.

suggest that the SGS eddy-viscosity model generates slight overestimations of u_{rms} (*cf.* Figure 5.2) and underestimations of both v_{rms} and w_{rms}; see Figures 5.3 and 5.4. This can be explained by the fact that LES models are typically less accurate in the prediction of high-order statistics.

In general terms, the SGS eddy-viscosity model gives satisfactorily accurate results in the range of Re_τ tested in this study. In particular, the differences in profiles between DNS and LES, depicted in Figures 5.1-5.4, are sufficiently small to be acceptable. Undoubtedly, other subgrid-scale models may result in a more accurate approximation of the unclosed terms $\boldsymbol{\tau}_{ij}$ in the filtered Navier-Stokes equations. As mentioned above, the related literature is vast. However, this chapter focuses primarily on the develop-

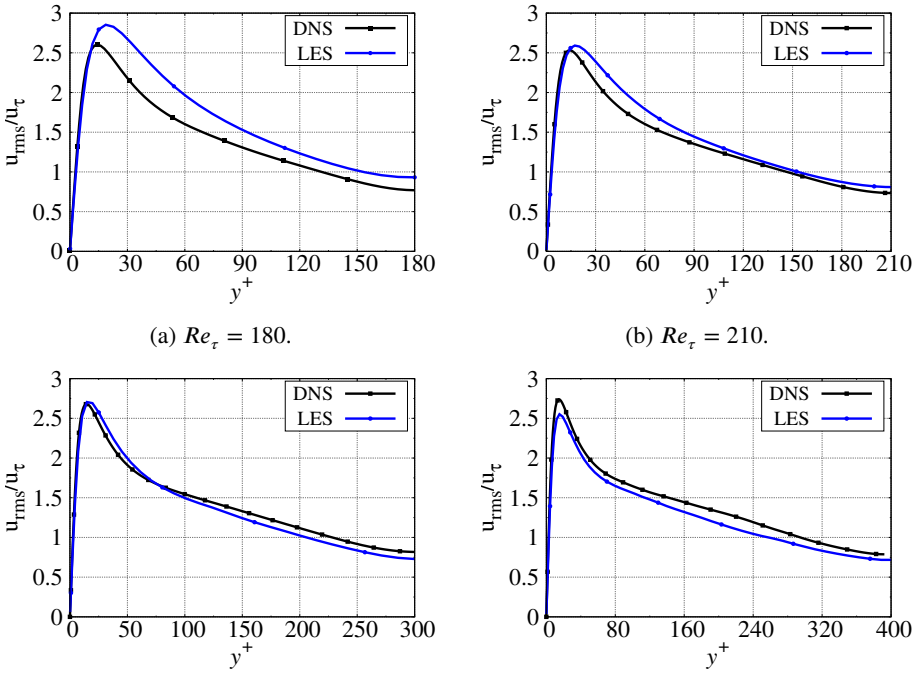

(a) $Re_\tau = 180$. (b) $Re_\tau = 210$.

(c) $Re_\tau = 300$. (d) $Re_\tau = 395$.

Figure 5.2: Comparison between DNS and LES profiles of the streamwise root-mean-square velocity u_{rms}. Our DNS database is used for $Re_\tau = 180$ and $Re_\tau = 210$. Whereas, we employ the DNS database of Wu and Kasagi [190] and Moser et al. [193] for $Re_\tau = 300$ and $Re_\tau = 395$, respectively.

ment of a cost-effective subgrid-scale model for the charge-density equation. In this context, we provide below a validation of the SGS eddy-diffusivity models.

5.5.2 SGS eddy-diffusivity models

Herein, we discuss the validity of the four SGS eddy-diffusivity models presented in section 5.4. For validation purposes, we compare these models with our DNS database for $Re_\tau = 180$ and $Re_\tau = 210$. According to the findings obtained in Chapter 4, the validation of a subgrid-scale eddy-diffusivity model is conducted on the basis of three fundamental quantities: the electrification rate, *i.e.*, the rate of change of $\langle \rho_{\text{el}} \rangle_{xz}$ at the midplane, the mean and the r.m.s of the electric charge density.

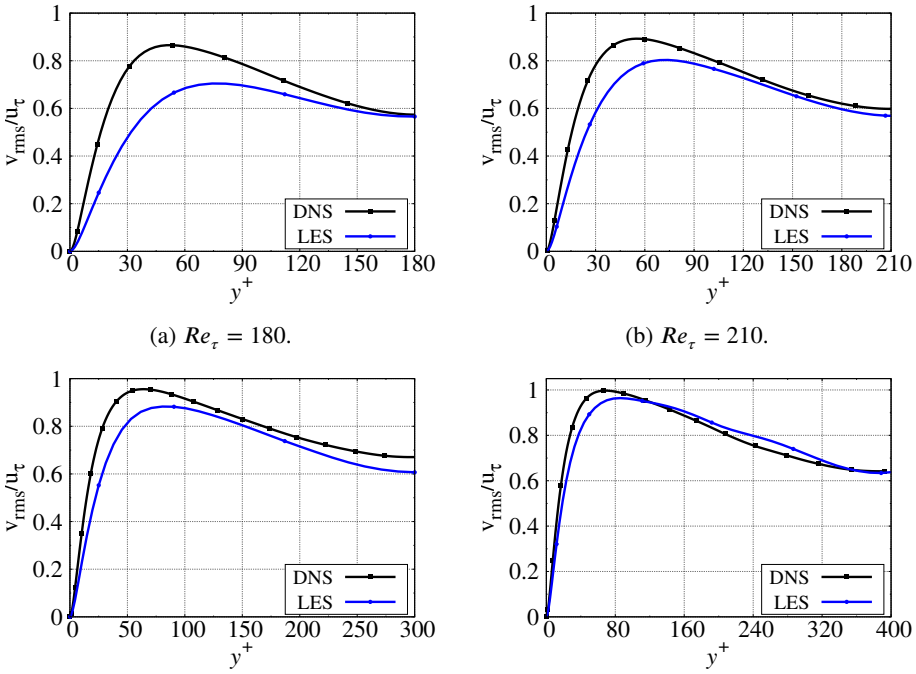

(a) $Re_\tau = 180$. (b) $Re_\tau = 210$.

(c) $Re_\tau = 300$. (d) $Re_\tau = 395$.

Figure 5.3: Comparison between DNS and LES profiles of the cross-stream root-mean-square velocity v_{rms}. Our DNS database is used for $Re_\tau = 180$ and $Re_\tau = 210$. Whereas, we employ the DNS database of Wu and Kasagi [190] and Moser et al. [193] for $Re_\tau = 300$ and $Re_\tau = 395$, respectively.

We have plotted in Figure 5.5 the evolution of the area-averaged charge density $\langle \rho_{\text{el}} \rangle_{xz}$ at the midplane, $y = 0$. First, we notice certain differences between DNS results and LES predictions with regards to Model 1. In particular, for $Re_\tau = 180$, the peak value of $\langle \rho_{\text{el}} \rangle_{xz}$, computed by using Model 1, is approximately 7.6% lower than the one estimated by our DNS; see Figure 5.5a. In addition, the area-averaged electric charge density, computed with Model 1, exhibits spurious oscillations during the third stage of electrification for both Re_τ (180 and 210).

These oscillations also exist when conducting LES with Model 2, and have practically the same amplitude as those predicted by using Model 1. As a matter of fact, we calibrated the constant value for D_{s} (in Model 2) so that, during the stationary stage, the value of the area-averaged charge density at the midplane for $Re_\tau = 180$ oscil-

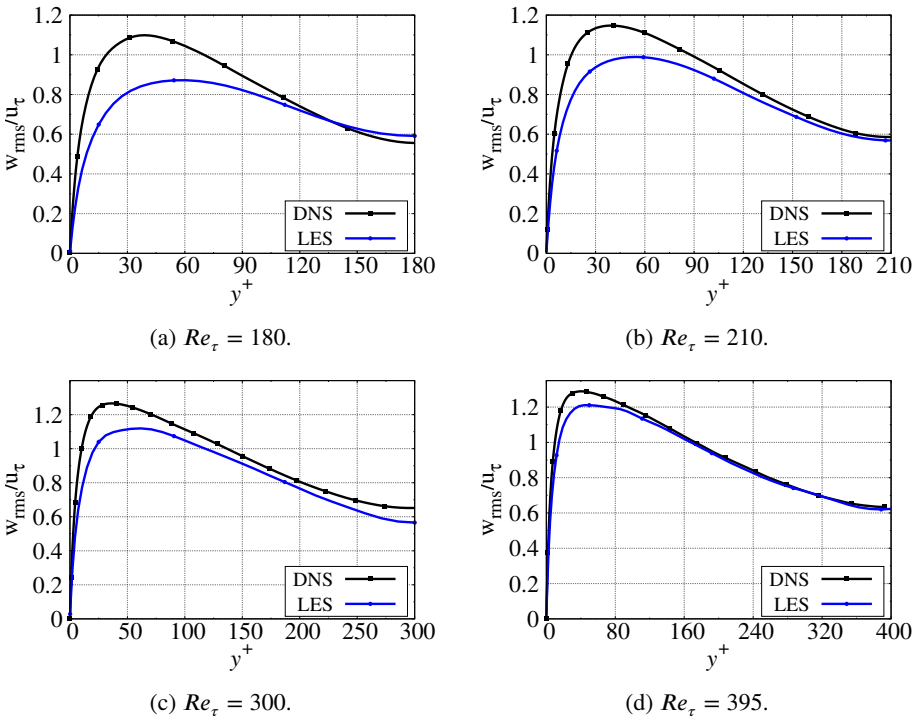

(a) $Re_\tau = 180$. (b) $Re_\tau = 210$.

(c) $Re_\tau = 300$. (d) $Re_\tau = 395$.

Figure 5.4: Comparison between DNS and LES profiles of the spanwise root-mean-square velocity w_{rms}. Our DNS database is used for $Re_\tau = 180$ and $Re_\tau = 210$. Whereas, we employ the DNS database of Wu and Kasagi [190] and Moser et al. [193] for $Re_\tau = 300$ and $Re_\tau = 395$, respectively.

lates around the peak of $\langle \rho_{\text{el}} \rangle_{xz}$, determined by DNS; *cf.* Figure 5.5a. Nonetheless, for $Re_\tau = 210$, we observe in Figure 5.5b that the final value of $\langle \rho_{\text{el}} \rangle_{xz}$ at the midplane, obtained via LES with Model 2, is 5.3% higher than the one predicted by DNS.

During the stationary stage, the final value of $\langle \rho_{\text{el}} \rangle_{xz}$ at the midplane predicted by LES with Model 3 is very close to that predicted by our DNS for $Re_\tau = 180$; see Figure 5.5a. On the other hand, for $Re_\tau = 210$, compared to DNS, the peak value of $\langle \rho_{\text{el}} \rangle_{xz}$ is 1.97% higher when carrying out LES with Model 3. Also, during the first and second stages of electrification, the electrification rate predicted by LES with Model 3 is moderately higher than the one estimated by DNS, for both Re_τ (180 and 210).

Conversely, during the first and second stages of electrification, compared to DNS, the electrification rate predicted via LES with Model 4 is slightly lower for both Re_τ.

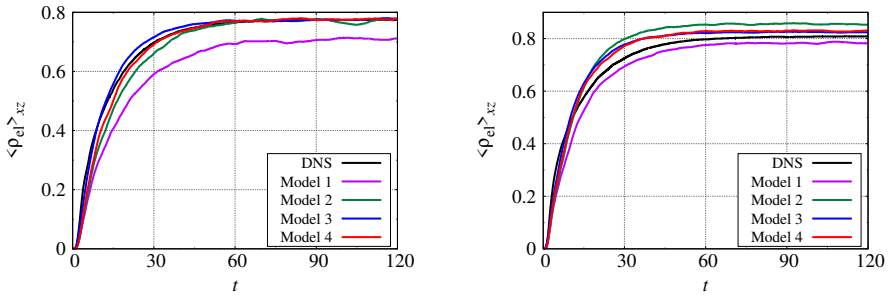

(a) $Re_\tau = 180$. (b) $Re_\tau = 210$.

Figure 5.5: Comparison between DNS and LES profiles of the evolution of the area-averaged charge density $\langle \rho_{\mathrm{el}} \rangle_{xz}$ at the midplane ($y = 0$).

Further, as is the case in DNS, the fluctuations of $\langle \rho_{\mathrm{el}} \rangle_{xz}$ at the midplane during the stationary stage are significantly reduced when conducting LES with Model 4, for both Re_τ. At this stage of electrification, the final value of $\langle \rho_{\mathrm{el}} \rangle_{xz}$, predicted by LES with Model 4, coincides with the value computed by DNS of $Re_\tau = 180$. Whereas for $Re_\tau = 210$, our simulations with Model 4 indicate that the final value of $\langle \rho_{\mathrm{el}} \rangle_{xz}$ is 2.34% higher to that predicted by our DNS; *cf.* Figure 5.5b. However, from the plots in Figure 5.5 for $Re_\tau = 180$ and $Re_\tau = 210$, the results of our simulations for the electrification rate and the peak value of the area-averaged charge density at the midplane suggest that Model 4 is more accurate than Model 3, which in turn is more accurate than Models 1 and 2.

Additionally, we have plotted in Figures 5.6 and 5.7 the profiles of the mean charge density $\langle \rho_{\mathrm{el}} \rangle$ for $Re_\tau = 180$ and $Re_\tau = 210$. According to these figures, we observe globally the same trend to that discussed above for the evolution of $\langle \rho_{\mathrm{el}} \rangle_{xz}$. First, the profile of $\langle \rho_{\mathrm{el}} \rangle$ in the bulk of the channel, obtained by conducting LES with Model 1, is below the profile of $\langle \rho_{\mathrm{el}} \rangle$ estimated by our DNS, especially for $Re_\tau = 180$; see Figure 5.6a. Whereas for $Re_\tau = 210$, this difference is less significant; see Figure 5.6b. Further, adjacent to the wall, *i.e.*, in the effective diffusion sublayer, our simulations indicate that the profile of $\langle \rho_{\mathrm{el}} \rangle$, computed by using LES with Model 1, is in excellent agreement with the DNS database, for both Re_τ (180 and 210); see Figure 5.7.

By contrast, carrying out LES with Model 2 leads to inaccuracies for $\langle \rho_{\mathrm{el}} \rangle$ in the effective diffusion sublayer due to the non-zero value of D_{S} at the wall; *cf.* (5.18).

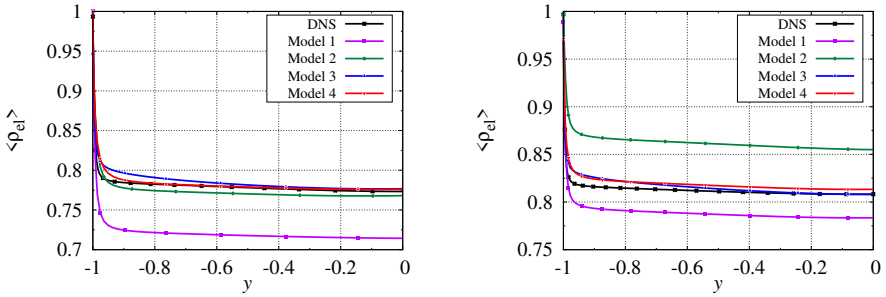

(a) $Re_\tau = 180$. (b) $Re_\tau = 210$.

Figure 5.6: Comparison between DNS and LES profiles of the mean charge density $\langle \rho_{\mathrm{el}} \rangle$ along the y-axis.

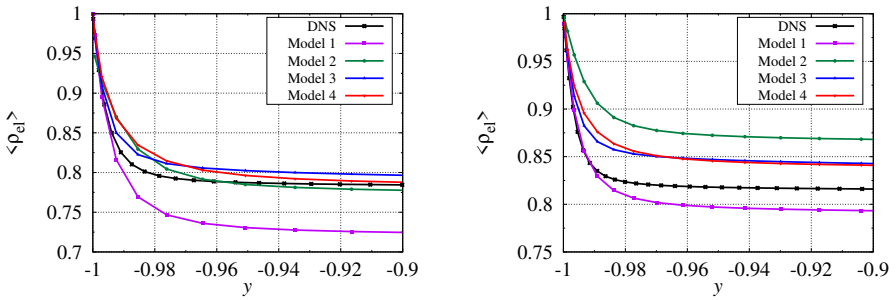

(a) $Re_\tau = 180$. (b) $Re_\tau = 210$.

Figure 5.7: Comparison between DNS and LES profiles of the mean charge density $\langle \rho_{\mathrm{el}} \rangle$ in the effective diffusion sublayer (first zone) and in the transition (second) zone.

Further, this trend is accentuated for $Re_\tau = 210$; see Figure 5.6b. As a matter of fact, only the value of $\langle \rho_{\mathrm{el}} \rangle$ in the bulk of the channel for $Re_\tau = 180$ is close to the one computed by using DNS. As mentioned above, this result was expected since we determined the constant value of D_{S} accordingly.

The profiles of $\langle \rho_{\mathrm{el}} \rangle$ with Model 3 agree well with the DNS predictions away from the wall (*i.e.*, in the bulk of the channel), especially for $Re_\tau = 180$; see Figure 5.6a. Additionally, our simulations suggest that the transition zone, corresponding approximately to $-0.99h \leq |y| \leq -0.9h$, is the region where the difference of profiles for $\langle \rho_{\mathrm{el}} \rangle$ is the most significant. As elaborated in Chapter 4, the predictions of the electric

charge density become particularly strenuous inside the transition zone. This characteristic can be readily confirmed from the plots of Figure 5.7. Also, for both Re_τ, Model 3 induces an overestimation, albeit moderate, of $\langle \rho_{\text{el}} \rangle$.

A similar analysis can be made for the LES results obtained with Model 4. More specifically, we observe from Figures 5.6 and 5.7 that the profiles of $\langle \rho_{\text{el}} \rangle$, predicted by carrying out LES with Models 3 and 4, are almost identical, at both Re_τ (180 and 210). A notable exception concerns the value of $\langle \rho_{\text{el}} \rangle$ in the effective diffusion sublayer. Inside this zone, the predictions with Model 3 are slightly more accurate than those with Model 4.

Furthermore, we have plotted in Figures 5.8 and 5.9 the r.m.s profiles of the electric charge density for $Re_\tau = 180$ and $Re_\tau = 210$. Overall, our simulations indicate a larger difference between DNS results and LES predictions for $\rho_{\text{el,rms}}$ than for $\langle \rho_{\text{el}} \rangle$. More specifically, the r.m.s profile obtained from Model 1 differs considerably to that from DNS. For example, the peak value of $\rho_{\text{el,rms}}$ obtained by simulating LES with Model 1, located in the near-wall regions, is approximately 37% higher to that obtained via DNS, for both $Re_\tau = 180$ and $Re_\tau = 210$; see Figure 5.9.

In line with the plots of $\langle \rho_{\text{el}} \rangle$, we observe that, at the wall, the profile of $\rho_{\text{el,rms}}$ with Model 2 differs significantly to the one predicted with DNS at $Re_\tau = 180$; see Figure 5.9a. Away from the wall and for both Re_τ, the r.m.s profiles of $\rho_{\text{el,rms}}$ obtained by using LES with Models 1 and 2 are practically the same; see Figure 5.8.

For Models 3 and 4, our simulations predict that, with the exception of the effective diffusion sublayer, the fluctuations of the electric charge density are more intense than those evaluated via DNS. However, from Figures 5.8 and 5.9 and for the two Reynolds numbers considered herein, it is expected that conducting LES with Model 4 may result to less inaccuracies than when conducting LES with Model 3.

To summarize, carrying out LES with Models 1 and 2 results in significant inaccuracies. By contrast, our simulations suggest that, globally, Models 3 and 4 approximate well the effect of the small-scale turbulent eddies in the filtered charge-density equation. Although the LES predictions of these two models bear similarities, we assume that Model 4 is more advantageous than Model 3. On another note, via the introduction of the subgrid Schmidt number, the fourth model takes into account the contribution of the eddy viscosity in the resolution of the smallest turbulent structures, in contrast to Model 3. In particular, by increasing the resolution of the computational grid, the LES

approach based on Model 4 can converge towards the DNS approach, on the contrary of the LES approach based on Model 3.

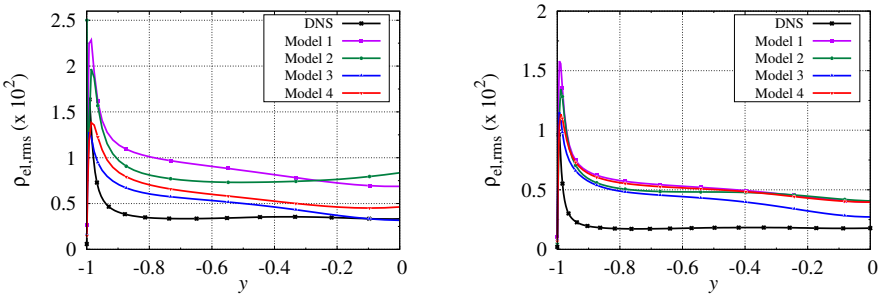

(a) $Re_\tau = 180$. (b) $Re_\tau = 210$.

Figure 5.8: Comparison between DNS and LES profiles of the r.m.s values of the electric charge density along the y-axis.

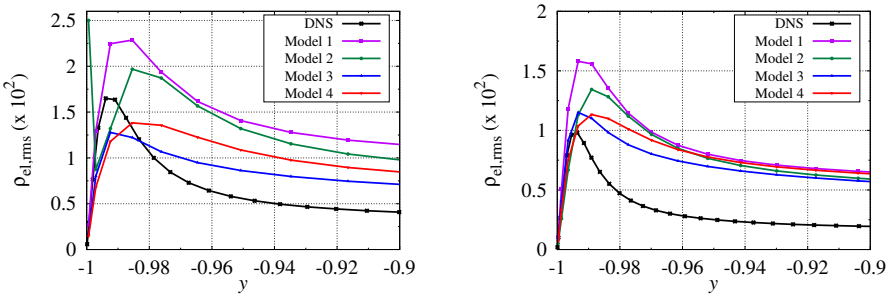

(a) $Re_\tau = 180$. (b) $Re_\tau = 210$.

Figure 5.9: Comparison between DNS and LES profiles of the r.m.s values of the electric charge density in the effective diffusion sublayer (first zone) and in the transition (second) zone.

5.6 Turbulent flow electrification at higher Reynolds numbers

In this section, we present four LES of turbulent flow electrification in a channel at $Re_\tau = 180$, 210, 300, and 395. On the basis of the above comparison of the four

subgrid-scale eddy-diffusivity models, we conduct these LES by using Model 4. In addition, we employ the notation reported in section 4.1.2 for the sake of consistency.

5.6.1 Transport and accumulation of electric-charge carriers

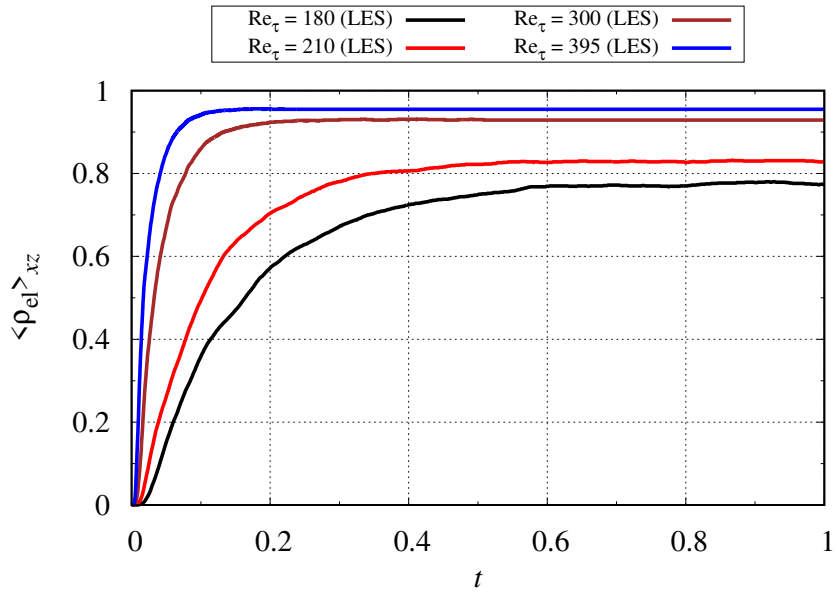

Figure 5.10: Evolution of the area-averaged charge density $\langle \rho_{\mathrm{el}} \rangle_{xz}$ at the midplane ($y = 0$) for the friction Reynolds numbers considered herein.

Our simulations of turbulent flow electrification at higher Reynolds numbers confirm all the predictions regarding the charge-density distribution that were made in low Re_τ DNS of Chapter 4. First, a more intense turbulent flow facilitates the transport of electric-charge carriers from the diffuse layer towards the bulk of the channel. We observe this phenomenon via the evolution of the area-averaged charge density $\langle \rho_{\mathrm{el}} \rangle_{xz}$ at the midplane, illustrated in Figure 5.10. As described in Chapter 4, there are three stages of electrification: a rapid buildup of charge (high electrification rate), a transition phase (lower electrification rate), and the stationary stage in which the process of electrification has been completed. According to Figure 5.10, the electrification rate increases dramatically with Re_τ. For example, when $Re_\tau = 395$, the liquid of inter-

est (benzene) reaches the third stage of electrification approximately three times faster than when $Re_\tau = 180$.

By increasing the turbulence intensity of the flow, the peak value of the electric charge density also increases, but at a lower rate. For instance, between $Re_\tau = 210$ and $Re_\tau = 300$, the final value of $\langle \rho_{\text{el}} \rangle_{xz}$ at the midplane increases by 12.3%; it is 2.7% between $Re_\tau = 300$ and $Re_\tau = 395$. As expected, during the stationary stage, the fluctuations of the area-averaged charge density $\langle \rho_{\text{el}} \rangle_{xz}$ become negligible for $Re_\tau \geq 300$.

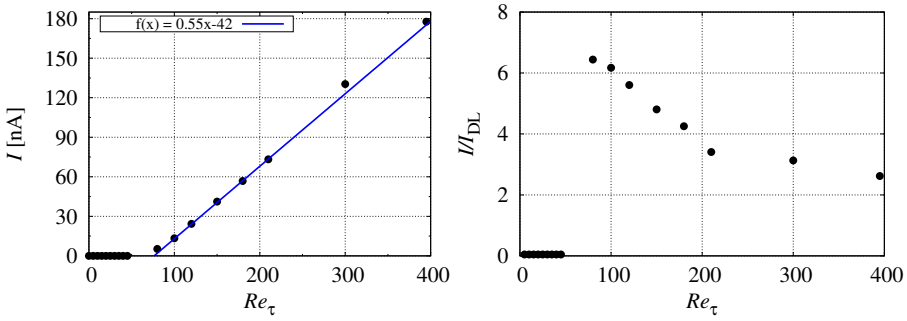

(a) Streaming current I.

(b) Ratio I/I_{DL}.

Figure 5.11: Numerical estimation of the total streaming current I (a) and the ratio I/I_{DL} (b) in terms of the friction Reynolds number. The last two points, corresponding to $Re_\tau = 300$ and $Re_\tau = 395$, are from LES. Whereas, the other points are from DNS.

As elaborated in Chapter 4, the streaming current increases with the turbulence intensity of the flow. For example, between $Re_\tau = 180$ and $Re_\tau = 395$, the total streaming current, I, has a threefold increase, as indicated in Figure 5.11a. In the same figure, we have juxtaposed a fit of the streaming current, by using the nonlinear least-squares Marquardt-Levenberg algorithm. Accordingly, it reads,

$$I\left(Re_\tau\right) \approx C_1 Re_\tau + C_2 \,, \quad \text{for} \quad Re_\tau \geq 100 \,. \tag{5.21}$$

where $C_1 = 5.5 \times 10^{-10}$ and $C_2 = -4.2 \times 10^{-8}$ are constants and have dimensions of current (Ampere).

Additionally, we have plotted respectively in Figures 5.12a and 5.12b the variations of the total charge Q and its ratio Q/Q_{DL} in terms of the turbulence intensity of the

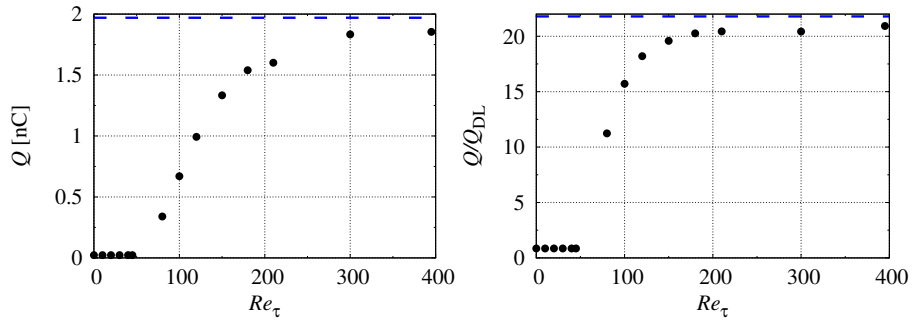

(a) Total charge Q.

(b) Ratio Q/Q_{DL}.

Figure 5.12: Numerical estimation of the total charge Q (a) and the ratio Q/Q_{DL} (b) in terms of the friction Reynolds number. The last two points, corresponding to $Re_\tau = 300$ and $Re_\tau = 395$, are from LES. Whereas, the other points are from DNS. Further, the dashed lines represent the predicted asymptotic profiles for Q, corresponding to $Q = 1.97$ [nC] (a), and for Q/Q_{DL}, corresponding to $Q/Q_{\mathrm{DL}} = h/4\lambda_{\mathrm{D}}$ (b).

flow. Our simulations indicate that there is an asymptotic profile for Q and Q/Q_{DL}, which is almost reached at $Re_\tau = 395$. These asymptotes are determined by replacing ρ_{el} by ρ_{w} in definitions (3.1) and (3.3). For the present study, they correspond to $Q = 1.97$ [nC] and $Q/Q_{\mathrm{DL}} = h/4\lambda_{\mathrm{D}}$. However, as mentioned in section 3.4.4, it is worth noting that the electric charge density cannot be everywhere equal to its value at the wall because of the ohmic resistance; *cf.* equation (2.21).

5.6.2 Charge-density statistics

Further, we have plotted in Figure 5.13 the profiles of the mean charge density $\langle \rho_{\mathrm{el}} \rangle$ along the y axis and in the near-wall regions, namely $0.9h \leq |y| \leq h$. According to it, we can identify the same three zones as in lower Re_τ, which in turn implies that this separation into three zones is valid even at large turbulence intensities. As mentioned in section 4.4.1, these zones are the effective diffusion sublayer, the transition zone, and the core of the channel. As expected, when Re_τ increases, the overall value of the mean charge density also increases. Moreover, our simulations confirm that the thickness of the effective diffusion sublayer and transition zone decreases at higher turbulence intensities. Please note that this trend is common to all boundary layers

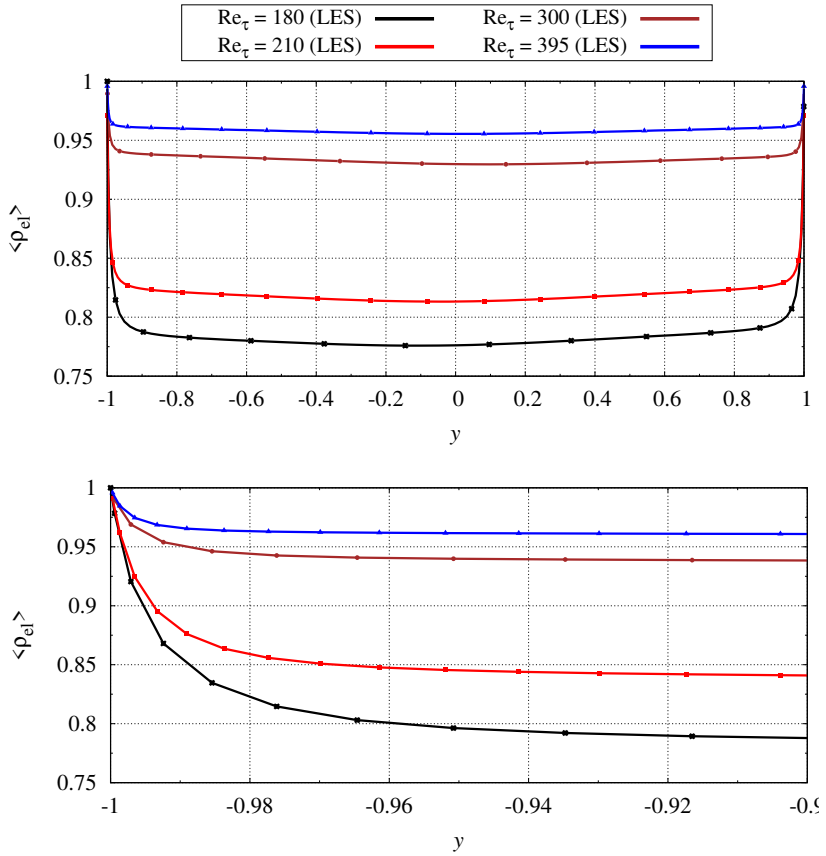

Figure 5.13: Plots of the mean charge density along the y-axis (Top) for the friction Reynolds numbers considered herein. Bottom: zoom of $\langle \rho_{\mathrm{el}} \rangle$ in the near-wall zone.

in turbulent flows: their thickness is reduced when increasing turbulence intensities. Therefore, the presumed thickness of the transition zone estimated in section 4.4.1, namely $0.9h - \delta$, where δ corresponds to the thickness of the first zone, is no longer valid for $Re_\tau = 300$ and $Re_\tau = 395$; see profiles of $\langle \rho_{\mathrm{el}} \rangle$ in Figure 5.13.

From the plots shown in Figures 5.12 and 5.13, we infer that, for the problem in hand, the efficiency of the transport of electric-charge carriers almost reaches its peak at $Re_\tau = 395$. At such turbulence intensity, the thickness of the first and second zones becomes very small, thus resulting in a uniformization of the charge-density distribution

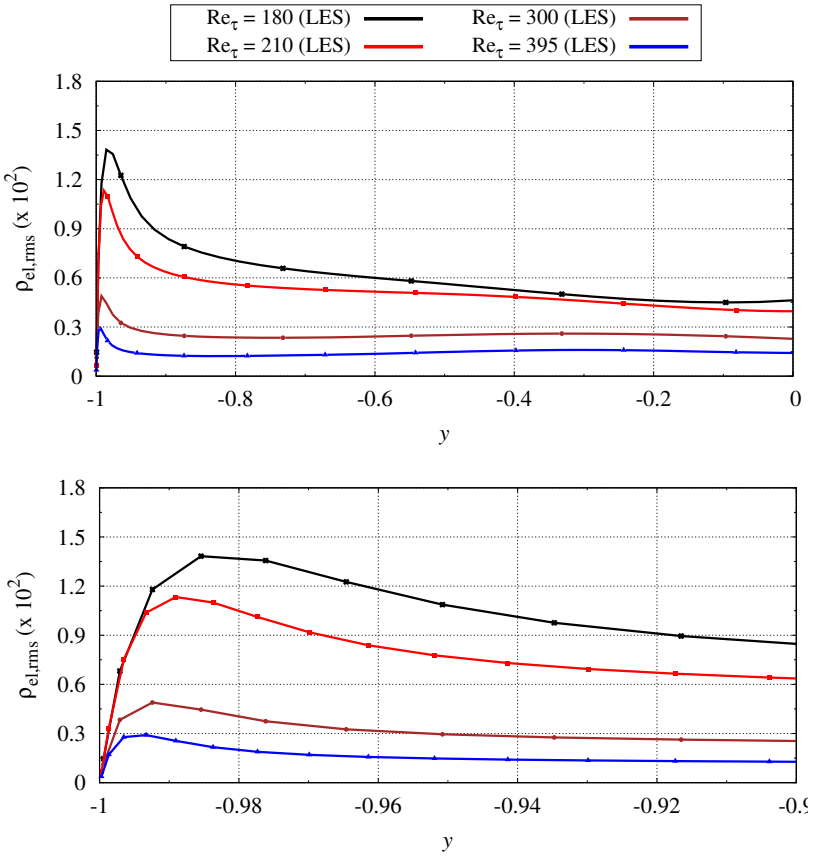

Figure 5.14: Plots of the root-mean-square charge density along the y-axis (Top) for the friction Reynolds numbers considered herein. Bottom: zoom of $\rho_{\mathrm{el,rms}}$ in the near-wall zone.

in the bulk of the channel, as shown in Figure 5.13. This phenomenon of uniformization has already been observed and discussed in Chapter 3 via the time-asymptotic profile of the charge-density distribution for a liquid at rest; *cf.* Figure 3.2. By comparing the plots of Figures 3.2 and 5.13, we readily infer that increasing the turbulence intensity of the flow results in an analogous effect on the charge-density distribution as increasing the Debye length. Please note that the profiles of $\langle \rho_{\mathrm{el}} \rangle$, obtained from our

LES, show the same trend as the profiles resulting from the approximate closed-form solution of the mean-charge density equation (4.5); *cf.* section 4.4.

The uniformization of the electric charge density in the bulk of the channel implies a significant reduction of its variations with regards to Re_τ. We confirm this trend from the plots of the r.m.s values of $\langle \rho_{\mathrm{el}} \rangle$, provided in Figure 5.14. For example, the peak of $\rho_{\mathrm{el,rms}}$ is five times higher for $Re_\tau = 180$ than for $Re_\tau = 395$. Furthermore, as predicted by our low Re_τ DNS of Chapter 4, the intensity of the turbulent flow seems to affect slightly the position of the peak. For instance, the peaks for $Re_\tau = 180$ and $Re_\tau = 395$ are located approximately at $|y| = 0.985h$ and $|y| = 0.994h$, respectively; see bottom of Figure 5.14.

5.7 Concluding remarks

In this chapter we studied the phenomenon of flow electrification in turbulent channel flows via LES. First, we derived the filtered governing equations for the problem in hand and presented four subgrid-scale eddy-diffusivity models. Accordingly, we introduced the notion of subgrid-scale (electric) Schmidt number. Then, we tested the validity of the subgrid-scale eddy-viscosity model. It corresponds to the constant Lilly-Smagorinsky approach, in which we added the van Driest damping function. Subsequently, we tested the validity of the four subgrid-scale eddy-diffusivity models. According to our simulations, the fourth model is more appropriate to approximate the unresolved turbulent eddies in the filtered charge-density equation.

Additionally, we carried out LES of turbulent flow electrification at higher Reynolds numbers. These simulations confirmed the main conclusions of the previous chapter, with regards to the electrification rate, the streaming current, the mean charge-density profile, and the fluctuations of the electric charge density. In particular, we predicted a linear dependence of the total streaming current with regards to the friction Reynolds number. Further, we demonstrated that the thickness of the third zone, corresponding to the core of the channel, increases in terms of the Reynolds number. At sufficiently high turbulence intensity, the thickness of the first and second zones becomes exceedingly small. Therefore, the electric charge density in the whole channel becomes very close to its constant value at the wall. This, in turn, implies that the efficiency of the transport and accumulation of electric-charge carriers reaches almost

its peak. According to it, at such turbulence intensity, a substantial risk of electrostatic hazards is expected. In this case, petrochemicals such as benzene must be handled with care.

CHAPTER 6

Conclusions and future perspectives

In this final chapter, we provide concluding remarks with regards to all the findings obtained throughout this thesis. Then, we discuss future perspectives for which an emphasis is placed on potential extensions of this study.

6.1 Concluding remarks

Throughout this thesis, we have investigated in detail the phenomenon of electrification of flowing dielectric liquids. Flow electrification occurs when ions (in the form of unknown impurities) are transported by a flowing liquid, in contact with a solid, from the diffuse layer towards the bulk of the flow domain. The diffuse layer, alongside the Stern layer, compose the electrical double layer which is formed at the interface between the flowing liquid and the solid, due to physico-chemical phenomena.

In the first part of our study, we elaborated on the development of an algorithm for computational electrohydrodynamics that is well suited for the study of flow electrification and, more generally, for wall-bounded flows of dielectric liquids. It has been implemented in our recently developed computational tool pafiX for simulations of flows that involve an operational hazard. Via this algorithm, we have been able to conduct numerical studies that helped assess the role of turbulence and the underpinning mechanisms of turbulent flow electrification, which had not been investigated before.

To determine the conditions in which flow electrification can take place, we examined in the second part of our study the charge-density distribution in the diffuse layer. When the fluid is at rest or the flow is laminar, the electric charge density decreases exponentially away from the wall. In this configuration, the diffuse layer is said to be fully developed. Accordingly, the total charge increases with the thickness of the diffuse layer, which is determined by the Debye length. In particular, when the electrical conductivity of the liquid is low (*e.g.*, liquid hydrocarbons), the Debye length becomes large. Further, the transport of ions from the diffuse layer towards the bulk of the flow does not occur in laminar channel flows. Hence, from this perspective, flow electrification cannot take place in this regime. However, the motion of the fluid generates a streaming current inside the diffuse layer. In laminar channel flow, the streaming current increases linearly in terms of the mean velocity, as in laminar pipes and rectangular duct flows. Moreover, the streaming current has a quadratic growth with respect to the Debye length (or, equivalently, the thickness of the diffuse layer).

On the other hand, when the flow is turbulent, the charge-density distribution in the diffuse layer is considerably modified. Unlike laminar flow, turbulence results in transport of electric-charge carriers from the diffuse layer towards the bulk of the channel. Thus, in channels, flow electrification solely occurs when the flow is turbulent. Accordingly, in the third part of our study, we investigated electrification in turbulent channel flows via DNS at weak/moderate turbulence intensities. As the turbulence intensity increases, the thickness of the inner layer becomes comparable to that of the diffuse layer, which enhances the convective transport of charge. Consequently, the total streaming current in the liquid becomes quite large. In turbulent flow of dielectric liquids, the electric charge is built up rapidly in the bulk of the channel until it reaches a plateau. During this stage of electrification, the charge-density distribution becomes statistically stationary. On another note, it corresponds also to the period in which the diffuse layer is said to be fully perturbed.

Further, the mean charge-density profile consists of three zones. The first zone corresponds to the effective diffusion sublayer which is inside both the diffuse layer and viscous sublayer. Inside this region, ions are transported via diffusion. The thickness of the effective diffusion sublayer increases with the diffusion coefficient and decreases with the velocity of the flow field. In the second zone, the convection of electric-charge

carriers becomes significant since ions move away from the wall (and the viscous sublayer). Whereas, in the third zone, the charge-density distribution is almost constant.

In addition, a more intense turbulent flow reduces the fluctuations of the electric charge density during the stationary stage. On the contrary, by increasing the electrical conductivity of the liquid, the fluctuations of the electric charge density increase. This is due to the ohmic resistance (*i.e.* conductive currents) which counter-balances the convective currents, thereby reducing the efficiency of turbulent mixing of electric-charge carriers in the liquid.

In the last part of this study, we investigated electrification in turbulent channel flows via LES at higher turbulence intensities. When the turbulence intensity is increased, the thickness of the first and second zones of the charge-density distribution becomes exceedingly small. This implies that the difference of concentration between anions and cations in the liquid becomes close to that in the Stern layer. Therefore, the convection and accumulation of ions (or, equivalently, impurities) in the liquid increase considerably.

6.2 Future perspectives

In this last section, we present four different suggestions to further extend the present study. They concern i) the geometry of the flow domain, ii) DNS at higher turbulence intensities, iii) LES at higher turbulence intensities, and iv) experimental studies.

In the past, several authors investigated turbulent flow electrification in different geometries, especially in circular pipes. Nonetheless, there is no such equivalent analysis of this phenomenon similar to that presented throughout this thesis for channel flows. Therefore, future studies could aim at reproducing the present work in other flow domains such as in circular pipes and square ducts (simple cross-sectional geometries). These studies will contribute to a better global understanding of the role of turbulence in flow electrification, regardless of the geometry of the domain. In particular, it would be interesting to assess the potential effects that the geometry of the flow domain has on fundamental quantities such as the thickness of the effective diffusion sublayer or the streaming current. On another note, the present study can be extended to dielectric liquids flowing through microporous media, filters, and screeens. However, due to their complex microstructure, a numerical analysis can be arduous.

Further, depending on the computational resources at disposal, future research should consider carrying out DNS at higher turbulence intensities to provide more insight into the phenomenon of turbulent flow electrification. Additionally, these DNS can serve as a database in the context of turbulence modeling. On another note and from an academic perspective, it would be interesting to conduct DNS at lower turbulence intensities, corresponding to Reynolds numbers ranging between 50 and 80. Please note that conducting DNS for this range of Reynolds numbers may be regarded as challenging due to the phenomenon of "numerical laminarization" of the flow. These simulations will help evaluating the convective transport of ions in the bulk of the flow domain for very low turbulence intensities. In particular, according to our numerical simulations, it is expected that the fluctuations of the electric charge density should be maximal for this range of Reynolds numbers. Indeed, at such low turbulence intensity, the efficiency of the turbulent transport is considerably reduced.

Another future direction would be to conduct LES at higher turbulence intensities, notably those that typically encountered in the process industries during the transport of dielectric liquids. This would require more investigation on the eddy-diffusivity modeling, possibly with the introduction of a dynamic approach for the computation of the subgrid-scale electric Schmidt number. It is worth adding that, due to the significance of the wall regions for the problem of interest, it is more appropriate to perform wall-resolved LES instead of wall-modeled LES.

Finally, our findings could be compared and validated through new experimental tests. As mentioned in the introduction, a team in the laboratory of Poitiers University developed a machine deemed capable of measuring the intensity of the streaming current. It would therefore be interesting to collaborate in the near future. The final purpose of this partnership will thus consist of deriving guidelines to improve safety when handling liquid hydrocarbons in the petrochemical industrial sector.

Bibliography

[1] M. Jarvis, Transparency in the Petroleum Sector: The Importance of Information and Clear Processes for Effective Development in Fragile Contexts, chap. 7, Huurdeman, A. and Rozhkova, A., 151–168, 2019.

[2] T. Ren, B. Daniel, M. Patel, K. Blok, Petrochemicals from oil, natural gas, coal and biomass: Production costs in 2030–2050, Resour. Conserv. Recycl. 53 (12) (2009) 653–663.

[3] M. Silberberg, P. Amateis, Chemistry: The Molecular Nature of Matter and Change, McGraw-Hill Education, New York, 9th edn., 2020.

[4] L. Hatch, S. Matar, From Hydrocarbons to Petrochemicals, Gulf Publishing Company, 1981.

[5] M. Papalexandris, Combustion and Fuels, Presses Universitaires de Louvain: Louvain-la-Neuve, 2020.

[6] S. Matar, L. Hatch, Chemistry of Petrochemical Processes, Elsevier, 2nd edn., 2001.

[7] R. Reid, J. Prausnitz, B. Poling, The properties of gases and liquids, McGraw-Hill, New York, 4th edn., 1987.

[8] Ceresana, Market study: Benzene, `https://www.chemeurope.com/en/news/149404/important-feedstock-for-the-chemical-industry-ceresana-analyzes-the-global-market-for-benzene.html`, 2014.

[9] J. Moore, S. Ramamoorthy, Aromatic Hydrocarbons—Monocyclics, chap. 4, 4, Springer New York, 43–66, 1984.

[10] J. Speight, Handbook of Industrial Hydrocarbon Processes, Elsevier, 2011.

[11] A. Uribe-Rodriguez, P. Castro, G. Gonzalo, B. Chachuat, Global optimization of large-scale MIQCQPs via cluster decomposition: Application to short-term planning of an integrated refinery-petrochemical complex, Comput. Chem. Eng. 140.

[12] R. Geyer, J. Jambeck, K. Law, Production, use, and fate of all plastics ever made, Sci. Adv. 3 (7) (2017) 1–5.

[13] I. Thery, J. Gril, J. Vernet, L. Meignen, J. Maury, Coal used for Fuel at Two Prehistoric Sites in Southern France: Les Canalettes (Mousterian) and Les Usclades (Mesolithic), J. Arch. Sci. 23 (4) (1996) 509–512.

[14] J. Dodson, X. Li, N. Sun, P. Atahan, X. Zhou, H. Liu, K. Zhao, S. Hu, Z. Yang, Use of coal in the Bronze Age in China, SAGE Open 24 (5) (2014) 525–530.

[15] C. Mattusch, Metalworking and Tools, in: J. P. Oleson (Ed.), The Oxford Handbook of Engineering and Technology in the CLASSICAL WORLD, Oxford University Press, 418–438, 2008.

[16] G. Irby-Massie, P. Keyser, Greek Science of the Hellenistic Era: A Sourcebook, Routledge, London, 1st edn., 2001.

[17] P. Chenier, Survey of Industrial Chemistry, Springer New York, NY, 3rd edn., 2002.

[18] P. Spitz, Petrochemicals: The Rise of an Industry, Wiley, J., Hoboken, NJ, 1988.

[19] J. Speight, The Chemistry and Technology of Coal, CRC Press Boca Raton, FL, 3rd edn., 2013.

[20] J. Speight, The Chemistry and Technology of Petroleum, CRC Press Boca Raton, FL, 5th edn., 2014.

[21] J. Gillingham, Ruhr Coal Miners and Hitler's War, J. Soc. His. 15 (4) (1982) 637–653.

[22] D. G. Tarr, The steel crisis in the United States and the European Community: Causes and adjustments, in: Issues in US-EC trade relations, University of Chicago Press, 173–200, 1988.

[23] EPCA, 50 Years of Chemistry for You. European Petrochemical Association, Brussels, Belgium, `https://epca.eu/`, 2016.

[24] IEA, The Future of Petrochemicals, `https://www.iea.org/reports/the-future-of-petrochemicals`, 2018.

[25] Q. Chen, Q. Jia, Z. Yuan, L. Huang, Environmental risk source management system for the petrochemical industry, Process. Saf. Environ. Prot. 92 (3) (2014) 251–260.

[26] J. Strelitz, L. Engel, R. Kwok, A. Miller, A. Blair, D. Sandler, Deepwater Horizon oil spill exposures and nonfatal myocardial infarction in the GuLF STUDY, Environ. Health Perspect 17 (69) (2018) 1–12.

[27] C. Delvosalle, C. Fievez, A. Pipart, B. Debray, ARAMIS project: A comprehensive methodology for the identification of reference accident scenarios in process industries, JHM Letters 130 (3) (2006) 200–219, outcome of the ARAMIS Project: Accidental Risk Assessment Methodology for Industries in the Framework of the SEVESO II Directive.

[28] A. Lindhe, L. Rosen, T. Norberg, O. Bergstedt, Fault tree analysis for integrated and probabilistic risk analysis of drinking water systems, Water Res. 43 (6) (2009) 1641–1653.

[29] B. Debray, O. Salvi, ARAMIS project: an integrated risk assessment methodology that answers the needs of various stakeholders, WIT Trans. Built Environ. 82.

[30] A. Klinkenberg, J. van der Minne, Electrostatics in the petroleum industry, Elsevier Publishing Company, University of Minnesota, 1st edn., 1958.

[31] I. Pavey, Electrostatic hazards in the process industries, Process. Saf. Environ. Prot. 82 (2004) 132–141.

[32] H. Chou, C. Yeh, C. Shu, Fire accident investigation of an explosion caused by static electricity in a propylene plant, Process. Saf. Environ. Prot. 97 (2015) 116–121.

[33] X. Diao, J. Jiang, L. Ni, A. Mebarki, G. Shen, Electrification hazard of turbulent pipe flow: Theoretical approach and numerical simulation, Process Saf. Environ. Prot. 159 (2022) 84–95.

[34] CBS, Barton solvents: explosion and fire, `https://www.csb.gov/barton-solvents-explosions-and-fire/`, 2007.

[35] A. Bourgeois, T. Paillat, O. Moreau, G. Mortha, G. Touchard, Flow electrification in power transformers: salt-type additive as a potential remedy?, J. Electrostat. 63 (6) (2005) 877–882, 10th International Conference on Electrostatics.

[36] K. Pitre, Electrophoresis | Theory of Electrophoresis, in: I. Wilson (Ed.), Encyclopedia of Separation Science, Academic Press, Oxford, 1348–1355, 2000.

[37] F. Reuss, Charge-Induced Flow, Proc. Imp. Soc. Nat. Mos. 3 (1809) 327–344.

[38] D. Wise, Remediation of Hazardous Waste Contaminated Soils, Routledge, New York, 1st edn., 1994.

[39] L. Martin, V. Alizadeh, J. Meegoda, Electro-osmosis treatment techniques and their effect on dewatering of soils, sediments, and sludge: A review, Soils Found. 59 (2) (2019) 407–418.

[40] C. Roth, Electrophoresis| Nucleic Acids, in: P. Worsfold, A. Townshend, C. Poole (Eds.), Encyclopedia of Analytical Science, Elsevier, Oxford, 2nd edn., 456–460, 2005.

[41] Q. Chang, Chapter 7 - Electrical Properties, in: Q. Chang (Ed.), Colloid and Interface Chemistry for Water Quality Control, Academic Press, 1st edn., 79–136, 2016.

[42] H. Merkus, Y. Mori, B. Scarlett, Particle size analysis by sedimentation field flow fractionation. Performance and application, Colloid. Polym. Sci. 267 (12) (1989) 1102–1107.

[43] L. Dongging, Electrokinetics Microfluidics and Nanofluidics, vol. 133 of *Fluid Mechanics and Its Applications*, Springer Cham, 1st edn., 2023.

[44] H. Dayarathne, M. Angove, S. Paudel, H. Ngo, W. Guo, B. Mainali, Optimisation of dual coagulation process for the removal of turbidity in source water using streaming potential, Groundw. Sustain. Dev. 16 (2022) 100714.

[45] J. Oh, S. Lee, Influence of streaming potential on flux decline of microfiltration with in-line rapid pre-coagulation process for drinking water production, J. Membr. Sci. 254 (1-2) (2005) 39–47.

[46] J. Lyklema (Ed.), Solid-Liquid Interfaces, vol. 2 of *Fundamentals of interface and colloid science*, Academic Press, 1995.

[47] H. Helmholtz, Ueber einige Gesetze der Vertheilung elektrischer Ströme in körperlichen Leitern mit Anwendung auf die thierisch-elektrischen Versuche, Ann. Phys. 165 (6) (1853) 211–233.

[48] M. Gouy, Sur la constitution de la charge électrique à la surface d'un électrolyte, J. Phys. 9 (1910) 457–468.

[49] D. Chapman, A contribution to the theory of electrocapillarity, Philos. Mag. 25 (1913) 475–481.

[50] O. Stern, Zur Theorie der Elektrolytischen Doppelschicht, Z. Elektrochem 30 (21-22) (1924) 508–516.

[51] W. B. Russel, D. A. Saville, W. R. Schowalter, Colloidal Dispersions, Cambridge Monographs on Mechanics, Cambridge University Press, Cambridge, 1989.

[52] S. Srinivasan, Fuel Cells: From Fundamentals to Applications, Springer New York, NY, 1st edn., 2006.

[53] M. Nakamura, N. Sato, N. Hoshi, O. Sakata, Outer Helmholtz Plane of the Electrical Double Layer Formed at the Solid Electrode–Liquid Interface, ChemPhysChem. 12 (8) (2011) 1430–1434.

[54] J. O. Bockris, M. A. V. Devanathan, K. Müller, J. Butler, On the structure of charged interfaces, Proc. Math. Phys. Eng. 274 (1356) (1963) 55–79.

[55] B. Conway, Transition from "Supercapacitor" to "Battery" Behavior in Electrochemical Energy Storage, J. Electrochem. Soc. 138 (6) (1991) 1539–1548.

[56] R. Marcus, Electron transfer reactions in chemistry. Theory and experiment, Rev. Mod. Phys. 65 (3) (1993) 599.

[57] Z. L. Wang, A. C. Wang, On the origin of contact-electrification, Mater. Today Commun. 30 (2019) 34–51.

[58] S. Lin, L. Xu, A. Chi Wang, Z. Lin Wang, Quantifying electron-transfer in liquid-solid contact electrification and the formation of electric double-layer, Nature 11 (399).

[59] J. Nie, Z. Ren, X. Liang, S. Lin, Z. Fei, X. Chen, Z. Wang, Probing Contact-Electrification-Induced Electron and Ion Transfers at a Liquid–Solid Interface, Adv. Mater. Lett. 32 (2).

[60] G. Touchard, Flow electrification of liquids, J. Electrostatics 51-52 (2001) 440–447, proceedings of the 9th International Conference on Electrostatics.

[61] B. Abedian, A. Sonin, Theory for electric charging in turbulent pipe flow, J. Fluid Mech. 120 (1982) 199–217.

[62] A. Ohsawa, Statistical analysis of fires and explosions attributed to static electricity over the last 50 years in Japanese industry, J. Phys. Conf. Ser. 301 (2011) 1–6.

[63] P. Atkins, J. de Paula, J. Keeler, Atkins' Physical Chemistry, Oxford University Press, London, 11th edn., 2018.

[64] W. Cooper, The electrification of fluids in motion, J. Appl. Phys. 4 (2) (1953) S11–S15.

[65] F. Dolezalek, Zur Theorie der binären Gemische und konzentrierten Lösungen. III., Z. Phys. Chem. 36 (33) (1913) 40–44.

[66] F. Russig, Durch comprimirten Sauerstoff veranlasste Explosionen, Chem. Ind. 36 (62).

[67] L. Bruninghaus, Électrisation et conduction électrique des hydrocarbures liquides, J. Phys. Rad. 1 (1930) 11–36.

[68] H. Nitka, Ueber die Entstehung, die Beseitigung und die Gefährlichkeit elektrostatischer Aufladungen, Chem. Fabrik 14 (1941) 211.

[69] S. Mackeown, V. Wouck, Electrical charges produced by flowing gasoline, Ind. Eng. Chem. 34 (6) (1942) 659–664.

[70] H. Keller, H. Hoelscher, Development of Static Charges in a Nonconducting System, Ind. Eng. Chem. 49 (9) (1957) 1433–1438.

[71] B. Hampel, H. Luther, Beeinflussung der elektrostatischen Aufladung strömender Kohlenwasserstoffe durch Fremdsubstanzen, Chemie. Ing. Tech. 29 (5) (1957) 323–329.

[72] F. Ernsberger, Mechanism of Frictional Electrification of Dielectric Liquids, J. Appl. Phys. 27 (4) (1956) 418–419.

[73] A. Rutgers, M. de Smet, G. de Myer, Influence of turbulence upon electrokinetic phenomena. Experimental determination of the thickness of the diffuse part of the double layer, Trans. Faraday Soc. 53 (1957) 393–396.

[74] J. Gavis, I. Koszman, Development of charge in low-conductivity liquids flowing past surfaces: A theory of the phenomenon in tubes, J. Colloid Sci. 16 (4) (1961) 375–391.

[75] I. Koszman, J. Gavis, Development of charge in low-conductivity liquids flowing past surfaces: Engineering predictions from the theory developed for tube flow, Chem. Eng. Sci. 17 (12) (1962) 1013–1022.

[76] G. Parkin, Valence, Oxidation Number, and Formal Charge: Three Related but Fundamentally Different Concepts, J. Chem. Educ. 83 (5) (2006) 791–799.

[77] A. Klinkenberg, Le Mouvement d'électricité accompagnant le Mouvement des Liquides et sa Conséquence, l'électricité dite Statique, G. Chim. 82 (1959) 149–157.

[78] A. Klinkenberg, Elektrische Aufladung schlecht leitender Flüssigkeiten bei turbulenter Strömung, Chem. Ing. Tech. 36 (3) (1964) 283–290.

[79] N. Gibson, F. Lloyd, Effect of contamination on the electrification of toulene flowing in metal pipes, Chem. Engng Sci. 25 (1) (1970) 87–95.

[80] N. Gibson, F. Lloyd, Electrification of toluene flowing in large-diameter metal pipes, J. Phys. D: Appl. Phys. 3 (4) (1970) 563–573.

[81] H. D. Goodfellow, W. Graydon, Electrostatic charging current characteristics for different fluid systems, Chem. Engng Sci. 23 (10) (1968) 1267–1281.

[82] R. C. Schwing, Electrification due to high-velocity liquids and mists: Experimental results for CHClF2 and CCl2F2 and their mixtures, J. Colloid Interface Sci. 32 (3) (1970) 433–443.

[83] I. Koszman, J. Gavis, Development of charge in low-conductivity liquids flowing past surfaces: Experimental verification and application of the theory developed for tube flow, Chem. Eng. Sci. 17 (12) (1962) 1023–1040.

[84] J. Gibbings, Electrostatics charging in the laminar flow in pipes of varying length, J. Electroanal. Chem. 25 (3) (1970) 497–504.

[85] A. Ratschow, S. Stein, H. Gross, Charge distribution in turbulent flow of charged liquid-Modeling and experimental validation, Process Saf. Prog. n/a (n/a).

[86] B. Abedian, A. Sonin, Electric currents generated by turbulent flows of liquid hydrocarbons in smooth pipes: Experiment vs. Theory, Chem. Eng. Sci. 41 (12) (1986) 3183–3189.

[87] A. Boumans, Streaming current in turbulent flows and metal capillaries. I. Theory (1). Distribution of charge in the liquid, Physica XXIII 23 (1957) 1007–1026.

[88] G. Touchard, Turbulent flow electrification with hydrocarbon liquids, liquid hydrogen, liquefied natural gas (LNG) and liquid nitrogen: Part I–Three different models, Int. J. Plasma Environ. Sci. 15 (2) (2021) 1–32.

[89] A. Boumans, Streaming current in turbulent flows and metal capillaries. II. Theory (2). Charge transported by the flow of liquid, Physica XXIII 23 (1957) 1027–1037.

[90] A. Boumans, Streaming current in turbulent flows and metal capillaries. III. Experiment (1). Aim and procedure, Physica XXIII 23 (1957) 1038–1046.

[91] A. Boumans, Streaming current in turbulent flows and metal capillaries. III. Experiment (2). Results and conclusions, Physica XXIII 23 (1957) 1047–1055.

[92] G. Touchard, Streaming currents developed in laminar and turbulent flows through a pipe, J. Electrostat. 5 (1978) 463–476.

[93] J. Cabaleiro, T. Paillat, G. Artana, G. Touchard, Flow Electrification in Turbulent Flows of Liquids—Comparison of Two Models for One Specific Case, IEEE Trans. Ind. Appl. 55 (5) (2019) 5235–5328.

[94] G. Touchard, Turbulent flow electrification with hydrocarbon liquids, liquid hydrogen, liquefied natural gas (LNG) and liquid nitrogen: Part II–Experiments and comparison with different models, Int. J. Plasma Environ. Sci. 15 (2) (2021) 1–15.

[95] G. Touchard, T. W. Patzek, C. J. Radke, A physicochemical explanation for flow electrification in low-conductivity liquids in contact with a corronding wall, IEEE Trans. Ind. Appl. Soc. 32 (5) (1996) 1051–1057.

[96] J. Cabaleiro, T. Paillat, O. Moreau, G. Touchard, Flow electrification of dielectric liquids in insulating channels: Limits to the application of the classical wall current expression, J. Electrostat. 66 (1) (2008) 79–83.

[97] T. Paillat, J. Cabaleiro, H. Romat, G. Touchard, Flow electrification process: the physicochemical corroding model revisited, IEEE Trans. Dielectr. Electr. Insul. 16 (2) (2009) 359–363.

[98] P. Leblanc, J. M. Cabaleiro, T. Paillat, G. Touchard, Impact of the laminar flow on the electrical double layer development, J. Electrostat 88 (2017) 76–80, special Issue on The International Conference on Electrostatics.

[99] P. Leblanc, T. Paillat, J. Cabaleiro, G. Touchard, Flow electrification investigation under the effect of the flow parameters, Int. J. Plasma Environ. Sci. Technol. 11 (2) (2018) 156–160.

[100] M. El-Adawy, T. Paillat, Y. Bertrand, O. Moreau, G. Touchard, Physicochemical Analysis at the Interface Between Conductive Solid and Dielectric Liquid for Flow Electrification Phenomenon, IEEE Trans. Ind. Appl. 46 (4) (2010) 1593–1600.

[101] M. El-Adawy, T. Paillat, G. Touchard, Numerical simulation of the electrical double layer development: Physicochemical model at the solid and dielectric liquid interface for laminar flow electrification phenomenon, IEEE Trans. Dielectr. Electr. Insul. 18 (5) (2011) 1463–1475.

[102] M. Ela, T. Paillat, G. Touchard, J. Cabaleiro, Numerical simulation of the electrical double layer development: physicochemical model at the solid and dielectric liquid interface for laminar flow electrification phenomenon, IEEE Trans. Dielectr. Electr. Insul. 18 (5) (2011) 1463–1475.

[103] H. Walmsley, G. Woddford, The generation of electric currents by the laminar flow of dielectric liquids, J. Phys. D: Appl. Phys 14 (10).

[104] A. Washabaugh, M. Zhan, A chemical reaction-based boundary condition for flow electrification, IEEE Trans. Dielectr. Electr. Insul. 4 (6) (1997) 688–709.

[105] G. Domínguez, G. Touchard, Streaming current development in a rectangular channel, J. Electrostat. 40-41 (1997) 153–159, Proceedings of the 8th International Conference on Electrostatics.

[106] T. Paillat, E. Moreau, G. Touchard, Space charge density at the wall in the case of heptane flowing through an insulating pipe, J. Electrostat. 53 (2) (2001) 171–182.

[107] J. Vazquez-Garcia, J. Rivenc, A. Agneray, T. Paillat, G. Touchard, A critical approach to measure streaming current: case of fuels flowing through conductive and insulating polymer pipes, IEEE Trans. Ind. Appl. 41 (5) (2005) 1335–1342.

[108] T. Paillat, O. Moreau, J. Cabaleiro, F. Perisse, G. Touchard, Flow electrification: An electrical model, J. Electrostat. 64 (7-9) (2006) 485–491.

[109] T. Paillat, G. Touchard, Electrical charges and liquids motion, J. Electrostat. 67 (2-3) (2009) 326–334.

[110] J. Cabaleiro, T. Paillat, G. Touchard, Transient electrical double layer dynamics in a quiescent fluid, IEEE Trans. Dielectr. 21 (1) (2014) 171–178.

[111] P. Clermont, T. Paillat, Y. Duval, J. Rivenc, G. Peres, Flow Electrification of an Electrically Charged Liquid, Int. J. Plasma Environ. Sci. Technol. 10 (2) (2016) 125–130.

[112] J. Cabaleiro, T. Paillat, G. Artana, G. Touchard, Flow Electrification of Liquids in Rectangular Channels—Comparison of Different Theoretical Models, IEEE Trans. Ind. Appl. 53 (6) (2017) 5831–5837.

[113] P. Clermont, T. Paillat, G. Peres, Y. Duval, G. Touchard, Quantification of Flow Electrification in the Context of a Tank Being Filled With a Dielectric Liquid, IEEE Trans. Ind. Appl. 53 (5) (2017) 4944–4949.

[114] I. Miaoulis, B. Abedian, M. Darnahal, Theory for electric charging in flow of low-conductivity liquids through screens, J. Electrostat. 25 (3) (1990) 287–294.

[115] G. Touchard, T. Artana, G.and Paillat, Analysis of flow electrification in micro rough capillaries, IEEE Trans. Dielectr. Electr. Insul. 20 (5) (2013) 1474–1480.

[116] P. W. Huber, A. A. Sonin, Theory for electric charging in liquid hydrocarbon filtration, J. Colloid Interface Sci. 61 (1) (1977) 109–125.

[117] P. W. Huber, A. A. Sonin, Electric charging in liquid hydrocarbon filtration: A comparison of theory and experiments, J. Colloid Interface Sci. 61 (1) (1977) 126–145.

[118] J. Gavis, J. Wagner, Electric charge generation during flow of hydrocarbons through microporous media, Chem. Eng. Sci. 23 (4) (1968) 381–391.

[119] T. Paillat, E. Moreau, P. Grimaud, G. Touchard, Electrokinetic phenomena in porous media applied to soil decontamination, IEEE Trans. Dielectr. Electr. Insul. 7 (5) (2000) 693–704.

[120] T. Paillat, E. Moreau, G. Touchard, Flow electrification through porous media, J. Loss Prev. Process. Ind. 14 (2) (2001) 91–93.

[121] G. Artana, G. Touchard, O. Moreau, Flow electrification due to the flow of a perpendicular jet on a flat plate, J. Electrostat. 40-41 (1997) 129–134, Proceedings of the 8th International Conference on Electrostatics.

[122] G. Touchard, P. Mas, T. Paillat, O. Moreau, Static electrification in power transformers: Correlation between charge generation and ECT-tan/spl delta/ parameters for different oil-pressboard couples, in: Proceedings of IEEE 13th International Conference on Dielectric Liquids, 396–399, 1999.

[123] P. Mas, T. Paillat, O. Moreau, G. Touchard, Flow electrification in power transformers: temperature influence on space charge distribution and charge accumulation in pressboard, J. Electrostat 51-52 (2001) 488–493.

[124] T. Paillat, L. Onic, O. Moreau, N. Charvet, G. Touchard, Influence of pressboard physico-chemical composition on static electrification in power transformers, IEEE Trans. Ind. Appl. 39 (2) (2003) 346–354.

[125] J. Cabaleiro, T. Paillat, O. Moreau, G. Touchard, Electrical Double Layer's Development Analysis: Application to Flow Electrification in Power Transformers, IEEE Trans. Ind. Appl. 45 (2) (2009) 597–605.

[126] M. El-Adawy, J. Cabaleiro, T. Paillat, O. Moreau, G. Touchard, Experimental determination of space charge density associated with flow electrification

phenomenon: Application to power transformers, J. Electrostat. 67 (2) (2009) 354–358, 11th International Conference on Electrostatics.

[127] T. Paillat, Y. Zelu, G. Morin, C. Perrier, Ester oils and flow electrification hazards in power transformers, IEEE Trans. Dielectr. Electr. Insul. 19 (5) (2012) 1537–1543.

[128] T. Paillat, G. Touchard, Y. Bertrand, "Capacitive sensor" to measure flow electrification and prevent electrostatic hazards, Sensors 12 (11) (2012) 14315–14326.

[129] T. Paillat, G. Morin, G. Touchard, O. Moreau, A. Tanguy, Electrostatic hazard in high-power transformers: Results of ten years of experience with P' Capacitive Sensor, IEEE Trans. Ind. Appl. 49 (4) (2013) 1751–1757.

[130] J. M. López-Herrera, S. Popinet, M. A. Herrada, A charge-conservative approach for simulating electrohydrodynamic two-phase flows using volume-of-fluid, J. Comput. Phys. 230 (5) (2011) 1939–1955.

[131] I. Roghair, D. van den Ende, F. Mugele, An OpenFOAM-based electrohydrodynamical model, in: 8th Int. Conf. Multiphase Flow, Jeju, Korea, 1–5, 2013.

[132] pafiX, `https://www.ptb.de/cms/asep`, 2019.

[133] G. Batchelor, An Introduction to Fluid Dynamics, Cambridge Mathematical Library, Cambridge University Press, Cambridge, 2000.

[134] L. D. Landau, E. M. Lifshitz, Landau and Lifshitz: Course of Theoretical Physics, vol. 6, Elsevier, 2nd edn., 1977.

[135] M. Rieutord, Fluid Fynamics: An Introduction, Graduate Texts in Physics, Springer Cham, 1st edn., 2015.

[136] D. J. Tritton, Physical fluid dynamics, Springer Dordrecht, 1st edn., 1977.

[137] A. Castellanos, Coulomb-driven convection in electrohydrodynamics, IEEE Trans. Dielectr. Electr. Insul. 26 (6) (1991) 1201–1215.

[138] J. Melcher, G. Taylor, Electrohydrodynamics: A Review of the Role of Interfacial Shear Stresses, Annu. Rev. Fluid Mech. 1 (1) (1969) 111–146.

[139] D. A. Saville, Electrohydrodynamics: The Taylor-Melcher Leaky Dielectric Model, Annu. Rev. Fluid Mech. 29 (1) (1997) 27–64.

[140] P. Dumargue, Perturbations des couches diffuses-I. Équations théoriques de base, Electrochim. Acta 16 (8) (1971) 1115–1128.

[141] J. Melcher, Continuum Electromechanics, Cambridge, Mass. : MIT Press, 1981.

[142] J. M. Crowley, Dimensionless Ratios in Electrohydrodynamics, in: J. Chang, A. Kelly, J. M. Crowley (Eds.), Handbook of Electrostatic Processes, chap. 7, CRC Press, 1st edn., 99–121, 1995.

[143] A. Castellanos, Electrohydrodynamics, Springer Vienna, 1998.

[144] H. Grosshans, M. Papalexandris, Direct numerical simulation of tribolelectric charging in a particle-laden turbulent channel flow, J. Fluid Mech. 818 (2017) 465–491.

[145] H. Grosshans, M. Papalexandris, Modulation of particle dynamics in dilute duct flows by electrostatic charges, Phys. Fluids 30 (8).

[146] H. Grosshans, C. Bissinger, M. Calero, M. Papalexandris, The effect of electrostatic charges on particle-laden duct flows, J. Fluid Mech. 909 (2021) A21.

[147] A. Huser, S. Biringen, Direct numerical simulation of turbulent flow in a square duct, J. Fluid Mech. 257 (1993) 65–95.

[148] G. Sharma, D. Phares, Turbulent transport of particles in a straight square duct, Int. J. Multi. Flow 32 (7) (2006) 823–837.

[149] F. Harlow, J. Welch, Numerical Calculation of Time-Dependent Viscous Incompressible Flow of Fluid with a Free Surface, Phys. Fluids 8 (12) (1965) 2182–2189.

[150] J. H. Ferziger, B. Perić, R. Street, Computational Methods for Fluid Dynamics, Springer Cham, 4th edn., 2019.

[151] S. Patankar, Numerical heat transfer and fluid flow, McGraw-Hill book company, 1980.

[152] D. Anderson, J. Tannehill, R. Pletcher, R. Munipalli, V. Shankar, Computational Fluid Mechanics and Heat Transfer, CRC Press, 4th edn., 2020.

[153] W. Press, S. Teukolsky, W. Vetterling, B. Flannery, Numerical recipes in C: the art of scientific computing, Cambridge University Press, New York, 2nd edn., 1992.

[154] L. Caretto, A. Gosman, S. Patankar, D. Spalding, Two calculation procedures for steady, three-dimensional flows with recirculation, in: Proceedings of the Third International Conference on Numerical Methods in Fluid Mechanics, Springer Berlin Heidelberg, Berlin, Heidelberg, 60–68, 1973.

[155] J. van Doormal, G. Raithby, Enhancements of the SIMPLE method for predicting incompressible fluid flows, Numer. Heat Transfer 7 (2) (1984) 147–163.

[156] R. Issa, Solution of implicitly discretized fluid flow equations by operator-splitting, J. Comput. Phys. 62 (1) (1986) 40–65.

[157] B. van Leer, Towards the ultimate conservative difference scheme. II. Monotonicity and conservation combined in a second-order scheme, J. Comput. Phys. 14 (4) (1974) 361–370.

[158] B. van Leer, Towards the ultimate conservative difference scheme. III. Upstream-centered finite-difference schemes for ideal compressible flow, J. Comput. Phys. 23 (3) (1977) 263–275.

[159] B. van Leer, Towards the ultimate conservative difference scheme. V. A second-order sequel to Godunov's method, J. Comput. Phys. 32 (1) (1979) 101–136.

[160] P. L. Roe, Characteristic-Based Schemes for the Euler Equations, Ann. Rev. Fluid Mech. 18 (1) (1986) 337–365.

[161] B. Koren, A robust upwind discretization method for advection, diffusion and source terms, chap. 5, Notes on Numerical Fluid Mechanics, Vieweg, Germany, 117–138, 1993.

[162] G. Zhou, Numerical simulations of physical discontinuities in single and multi-fluid flows for arbitrary Mach numbers, Chalmers University of Technology, 1995.

[163] N. Waterson, H. Deconinck, Design principles for bounded higher-order convection schemes – a unified approach, J. Comput. Phys. 224 (1) (2007) 182–207.

[164] Chemical book, `https://www.chemicalbook.com/`, 2022.

[165] A. S. Brown, P. Levin, E. Abrahamson, Dielectric Constant of Benzene at 25°C by the Wyman Method, J. Chem. Phys. 19 (10) (1951) 1226–1229.

[166] E. Forster, Electric Conduction in Liquid Hydrocarbons. I. Benzene, J. Chem. Phys. 37 (5) (1962) 1021–1028.

[167] H. Ohshima, K. Furusawa (Eds.), Electrical Phenomena at Interfaces. Fundamentals, Measurements, and Applications, vol. 76 of *Surfactant Science*, Routledge, New York, 2nd edn., 1998.

[168] S. B. Pope, Turbulent Flows, Cambridge University Press, New York, 2000.

[169] H. Tennekes, J. Lunley, A first course in turbulence, The MIT Press, 1st edn., 1972.

[170] J. Kim, P. Moin, R. Moser, Turbulence statistics in fully developed channel flow at low Reynolds number, J. Fluid Mech. 177 (1987) 133–166.

[171] S. Park, M. Seo, Chapter 1 - Intermolecular Force, in: Interface Science and Composites, vol. 18 of *Interface Science and Technology*, Elsevier, 1–57, 2011.

[172] C. Liu, Y. Meng, Tribology at charged solid-liquid interfaces, in: Reference Module in Chemistry, Molecular Sciences and Chemical Engineering, Elsevier, 2023.

[173] M. Calero, H. Grosshans, M. Papalexandris, A computational framework for electrification of liquid flows, J. Loss Prevent. Proc. 74 (2022) 104637.

[174] V. Patel, M. Head, Some observations on skin friction and velocity profiles in fully developed pipe and channel flows, J. Fluid Mech. 38 (1) (1969) 181–201.

[175] M. Calero, H. Grosshans, M. Papalexandris, Electrification in turbulent channel flows of liquid dielectrics, Phys. Fluids 35 (4) (2023) 045119.

[176] W. Hay, M. Papalexandris, Numerical simulations of turbulent thermal convection with a free-slip upper boundary, Proc. Roy. Soc. A. 475 (2019) 20190601.

[177] W. Hay, M. Papalexandris, Evaporation-driven turbulent convection in water pools, J. Fluid Mech. 904 (2020) A14.

[178] H. Reichardt, Vollstandige Darstellung der turbulenten Geschwindigkeitsverteilung in glatten Leitungen, Z. Angew. Math. Mech. 31 (7) (1951) 208–219.

[179] A. Quarmby, A. R.K., Non-axisymmetric turbulent mass transfer in a circular tube, J. Fluid Mech. 38 (3) (1969) 457–472.

[180] B. S. Petukhov, Heat Transfer and Friction in Turbulent Pipe Flow with Variable Physical Properties, vol. 6 of *Advances in Heat Transfer*, Academic Press, 1970.

[181] D. Combest, P. Ramachandran, M. Dudukovic, On the Gradient Diffusion Hypothesis and Passive Scalar Transport in Turbulent Flows, Ind. Eng. Chem. Res. 50 (15) (2011) 8817–8823.

[182] C. Argyropoulos, N. Markatos, Recent advances on the numerical modelling of turbulent flows, Appl. Math. Model 39 (2) (2015) 693–732.

[183] P. Sagaut, Large eddy simulation for incompressible flows: an introduction, Springer Science & Business Media, 2005.

[184] M. Germano, U. Piomelli, P. Moin, W. Cabot, A dynamic subgrid-scale eddy viscosity model, Phys. Fluids 3 (1991) 1760–1765.

[185] D. Lilly, A proposed modification of the Germano subgrid-scale closure method, Phys. Fluids 4 (1992) 633–645.

[186] C. Menneveau, K. Sreenivasan, A Lagrangian dynamic subgrid-scale model of turbulence, J. Fluid Mech. 319 (1996) 353–385.

[187] D. Lilly, The representation of small-scale turbulence in numerical simulation experiments, IBM Form. 4 (1992) 195–210.

[188] V. Canuto, Y. Cheng, Determination of the Smagorinsky–Lilly constant C_S, Phys. Fluids 9 (1997) 1368–1378.

[189] J. W. Deardorff, A numerical study of three-dimensional turbulent channel flow at large Reynolds numbers, J. Fluid Mech. 41 (1970) 453–480.

[190] H. Wu, N. Kasagi, Effects of arbitrary directional system rotation on turbulent channel flow, Phys. Fluids 16 (2004) 979–990.

[191] H. Wu, N. Kasagi, Turbulent Heat Transfer in A Channel Flow with Arbitrary Directional System rotation, Phys. Fluids 47 (2004) 4579–4591.

[192] H. Wu, N. Kasagi, Fully Developed Channel Flow and Heat Transfer with Streamwise System Rotation at $Re_\tau = 300$, `https://thtlab.jp/DNS/CH122_RT.WL7`, 2004.

[193] R. Moser, J. Kim, N. Mansour, Direct numerical simulation of turbulent channel flow up to $Re_\tau = 590$, Phys. Fluids 11 (4) (1990) 943–945.

[194] E. S. Oran, J. P. Boris, Computing Turbulent Shear Flows — A Convenient Conspiracy, Comput. Phys. 7 (5) (1991) 532–533.

[195] C. Fureby, F. Grinstein, Monotonically integrated large eddy simulation of free shear flows, AIAA J. 37 (5) (1999) 544–556.

[196] M. Lesieur, R. Rogallo, Large-eddy simulation of passive scalar diffusion in isotropic turbulence, Phys. Fluids 1 (4) (1989) 718–722.

[197] L. Bricteux, M. Duponcheel, G. Winckelmans, I. Tiselj, Y. Bartosiewicz, Direct and large eddy simulation of turbulent heat transfer at very low Prandtl number: Application to lead–bismuth flows, Nucl. Eng. Des. 246 (2012) 91–97.

[198] O. Métais, M. Lesieur, Spectral large-eddy simulation isotropic and stablystratified turbulence, J. Fluid Mech. 239 (1992) 157–194.

[199] T. Kobayashi, M. Kano, T. Ishihara, Prediction of turbulent flow in two-dimensional channel with turbulence promoters (1st report, numerical predictions by large eddy simulation), Bull. JSME 27 (231) (1984) 1893–1898.

[200] T. Kobayashi, M. Kano, T. Ishihara, Prediction of turbulent flow in two-dimensional channel with turbulence promoters (3rd report, improvement of large eddy simulation and formation of streaklines), Bull. JSME 28 (246) (1985) 1893–1898.

[201] M. Georgiou, M. V. Papalexandris, Direct numerical simulation of turbulent heat transfer in a T-junction, J. Fluid Mech. 845 (2018) 581–614.

[202] W. Hay, M. Papalexandris, Turbulent thermal convection driven by free-surface evaporation in cuboidal domains of different aspect ratios, Phys. Fluids 33 (2021) 015104.